The investigation of photo induced electric currents in the terahertz frequency range is a vastly efficient tool for the study of nonequilibrium processes in low-dimensional structures. In this work, non-linear transport phenomena in graphene as well as in silicon – both being multi-valley semiconductors – driven by the free-carrier absorption of electromagnetic radiation are explored. It is demonstrated that the individual control of electron fluxes in different valleys can be achieved by the excitation of valley degenerate structures with polarized light. Moreover, the experiments together with theoretical considerations show that the microscopic origins of these currents are mainly orbital mechanisms. Thus, novel models of photocurrents are developed, where the charge carriers' orbital motion is caused by the crossed alternating electric and magnetic field components of the incident radiation. Under asymmetric photoexcitation or relaxation, this may result in a directed electric current.

Dissertationsreihe Physik - Band 22
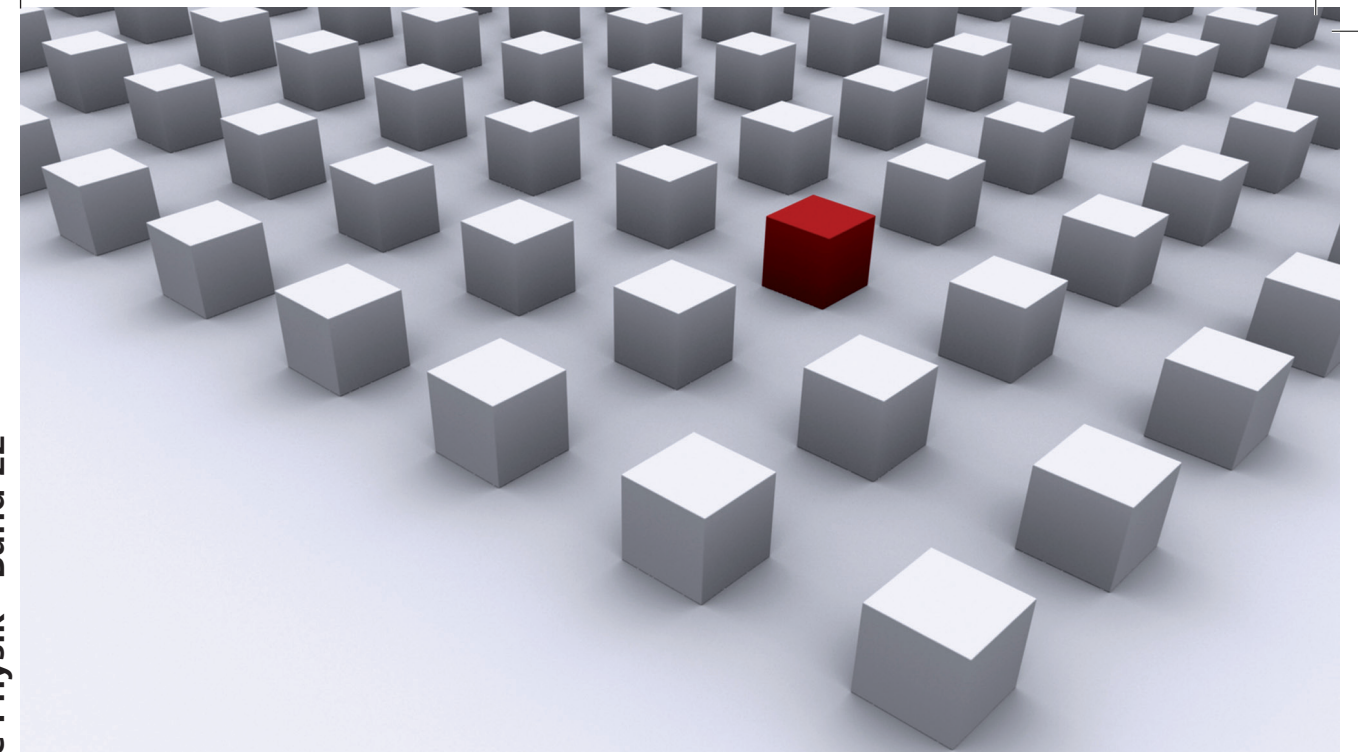
Universitätsverlag Regensburg

Johannes Karch

Johannes Karch

Orbital Photocurrents Induced by Terahertz Laser Radiation in Multi-Valley Semiconductors

Universitätsverlag Regensburg

22

Dissertationsreihe Physik

Universität Regensburg

Johannes Karch

Orbital Photocurrents Induced
by Terahertz Laser Radiation
in Multi-Valley Semiconductors

Orbital Photocurrents Induced
by Terahertz Laser Radiation in Multi-Valley Semiconductors

Dissertationsreihe der Fakultät für Physik der Universität Regensburg, Band 22

Johannes Karch

**Orbital Photocurrents Induced
by Terahertz Laser Radiation
in Multi-Valley Semiconductors**

Orbital Photocurrents Induced by Terahertz Laser Radiation in Multi-Valley Semiconductors

DISSERTATION

zur Erlangung des Doktorgrades der Naturwissenschaften

doctor rerum naturalium

(Dr. rer. nat.)

der Fakultät für Physik

Universität Regensburg

im Mai 2011

vorgelegt von

Dipl.-Phys. Johannes Karch

geboren am 18.01.1983 in Eichstätt

Die Arbeit wurde von Prof. Dr. Sergey D. Ganichev angeleitet.

Das Promotionsgesuch wurde am 5. Mai 2011 eingereicht.

Das Kolloquium fand am 20. Juli 2011 statt.

Prüfungsausschuss:

Vorsitzender:	Prof. Dr. Klaus Richter
1. Gutachter:	Prof. Dr. Sergey D. Ganichev
2. Gutachter:	Prof. Dr. Christian Schüller
weiterer Prüfer:	Prof. Dr. Christian Back

Contents

1   Introduction

The ongoing tremendous interest in graphene relies on both its providing access to fundamental physics and its great potential for future applications. The extraordinary electronic band structure of this novel material, being responsible for the treatment of graphene's charge carriers as massless, Dirac-like particles, enables quasi-relativistic experiments in a solid state environment [1–3]. Moreover, the ultra-high mobilities observed in graphene together with its perfect two-dimensionality may lead to substantially faster nanoelectronic devices than realized by any conventional transistor [4–7]. This is why A. Geim and K. Novoselov have been awarded already six years after their first realization of exfoliated graphene [4] with the Nobel prize in physics 2010 "for groundbreaking experiments regarding the two-dimensional material graphene".

One peculiarity of graphene, which attracted considerable attention, is its valley degree of freedom. Electrons (or holes) can occupy two inequivalent energy band minima, the so called Dirac points K and K' at the corners of the first Brillouin zone, whose low energy environment is characterized by a linear dispersion. This prompts the basic concept to utilize the valley state as additional degree of freedom, analogous to the charge carrier's spin, for the design of new types of solid-state devices [8–10]. The conventional bipolar electronics relies, thereby, only on the crude fact that free carriers in solids can carry both positive and negative electric charge. However, the additional degeneracies enable one to engineer various distributions of carriers in the momentum, spin, and valley spaces. A controllable way of occupying a particular spin state or filling a particular valley is a key ingredient for spintronics [11] or valleytronics [8,12], respectively, both aimed at the development of novel electronic devices characterized by less power dissipation. Candidates appropriate for the realization of valleytronics concepts include besides graphene also other multi-valley semiconductors such as carbon nanotubes [12] or silicon [12, 13].

In this work, photocurrents induced by terahertz (THz) laser radiation are employed to study optoelectronic transport phenomena in graphene as well as in silicon both being multi-valley semiconductors. By the investigation of photo induced electric currents in graphene, a novel Hall effect, driven by the

crossed alternating electric and magnetic fields of circularly polarized light was discovered, which we named circular ac Hall effect (CacHE) [14,15]. This new phenomenon is very general and may occur in a great variety of materials. However, graphene offers an ideal model system, as the perfect two-dimensionality of its honeycomb lattice prohibits the carriers' motion perpendicular to the layer. Therefore, the appearance of other photocurrents, which usually mask the CacHE in conventional systems, is forbidden. The circular ac Hall effect, which can generally be treated as high frequency Hall or photon drag effect, may also deliver information on the underlying electron dynamics in graphene and, thus, provides a new access to the understanding and application of carbon based nanostructures.

Additionally, it is demonstrated that in multi-valley semiconductors currents can be induced by circularly as well as linearly polarized light in each individual valley with different directions in the momentum space. This work shows that they can form pure valley-orbit currents or, by summing up all of these individual flows, a measurable electric current. So far, valley currents are only predicted by theoretical proposals [8–10,12,13,16], but have not been observed in experiments. Here, a vivid evidence of the existence of pure valley-orbit currents is found [17]. Furthermore, it is demonstrated that the individual control of electron fluxes in valleys can be achieved by the excitation of (111)-oriented Si-metal-oxide-semiconductor (Si-MOS) structures with polarized light.

The focus of this work is mainly on helicity driven currents characterized by changing the carrier flow's direction upon flipping the sign of circular polarization from right- to left-handed. Up to now, the discussion about microscopic origins of helicity driven photocurrents has usually been based on the spin-dependent excitation or scattering of electrons and holes by light in materials with strong spin-orbit interaction. Within this framework, the angular momentum of circularly polarized photons is transferred to the carriers generating an unbalanced spin distribution in spin-split subbands. The optical spin injection may yield helicity dependent photocurrents like the circular photogalvanic effect (CPGE) [18,19] or the spin-galvanic effect (SGE) [20].

However, in the relatively light elements C and Si spin-orbit coupling becomes weak [21] and, therefore, spin-related origins of the photocurrents are ineffec-

tive. Thus, a novel access to explain these currents is required, involving pure orbital, i.e. spin-unrelated mechanisms. This means that rather the orbital motion of charge carriers causes, in the presence of an asymmetry in the photoexcitation or carrier relaxation process, a directed particle flow. The orbital trajectory can, thereby, be treated either classically or by a quantum mechanical picture, what is determined by the studied frequency range and by material parameters like the relaxation time and Fermi energy. An illustrative example for a classical model is the high frequency Hall effect, which, as mentioned above, is studied in graphene in this work. Moreover, also the quantum mechanical origin of orbital photocurrents is explored, here, in two-dimensional silicon structures, since the Fermi level in this indirect semiconductor lies much lower than in typical graphene. The helicity driven, purely orbital photocurrent in Si originates from the quantum interference of different pathways of carrier intra- or inter-subband transitions contributing to the light absorption. This results in an imbalance of electrons in the momentum space or, correspondingly, in an electric current [22, 23].

This dissertation is organized as follows. Chapter 2 starts with theoretical basics being important for the studied photocurrents. After introducing the Drude-Lorentz law of high frequency conductivity, THz radiation induced electric currents based on this absorption process and the peculiarities of the used materials, graphene and silicon, are discussed. The experimental methods including the functionality of the THz lasers and polarizers as well as the whole experimental setup are implemented in Chap. 3. Furthermore, details and properties of the studied samples are presented. Based on these fundamentals, Chap. 4 deals with the experimental findings in graphene and their theoretical illustration by means of the CacHE model, as well as with preliminary results identified as edge photogalvanic effect. Afterwards, experiments concerning valley-orbit currents are addressed in Chap. 5. They are studied in (111)-oriented two-dimensional silicon and explained by a mainly phenomenological theory. Finally, the orbital mechanisms underlying the photocurrent generation in silicon are experimentally investigated and theoretically discussed, first with the quantum mechanical model and then with the classical high frequency conductivity in an asymmetric carrier confinement realized in Si-MOS field-effect-transistors (Si-MOSFETs).

2 Theoretical basics

In the following, a brief overview of the theoretical basics of electric currents induced by THz radiation is presented. The chapter starts with the Drude-Lorentz law of high frequency conductivity being the dominant mechanism for the absorption of an electromagnetic THz field and, as a consequence, for the generation of a directed electric current. Afterwards, these photo induced currents are discussed in more detail, starting with some general phenomenological equations. Furthermore, important examples of THz radiation induced currents are introduced by commonly considered model pictures. Among them, the photon drag effect (PDE) caused by the momentum transfer of photons to charge carriers is outlined by means of a microscopic model for intrasubband absorption. Anymore, the microscopic origins of the photogalvanic effects caused by linearly (LPGE) as well as circularly (CPGE) polarized radiation are discussed. Thereby, the LPGE can be considered as a kind of classical ratchet effect and the CPGE as transfer of the photons' angular momentum into a directed motion of free carriers within spin-split subbands. Since this work deals with the experimental study of photocurrents in multi-valley semiconductors, some characteristic features and peculiarities of the ideal two-dimensional (2D) material graphene are presented. Finally, the functionality of usual 2D nanostructures based on conventional semiconductors as well as the phenomenon of quantum-confinement in two dimensions, especially in silicon MOSFETs, are addressed briefly.

2.1 Drude-Lorentz law of high frequency conductivity

In the Drude model of free electrons in metals describing the fundamentals of electrical conductivity of solids, the valence electrons are not bound to the atoms of the solids and build a free electron gas, which can be treated by the kinetic gas theory. If an electric field $\boldsymbol{E}$ is applied to this system (see Fig. 1(a)), the electrons are accelerated and collide with the positively charged ions of the system, until they reach the steady state, where the mean velocity of the electrons is proportional to the field strength. Such scattering events are characterized by the average time between two collisions, the so called

momentum relaxation time τ. In fact, this model can also be applied to doped semiconductors, where the mass of free electrons m is just replaced by the effective mass m^* accounting for the conduction and valance band structure of the semiconductor. The Newton's equation of motion for this process driven by the constant force $\boldsymbol{F} = -e\boldsymbol{E}$ is given by

$$m^* \frac{d\boldsymbol{v}}{dt} + \frac{m^*}{\tau}\,\boldsymbol{v}_\mathrm{D} \;=\; -e\boldsymbol{E}\,, \tag{1}$$

where $\boldsymbol{v}$, $\boldsymbol{v}_\mathrm{D}$ and e are the electron's velocity, drift velocity and charge, respectively [24]. In the steady state, the electron acceleration vanishes yielding a drift velocity

$$\boldsymbol{v}_\mathrm{D} \;=\; \frac{-e\tau}{m^*}\,\boldsymbol{E} \tag{2}$$

and, thus, the current density

$$\boldsymbol{j} \;=\; -eN\boldsymbol{v}_\mathrm{D} \;=\; \frac{e^2\tau N}{m^*}\,\boldsymbol{E}\,, \tag{3}$$

with N being the carrier concentration. Therefore, the dc conductivity σ_0 is given via Ohm's law by the Drude formula [25]

$$\sigma_0 \;=\; \frac{\boldsymbol{j}}{\boldsymbol{E}} \;=\; \frac{e^2\tau N}{m^*}\,. \tag{4}$$

Equation (1) represents the equation of a damped harmonic Lorentz oscillator without the influence of a restoring force by displacing the charge carriers:

$$m^* \frac{d^2\boldsymbol{x}}{dt^2} + m^*\,\gamma\,\frac{d\boldsymbol{x}}{dt} \;=\; -e\boldsymbol{E}\,, \tag{5}$$

where $\boldsymbol{x} = \boldsymbol{x}(t)$ is the displacement of the electrons with respect to the atoms and γ the damping rate as consequence of the energy losses due to collisional processes. Thus, the free electrons are oscillating relative to the fixed atoms of the solid due to their much lower mass, forming oscillating dipoles.

In the following, the interaction between an alternating electric field of a light wave $\boldsymbol{E}(t) = \boldsymbol{E}\mathrm{e}^{-\mathrm{i}\omega t}$ with the angular frequency ω and a semiconductor consisting of fixed ions and free electrons with the effective mass m^* is considered. Thus, Eq. (5) can be solved by substituting $\boldsymbol{x} = \boldsymbol{x}_0\,\mathrm{e}^{-\mathrm{i}\omega t}$ resulting in a time-dependent electron velocity

$$\boldsymbol{v}(t) \;=\; \frac{-e\tau}{m^*}\,\frac{1}{1 - \mathrm{i}\omega\tau}\,\boldsymbol{E}\,\mathrm{e}^{-\mathrm{i}\omega t}\,. \tag{6}$$
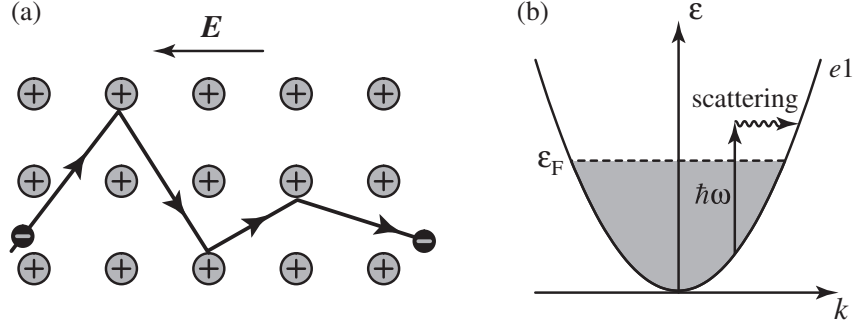
Figure 1: Model of (a) the Drude conductivity by means of scattered electrons on fixed ions and (b) Drude absorption process within the lowest subband accompanied by phonon scattering.

From this equation directly follows via Eqs. (3) and (4) the ac or high frequency conductivity

$$\sigma(\omega) \;=\; \frac{e^2 \tau N}{m^*} \frac{1}{1 - \mathrm{i}\omega\tau} \;=\; \sigma_0 \frac{1 + \mathrm{i}\omega\tau}{1 + (\omega\tau)^2} \,, \tag{7}$$

consisting of a real and an imaginary part. The imaginary part of the conductivity indicates that the electric current lags behind the electric field of the light. This is caused by the fact that the electrons need roughly the time τ to accelerate in response to a change of the applied alternating electric field. This phenomenon increasing with higher angular frequencies ω is also called retardation [26].

Drude conductivity as described above is responsible for the absorption of radiation in a wide range above the plasma frequency. The physical model being usually referred to explain Drude absorption includes the optical excitation of charge carriers into virtual states followed by scattering processes [27]. Thereby, the intermediate states can be chosen, e.g., in other electronic subbands, the valence band or size quantized levels in the case of 2DEGs. In a semiconductor, the light absorption process yielding an electric current can physically be described as follows. The presence of free carriers leads at small light frequencies to the absorption of photons, also called free carrier absorption. Therefore, Fig. 1(b) shows the first parabolic conduction subband of an n-type semiconductor filled up to the Fermi level ε_F determined by the free carrier density N. The absorption of a photon with the energy $\hbar\omega$ excites an

electron from an occupied state below ε_F to an empty level above the Fermi energy. As the photon carries only a small momentum compared to the electron, an additional scattering process has to occur to change the momentum of the electron and, thus, to fulfill the momentum conservation law. Such a supporting scattering process can be realized by the emission or absorption of phonons or the scattering on impurities [24]. Under certain conditions discussed in the next chapters, this may lead to a directed electric current.

2.2   THz radiation induced electric currents

The absorption of homogeneous terahertz radiation in homogeneous materials induces photocurrents, which can phenomenologically be described by the expansion of the current $\boldsymbol{j}$ in powers of the electric field $\boldsymbol{E} = \boldsymbol{E}(\omega, \boldsymbol{q})$ inside the excited medium at the radiation's angular frequency ω and wavevector $\boldsymbol{q}$. For this purpose, there is no need for the knowledge of microscopic models. Since in the THz range the photon energy is smaller than the band gap of usual semiconductors, THz radiation induced electric currents appear neither due to an inhomogeneity of optical excited electron-hole pairs, as in the Dember or the photoelectromagnetic effect, nor due to an inhomogeneity of the sample, as in the conventional photovoltaic effect in p-n junctions [28]. Instead, the far-infrared radiation causes a redistribution of carriers in both the momentum space and the energy and, correspondingly, a directed electric current without an externally applied bias [29].

2.2.1   Phenomenological theory

In the lowest nonvanishing order of a Fourier expansion, the density of a directed current (dc) can phenomenologically be written as response

$$j_\lambda(0,0) \;=\; \sigma^{(2)}_{\lambda\nu\mu}(\omega, \boldsymbol{q}) \, E_\nu(\omega, \boldsymbol{q}) \, E_\mu^*(\omega, \boldsymbol{q}) \tag{8}$$

to the electric field of a plane electromagnetic wave

$$\boldsymbol{E}(t) \;=\; \boldsymbol{E}(\omega, \boldsymbol{q}) \, \mathrm{e}^{-\mathrm{i}\omega t} + \boldsymbol{E}^*(\omega, \boldsymbol{q}) \, \mathrm{e}^{\mathrm{i}\omega t} \,. \tag{9}$$

Here, $E_\nu^* = E_\nu^*(\omega) = E_\nu^*(-\omega)$ is the complex conjugate of E_ν, λ, μ and ν are the Cartesian coordinates, and the expansion coefficient $\sigma_{\lambda\nu\mu}^{(2)}(\omega, \boldsymbol{q})$ is the second-order high-frequency conductivity. In the general case of anisotropic materials, the conductivity, already given by Eq. (7), is a complex third rank tensor. Thus, the electric current $\boldsymbol{j}$, averaged in time and space, can be regarded as a second-order nonlinear steady-state response to an alternating electric field, since the expression given by Eq. (8) contains twice the electric field (corresponding to optical absorption). Further, the tensor $\boldsymbol{\sigma}^{(2)}(\omega, \boldsymbol{q})$ can be expanded in powers of the wavevector $\boldsymbol{q}$ yielding the first two terms

$$\sigma_{\lambda\nu\nu}^{(2)}(\omega, \boldsymbol{q}) \;=\; \chi_{\lambda\mu\nu}(\omega, 0) \;+\; T_{\lambda\delta\mu\nu}(\omega)\, q_\delta \,. \tag{10}$$

Therefore, the electric current density being linear in the intensity is given by

$$j_\lambda \;=\; \underbrace{\sum_{\mu,\nu} \chi_{\lambda\mu\nu}\, E_\mu E_\nu^*}_{\text{Photogalvanic Effect}} \;+\; \underbrace{\sum_{\delta,\mu,\nu} T_{\lambda\delta\mu\nu}\, q_\delta E_\mu E_\nu^*}_{\text{Photon Drag Effect}}\,, \tag{11}$$

where the expansion coefficients $\chi_{\lambda\mu\nu}$ and $T_{\lambda\delta\mu\nu}$ are third and fourth rank tensors, respectively.

A symmetry analysis of the underlying system determines the nonvanishing components of the tensors and yields currents in different directions for various polarization states of the light. For structures belonging to very high symmetry classes for example, all tensor components can vanish and, therefore, no electric current is allowed by symmetry considerations. Note that, in the following, the complex amplitude of the electric field is sometimes written as $\boldsymbol{E} = E\boldsymbol{e}$ with the real amplitude E and the complex unit vector of the light polarization $\boldsymbol{e}$ ($|\boldsymbol{e}|^2 = 1$). The first term on the right-hand side of Eq. (11) represents the photogalvanic effects, which are examined more closely in Chap. 2.2.3, the second term containing the wavevector describes the photon drag effect [15], being the topic of Chap. 2.2.2.

The photogalvanic effects characterized by the third rank tensor $\boldsymbol{\chi}$ can phenomenologically be separated into a purely real and a purely imaginary term sensitive to linearly (or unpolarized) and circularly polarized light, respectively. Similar to the external product $E_\mu E_\nu^*$ of the electric field components, which

can be decomposed into the sum of a symmetric and an asymmetric product regarding the interchange of ν and μ,

$$E_\mu E_\nu^* \;=\; \{E_\mu E_\nu^*\} \;+\; [E_\mu E_\nu^*] \;, \tag{12}$$

with

$$\{E_\mu E_\nu^*\} \;=\; \frac{1}{2}\left(E_\mu E_\nu^* + E_\nu E_\mu^*\right) \;\; \text{and} \;\; [E_\mu E_\nu^*] \;=\; \frac{1}{2}\left(E_\mu E_\nu^* - E_\nu E_\mu^*\right) \;, \tag{13}$$

also the tensor $\boldsymbol{\chi}$ can be written as sum of a real symmetric and an imaginary asymmetric part. Thereby, the two indices of the imaginary term can be further contracted by means of the totally antisymmetric Levi-Civita tensor $\delta_{\rho\mu\nu}$ to only one pseudo vector index,

$$\sum_{\mu,\nu} \chi_{\lambda\mu\nu}\,[E_\mu E_\nu^*] \;=\; \mathrm{i}\sum_{\rho,\mu,\nu} \gamma_{\lambda\rho}\,\delta_{\rho\mu\nu}\,[E_\mu E_\nu^*] \;=\; \sum_{\rho} \gamma_{\lambda\rho}\,\mathrm{i}\left(\boldsymbol{E}\times\boldsymbol{E}^*\right)_\rho, \tag{14}$$

where $\gamma_{\lambda\rho}$ is a second rank pseudo tensor. Finally, Eq. (8) can be written as a sum of the linear and the circular photogalvanic effect, which require the lack of an inversion center in the symmetry point group of the system, and the photon drag effect, which is allowed in both centrosymmetric and noncentrosymmetric media [28–31]:

$$j_\lambda \;=\; \underbrace{\sum_{\mu,\nu} \chi_{\lambda\mu\nu}\{E_\mu E_\nu^*\}}_{\text{LPGE}} \;+\; \underbrace{\sum_{\rho} \gamma_{\lambda\rho}\mathrm{i}\left(\boldsymbol{E}\times\boldsymbol{E}^*\right)_\rho}_{\text{CPGE}} \;+\; \underbrace{\sum_{\delta,\mu,\nu} T_{\lambda\delta\mu\nu}q_\delta E_\mu E_\nu^*}_{\text{PDE}}, \tag{15}$$

where $\chi_{\lambda\mu\nu} = \chi_{\lambda\nu\mu}$. These three terms, representing the linear (LPGE) and circular (CPGE) photogalvanic as well as the photon drag effect (PDE), are discussed in more detail in the next chapters.

2.2.2   The photon drag effect

The possibility to generate a directed carrier flow in semiconductors by the linear momentum of absorbed photons and, thus, by the radiation pressure, was theoretically predicted already in 1935 [32], and treated at the classical frequency limit, where the photon energy is smaller than the typical electron energy, in 1954 [33]. In this classical range, the PDE can be explained in

terms of the ordinary Hall effect, where the crossed electric and magnetic fields of the incident radiation cause a Lorentz force, and, hence, is sometimes called high frequency Hall effect. Afterwards, the PDE was observed in the bulk cubic semiconductor germanium [34, 35] and later also in low-dimensional structures [29]. As the current j is mediated by a fourth rank tensor T with both twice the electric field E (corresponding to absorption of radiation) and the photon momentum q, there is no symmetry restriction for this effect. Thus, in contrast to ordinary optical and photoelectrical phenomena exhibiting an isotropic behavior in crystals of cubic symmetry, the photon drag processes may be anisotropic even in cubic crystals. These general symmetry considerations exemplify that a directed current caused by the illumination of semiconductors does not only flow collinear to the light propagation (longitudinal PDE), but can also be generated transversally to the light's wavevector (transversal PDE). The microscopic reason for it is the anisotropy of isoenergetic surfaces in the momentum space and of dipole matrix elements in certain crystals [29].

It is convenient to separate the PDE, similarly to the photogalvanic effects, into terms caused by linearly polarized or unpolarized light (symmetrical part of the tensor T in Eq. (15)) as well as by elliptically or circularly polarized radiation (asymmetrical part):

$$j_\lambda = \underbrace{\sum_{\delta,\mu,\nu} \widetilde{T}_{\lambda\delta\mu\nu}\, q_\delta\, E_\mu E_\nu^*}_{\text{Linear PDE}} + \underbrace{\sum_{\delta,\rho} \Phi_{\lambda\delta\rho}\, q_\delta\, \mathrm{i}\,(\boldsymbol{E} \times \boldsymbol{E}^*)_\rho}_{\text{Circular PDE}}, \qquad (16)$$

where the fourth rank tensor $\widetilde{T}$ describes the linear and the third rank tensor Φ the circular photon drag effect. The circular PDE, sensitive to the helicity of light, was phenomenologically discussed in the early 1980s [36, 37] and observed in GaAs quantum wells in the mid-infrared range quite recently [38].

The photon drag effect can occur for different types of optical absorption processes like free carrier (Drude) absorption or direct transitions between valence as well as between size-quantized subbands, Rashba-Dresselhaus spin-split subbands, interband transitions and impurity photoionization, and Landau levels or Zeeman split subbands [29]. In the following, the PDE is microscopically explained using the example of Drude absorption within one electronic subband, see Fig. 2, since this mechanism is mostly responsible for the effect in
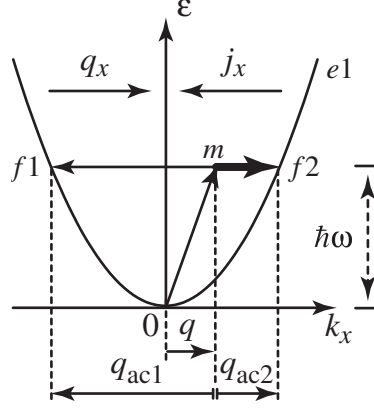
Figure 2: Model of the photon drag effect due to Drude absorption.

the terahertz range. Here, the transfer of the light's quasimomentum to the free carriers results in an asymmetric distribution in the momentum space and, hence, in an electric current. Such a free carrier absorption by indirect transitions inside one subband, represented by the tilted vertical arrow, is only allowed in the presence of phonons or impurities etc. to fulfill the momentum conservation law. Therefore, an optical transition caused by a photon of energy $\hbar\omega$ and wavevector $\boldsymbol{q}$ from, e.g., $k_x = 0$ can only take place via a virtual intermediate state m by emitting or absorbing an acoustic phonon. Hereby, the energy of acoustic phonons can be neglected compared to the photon energy even in the THz range, while they are able to deliver a quasimomentum (wavevector), shown by horizontal arrows from the intermediate to the final states $f1$ and $f2$ with different wavevectors q_{ac1} and q_{ac2}, respectively. This difference, caused by the momentum $\boldsymbol{q}$ of the absorbed photon, yields unequal probabilities of scattering (see the arrows' different thickness) to positive and negative k_x and, thus, an electric current j_x due to the imbalance of the electron distribution in the momentum space [29].

2.2.3   The photogalvanic effects

While the photon drag effect may occur even in materials possessing an inversion center, a different root of photocurrents arises in media lacking the spatial inversion, where the small wavevector $\boldsymbol{q}$ of the radiation needs not to be con-

sidered. Here, a homogeneous optically excitation can result in photogalvanic effects (or photovoltaic effects [31]). They are separated, depending on the polarization state of the light, into the linear and circular photogalvanic effect.

2.2.3.1 The linear photogalvanic effect: The LPGE current is described by the first term of Eq. (15) being symmetric in the last two indices,

$$j_\lambda^{\text{LPGE}} = \sum_{\mu,\nu} \chi_{\lambda\mu\nu} E_\mu E_\nu^* = \sum_{\mu,\nu} \chi_{\lambda\mu\nu} \frac{1}{2}(E_\mu E_\nu^* + E_\nu E_\mu^*), \qquad (17)$$

and is caused by excitation with linearly polarized or unpolarized light. The tensor $\boldsymbol{\chi}$ is, therefore, isomorphic to the piezoelectric tensor and exhibits non-vanishing components only in systems lacking an inversion center. As the LPGE is caused by periodically alternating electric fields in the absence of any net force (averaged over one period in time) in systems with sufficiently low symmetry, it can also be understood as a classical microscopic ratchet [39, 40]. This was correctly recognized by P. Reimann in a review paper about ratchet effects in 2002 [41]. Afterwards, the treatment of photogalvanic effects as microscopic ratchets was done more precisely in our group [39, 42]. Hereby, the prerequisites of the ratchet effect, namely the simultaneous breaking of the thermal equilibrium and of the spatial inversion symmetry, are naturally realized by the optical excitation and the system's microscopic structure, respectively [41]. The simplest case of a ratchet is illustrated in Fig. 3(a). Here, the electrons are excited homogeneously with an ac $\boldsymbol{E}$-field of angular frequency ω but without net direction. As the electrons in this model feel an asymmetric sawtooth potential, a restricted motion of the charge carriers along the "easy" direction results and, hence, a directed particle flow $\boldsymbol{i}$ parallel to the applied electric field [41]. In the particular case of the LPGE, the charge carriers are asymmetrically excited in the $\boldsymbol{k}$-space by photons and exhibit an asymmetric momentum relaxation due to scattering on phonons, static defects or other carriers in noncentrosymmetric crystals [28–31].

The appearance of the LPGE can be visualized by a simple model of randomly distributed but identically oriented equilateral triangles acting as asymmetric elastic scattering centers. This model showing the generation of the linear photogalvanic current is relevant for, e.g., two-dimensional GaN/AlGaN
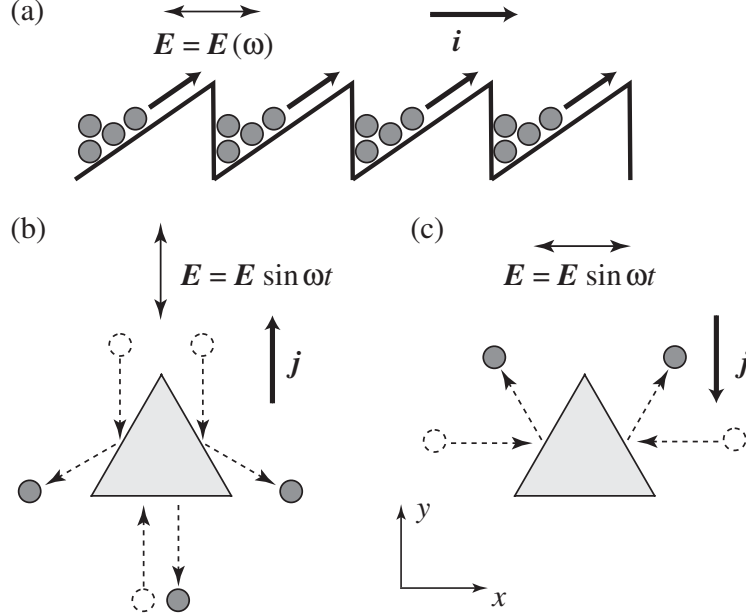
Figure 3: Model of the LPGE. (a) Classical ratchet effect. (b) and (c) Excitation of an asymmetric system with linearly polarized light orientated along the y and x axis, respectively.

structures possessing the C_{3v} symmetry excited by linearly polarized radiation at normal incidence, as pointed out in detail in Ref. [39]. In Fig. 3(b) and (c), a triangle with one side oriented parallel to the x direction is depicted, which illustrates the symmetry properties of the C_{3v} point group and obviously lacks an inversion center. In thermal equilibrium, the velocities of the electrons are isotropically distributed. The application of an external in-plane field $\boldsymbol{E}(t) = \boldsymbol{E}\sin\omega t$ adds an oscillatory motion along this electric field to the random thermal motion of the charge carriers. For a field pointing along the y axis, the scattering results in an electron flow in the $-y$ direction, yielding an electric current $j_y > 0$ shown by the up arrow in Fig. 3(b). By that electron fluxes along the x direction compensate each other and j_x is absent. A variation of the relative direction between the electric field and the orientation of the wedges changes the direction and strength of the carrier flow resulting in a characteristic polarization dependence. It may, e.g., reverse its direction, as shown in Fig. 3(c) for the field oriented along the x axis, or rotate by 90° in the case of $\boldsymbol{E}$ directed at an angle of 45° relative to the y axis. In general, this

mechanism of the LPGE demonstrates a violation of the detailed balance, so that the inequality $W_{\boldsymbol{k},\boldsymbol{k'}} \neq W_{\boldsymbol{k'},\boldsymbol{k}}$ holds for the probabilities of the transition from a state with the momentum $\boldsymbol{k'}$ to the state $\boldsymbol{k}$ and vice versa. This contribution to the linear photogalvanic effect due to carriers having asymmetric distributed velocities is called ballistic contribution [29]. In addition, there exists also the shift contribution to the LPGE being of comparable magnitude. It stems from shifts of the center-of-mass of free-carrier wave-packets in real space by microscopic lengths in quantum transitions. Note that similar contributions to the electric current, called skew-scattering and side-jump currents, also exist in the anomalous Hall effect [39, 43].

2.2.3.2 The circular photogalvanic effect: By illuminating unbiased structures with elliptically or, in particular, circularly polarized light, the circular photogalvanic effect may occur. The characteristic feature of the CPGE is that the current reverses its direction upon changing the helicity of the radiation from right- (σ_+) to left-handed (σ_-) circular polarization. For its appearance the media must belong to a gyrotropic crystal class as a fundamental requirement. Gyrotropy is, thereby, the possibility to couple a polar vector $\boldsymbol{P}$ with an axial vector $\boldsymbol{A}$ (also called pseudo vector) via a pseudo tensor $\boldsymbol{M}$ yielding the relation $P_\lambda = M_{\lambda\rho} A_\rho$. Hence, the corresponding point group symmetry, represented by the pseudo tensor, does not distinguish between the components of polar vectors (e.g., electric current or electron momentum) and of axial vectors (e.g., electron spin or helicity of light) [28, 44–46]. One demonstration of such an interconnection in gyrotropic media was already given by the antisymmetric second term of Eq. (15), where the electric current $\boldsymbol{j}$ is coupled with the cross product $\mathrm{i}(\boldsymbol{E} \times \boldsymbol{E}^*)$ representing an axial vector:

$$j_\lambda^{\mathrm{CPGE}} = \sum_\rho \gamma_{\lambda\rho} \, \mathrm{i} \left(\boldsymbol{E} \times \boldsymbol{E}^* \right)_\rho = \sum_\rho \gamma_{\lambda\rho} \, E^2 \, \hat{e}_\rho \, P_{\mathrm{circ}} \, . \tag{18}$$

Here, $\hat{e}_\rho$ is the unit vector pointing in the light propagation direction and P_{circ} the degree of circular polarization with values between $+1$ for fully right-handed and -1 for left-handed circularly polarized light. Equation (18) builds, therefore, the basic equation of the circular photogalvanic effect. It clearly demonstrates the change in sign upon reversing the helicity from σ_+ to σ_- and

the importance of nonzero components of the pseudo tensor $\boldsymbol{\gamma}$, which requires a sufficiently low symmetry of the studied gyrotropic system and depends on the used coordinate system.
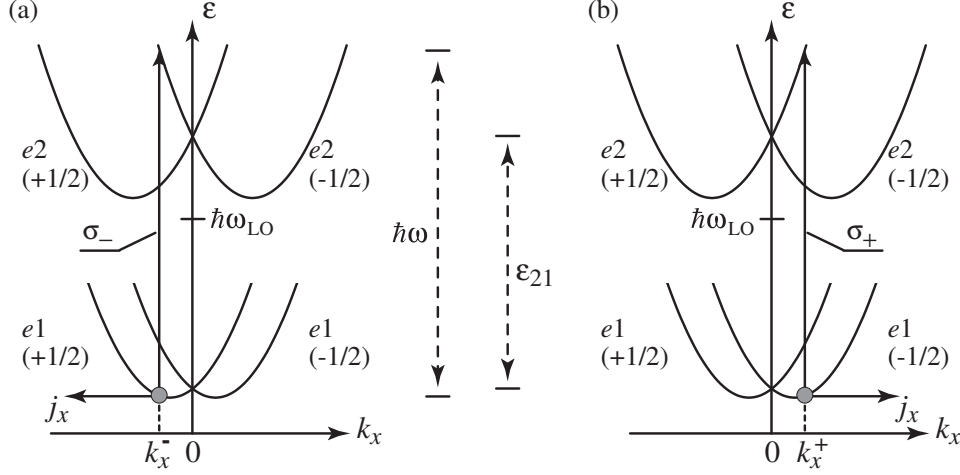
Figure 4: Intersubband model of the CPGE. Transitions between spin split subbands due to (a) left-handed and (b) right-handed circularly polarized light resulting in different current directions j_x.

Usually, spin mechanisms are addressed as microscopic origin of the circular photogalvanic effect [18, 47]. Hence, the absorption of circularly polarized light results in a spin orientation due to the transfer of the photons' angular momentum to a two-dimensional electron system (2DES). Subsequently, a current flow is driven by an asymmetric distribution of the spin polarized carriers in the momentum space. This becomes possible in systems with lifted spin degeneracy due to $\boldsymbol{k}$-linear terms in the Hamiltonian resulting from the spin-orbit interaction [29]. The most elementary microscopic model of the CPGE based on a spin mechanism can, thereby, be illustrated in Fig. 4 for direct intersubband transitions in n-type 2D systems of C_s symmetry having only one mirror plane. Here, the first two size-quantized electronic subbands $e1$ and $e2$ are shown, shifted along k_x due to spin-orbit coupling (for details see, e.g., [21, 48]). As a result of the selection rules of optical transitions caused by circularly polarized light, an electron must flip its spin under absorption of a photon. Therefore, for an optical transition due to normally incident light of given energy $\hbar\omega$, the electron can only be excited from the electronic sub-

band $e1$ with spin $m_s = +1/2$ to the higher subband $e2$ with spin $m_s = -1/2$ by absorbing left-handed circularly polarized light σ_- possessing the angular momentum -1 (see Fig. 4(a)). For a fixed value $\hbar\omega$, the only compatible transition can occur at the wavevector k_x^-. This results in an imbalance in the $\boldsymbol{k}$-space and, hence, an electric current j_x within both subbands $e1$ and $e2$ antiparallel and parallel to x, respectively. Since in n-type heterostructures the energy spacing ε_{21} between the subbands is typically larger than the energy of longitudinal optical phonons $\hbar\omega_{\mathrm{LO}}$, the excited electrons in the higher subband relax rapidly due to phonon emission and do not contribute to the electric current. The resulting current j_x is thereby spin polarized, as it is determined by the photogenerated holes in the electronic ground subband $e1$ with the spin $m_s = +1/2$. Reversing the helicity from left- to right-handed circular polarization σ_+ yields a mirrored picture and a current into the opposite direction with the flipped spin $-1/2$, see Fig. 4(b) [29]. Another possibility to change both the current and the spin direction is the illumination of the structure with a smaller photon energy, not shown in this picture. In this case, the transition also moves successively to positive values k_x^+ and results in an electric current $j_x > 0$ for σ_- light [49, 50].

2.3 Properties of graphene

The novel material graphene, exhibiting an exceptionally high crystal and electronic quality, is the focus of intensive research since its first experimental realization seven years ago [4]. Thus, this chapter deals with the important and interesting peculiarities of this carbon compound. Graphene is a two-dimensional monolayer of graphite building a honeycomb lattice. This hexagonal structure results from the sp^2 hybridization of the carbon atoms yielding three σ bondings to three next neighbors in an angle of $120°$ and, in addition, one π orbital delivering free delocalized conduction electrons. Therefore, graphene can be described as the perfect two-dimensional electronic material feasible in nature, since the carriers are necessarily confined in this strict 2D layer [51]. On the other hand, this was also the reason why graphene, although known as an integral part of three-dimensional materials like, e.g., graphite, was presumed not to exist in the free state. Small thermal fluctuations cause

atomic vibrations perpendicular to the plane, whereby it should get unstable,
roll up and build curved structures such as carbon islands, fullerenes and car-
bon nanotubes. But, in the presence of a substrate, the weak van der Waals
interaction induces adhesive forces between graphene and the wafer. Thus,
free-standing and very stable graphene was unexpectedly fabricated opening
the experimental approach to a great variety of fundamental physics and ap-
plications [52].
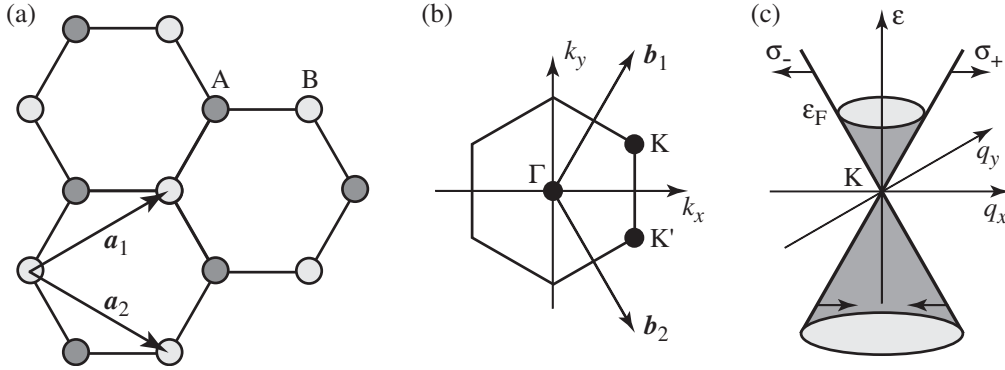
Figure 5: Graphene in (a) real and (b) momentum space. (c) Dirac
cone at the K point filled up to the Fermi energy ε_F providing an n-type
character.

The honeycomb lattice of graphene consists of a triangular lattice with a basis
of two atoms A and B per unit cell, see Fig. 5(a). It is defined by the 2D lattice
vectors $a_1 = (a/2)(3, \sqrt{3})$ and $a_2 = (a/2)(3, -\sqrt{3})$, corresponding to the A and
B sites of the unit cell, respectively. Here, the lattice constant a is given by
the carbon-carbon distance of 0.142 nm. In the reciprocal space, the two
sublattices A and B lead to two inequivalent points K and K' at the corners of
the first Brillouin zone, as they are not connected by a reciprocal lattice vector,
see Fig. 5(b). The locations of these so called Dirac points in the momentum
lattice space are given by K $= (2\pi/3a)(1, 1/\sqrt{3})$ and K' $= (2\pi/3a)(1, -1/\sqrt{3})$.

Calculating the electronic band structure of monolayer graphene shows the
importance of the Dirac points. This was done by P. R. Wallace within the
tight-binding approximation [53], more than half a century before the first
experimental realization of graphene. The analytic energy formula up to the

second-nearest-neighbor hopping term for the conduction (+, anti-bonding π^*) and the valence (-, bonding π) band is given by

$$E_{\pm} \approx 3t' \pm \hbar v_{\mathrm{F}}|\boldsymbol{q}| - \left(\frac{9t'a^2}{4} \pm \frac{3ta^2}{8} \sin(3\theta_q) \right) |\boldsymbol{q}|^2 \,, \tag{19}$$

where $\boldsymbol{q}$ is the momentum measured relatively to the Dirac points, $v_{\mathrm{F}} = 3ta/2\hbar$ is the Fermi velocity, $\theta_q = \arctan^{-1}(q_x/q_y)$ the angle in the momentum space, and $t \approx 2.5$ eV and $t' \approx 0.1$ eV are the nearest-neighbor (between the sub-lattices A-B) and next-nearest-neighbor (inside one sublattice, A-A or B-B) hopping amplitudes, respectively. Hence, for small q relative to the Dirac points and neglecting t', the dispersion relation simplifies to

$$E_{\pm} = \pm \hbar v_{\mathrm{F}} |\boldsymbol{q}| = \pm \hbar v_{\mathrm{F}} \left(q_x^2 + q_y^2 \right)^{1/2} \,. \tag{20}$$

This means that the energy of the upper conduction (+) and the lower valence (-) band depends linearly on the momentum (described by a vanishing effective mass, in this respect like ultra-relativistic particles) and intersects at the Dirac points ($q = 0$) building the so called Dirac cones, for an illustration see Fig. 5(c). The existence of these two equivalent but independent Dirac cones at K and K' results in a two-fold valley degeneracy for graphene. Thus, graphene is a zero band-gap semiconductor or a semimetal with a linear energy dispersion, in contrast to the quadratic energy-momentum relation of usual semiconductors. Graphene's energy dispersion comprising a rather high constant Fermi velocity $v_{\mathrm{F}} = 10^6$ m/s (1/300 of the speed of light) indicates the most distinguishing feature of this material, together with its perfect two-dimensionality.

The existence of two equivalent but independent sublattices A and B results not only in the linear dispersion, but also in a novel chirality in graphene dynamics. Therefore, the two linear branches of the Dirac cone with positive (σ_+) and negative slope (σ_-) become independent of each other, yielding a new quantum number $\boldsymbol{\sigma}$ called (sublattice) pseudospin as natural consequence of the two sublattices. By reversing the motion of an electron, also the pseudospin has to change and realign according to the new direction of the particle. In this manner, the Schrödinger equation for spinless carriers in graphene near the Dirac points is given by

$$-i\hbar v_{\mathrm{F}} \, \boldsymbol{\sigma} \, \boldsymbol{\nabla} \, \Psi(\boldsymbol{r}) = \hbar v_{\mathrm{F}} \, \boldsymbol{\sigma} \, \boldsymbol{k} \, \Psi(\boldsymbol{r}) = E \, \Psi(\boldsymbol{r}) \,, \tag{21}$$

where $\boldsymbol{\sigma} = (\sigma_x, \sigma_y)$ is the 2D vector of Pauli matrices describing the pseudospin and $\Psi(\boldsymbol{r})$ the 2D spinor wavefunction corresponding to the pseudospin symmetry. The chirality, also called helicity, is subsequently given by the helicity operator $\hat{h} = \boldsymbol{\sigma}\boldsymbol{k}/k$ with two eigenvalues $h = \pm 1$ (as $\boldsymbol{\sigma}\boldsymbol{k}\left|\Psi\right\rangle = \pm k\left|\Psi\right\rangle$). Thus, the helicity operator $\hat{h}$ is the projection of the pseudospin $\boldsymbol{\sigma}$ on the momentum axis $\boldsymbol{k}$. This means that in the K valley electrons (holes) have a positive (negative) helicity, and in the K' valley the opposite is valid. Equation (21) is the 2D equation of massless chiral Dirac fermions of velocity v_{F} instead of the speed of light. It directly results from the tight-binding Schrödinger equation for carbon in a honeycomb lattice with two atoms per unit cell. Here, the real spin is neglected and would add an extra spinor structure to the wavefunction of graphene. Note that the massless Dirac description of graphene consequently follows from the intrinsic coupling of the carriers' orbital motion to the pseudospin degree of freedom [1–3, 52, 54, 55].

Besides an intensive study of the unique elastic, thermal and chemical properties, there is an especially great variety of experiments showing interesting physics in a solid state environment caused by the peculiarities of graphene. For example, relativistic effects like Klein tunneling [56] become feasible as consequence of graphene's dispersion relation of a massless relativistic particle [57,58]. Graphene also shows a particular "half-integer" quantum Hall effect (QHE), where the Hall conductivity is shifted about $1/2$ with respect to the usual integer QHE, so that $\sigma_{xy} = \pm 4e^2/h\,(N + 1/2)$ [59,60]. Here, N is the Landau level index and the factor 4 accounts for the double valley and the double spin degeneracy. This effect stems from the quantum electrodynamic-like quantization of the electronic spectrum in graphene in a magnetic field and the chiral motion of the charge carriers [52]. Finally, not only the bulk properties of graphene, but also the surface states of this 2D material (graphene edges) attracted great intention. They can form a armchair (alternating atoms of both sublattices A and B) or zigzag (always the same atom of only one type) structure. At this, zigzag edges always show a metallic character, whereas armchair edges can behave as metal or semiconductor, what consequently strongly influences transport phenomena [1,54].

2.4 Quantum-confinement in Si-MOSFET structures

In contrast to graphene, where a quantum confinement in two dimensions is naturally present due to its monoatomic configuration, in usual semiconductors a 2D electronic system is achieved by growing heterostructures or inversion layers consisting of materials with different band properties. As this work also deals with photocurrents measured in two-dimensional silicon, in the following the quantum confinement on the example of Si metal-oxide-semiconductor-field-effect-transistors (MOSFETs) is discussed. Subsequently, the band structure and valley degeneracy of silicon being of great importance for this work are addressed.

Two-dimensional quantum-confinement means that the electrons are trapped inside some kind of potential well, e.g., between two materials with different bandgaps, by what they can not be treated classically anymore. Hence, their motion is only allowed within the xy plane and forbidden along the z direction, what results in a two-dimensional electron gas (2DEG). The electron transport in such a 2DEG can be described similarly to the Drude model introduced in Chap. 2.1 but is reduced to a 2D plane. In quantum mechanics it is well known that the energy dispersion of 2D confined systems gets quantized in z direction

$$E_n(\boldsymbol{k}) = E_n + \frac{\hbar^2}{2m^*} \left(k_x^2 + k_y^2 \right) , \tag{22}$$

where n is the number of the level occupied by electrons, also called subband. Each energy E_n builds, thus, the bottom of a parabolic subband [61]. In the case of large carrier concentrations, also higher subbands as the ground level E_0 get populated and, strictly speaking, the system is no longer two-dimensional. This is due to the fact that the electrons in higher occupied states are not longer strongly confined in the z direction. In addition, the charge carriers in usual semiconductors are always confined in layers of some finite width (≈ 5 to 50 nm) building only so called quasi-2D systems, where the wavefunction of the electrons is broadened in z direction.

In Si-MOSFETs, this quasi-2DEG emerges at the interface of silicon and its oxide. The complete transistor design is schematically shown in Fig. 6(a) and consists of a p-type Si substrate with source and drain contacts fabricated from
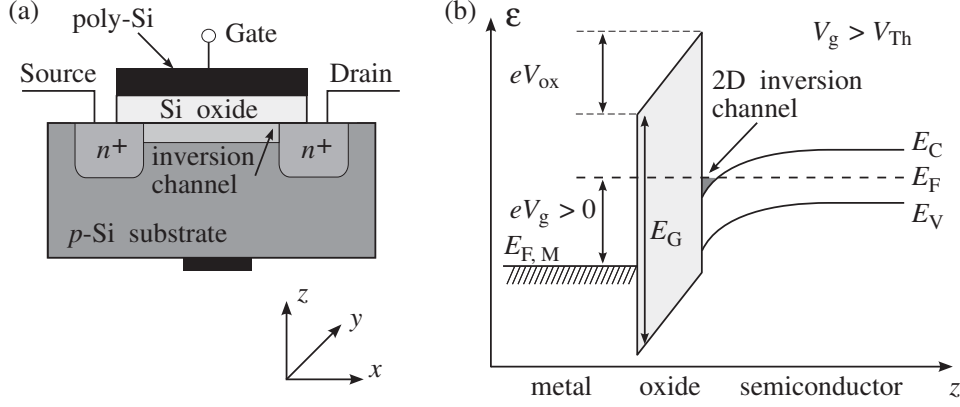
Figure 6: (a) Schematic design and (b) band structure of a Si-MOSFET.

n^+-type Si. A gate made from highly doped polycrystalline silicon (playing the role of a metal) is grown on top of the substrate, separated by an isolating SiO$_2$ layer. Since the gate, the dielectric and the substrate build a capacitor, a positive applied gate voltage results in a charging of the isolating layer with a negative potential on the side near to the interface. Therefore, the holes in the boundary layer are collected by the electric field leaving the negative charged acceptors in this area. This process is called depletion, since the majority carriers get compensated. By reaching a sufficiently high gate voltage above the threshold, $V_g > V_{Th}$, holes are no longer available for recombination and electrons can flow towards the interface and accumulate there. Thus, the electrons build a thin n-type inversion channel consisting of the minority carriers of the substrate. This channel conductively connects the source and drain contacts and enables a current flow between them for an applied source-drain voltage V_{SD}.

Figure 6(b) illustrates the functionality of this MOSFET by means of the corresponding band structure. From left to right one can see the Fermi energy of the metal $E_{F,M}$, the large bandgap of the oxide E_G as well as the conduction band, Fermi and valence band energy of the semiconductor E_C, E_F and E_V, respectively. Without applied gate voltage V_g, the Fermi energy in the silicon substrate lies between the conduction and valence band providing no free carriers for electronic transport. For rising positive gate voltages, conduction as

well as valence band move upwards inside the semiconductor, but their edges are bent downwards near to the interface. Reaching the threshold voltage, the conduction band and the Fermi energy touch each other near the interface, resulting in free carriers in the electronic band. Thus, a 2DEG arises next to the interface characterized by a linearly increasing charge carrier density N for higher applied gate voltages. In addition, changing V_g results also in a lifting of the size-quantized parabolic subbands e_n and e_{n+1} by the energy $\varepsilon_{n+1,n}$ [26, 62–66].
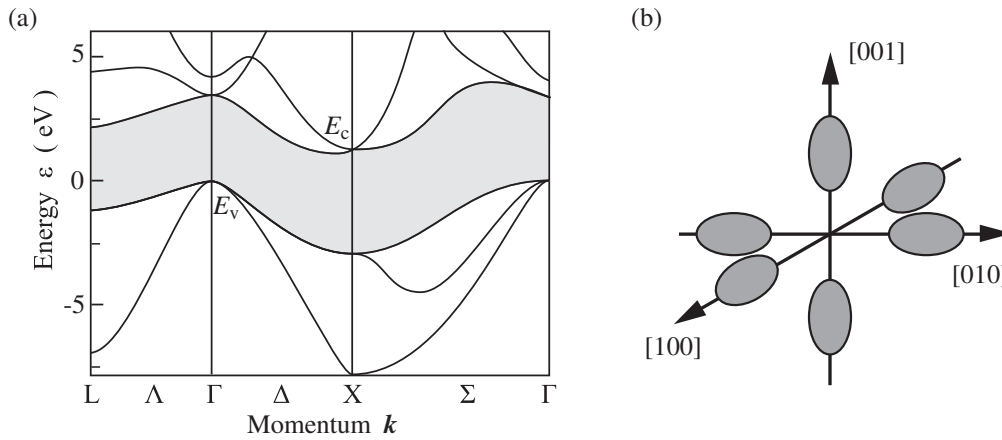
Figure 7: (a) Energy band structure of bulk silicon and (b) constant energy surfaces of the Si conduction band illustrating its six-fold valley degeneracy. The ellipsoids' long axis correspond to the longitudinal effective mass, $m_l = 0.916 m_0$, of electrons in Si and the short axes to the transversal effective mass, $m_t = 0.190 m_0$.

The properties of the two-dimensional electron gas in a Si-MOSFET depend strongly on the crystallographic orientation of the structure. Therefore, the energy band structure of bulk silicon is of importance, see Fig. 7(a). Silicon is an indirect semiconductor with the valence band maximum on the Γ point and six conduction band minima on the X points in the $\langle 001 \rangle$ directions of the first Brillouin zone [27]. Consequently, the constant energy surfaces for the electronic band of this semiconductor crystallizing at the diamond structure consists of six equivalent ellipsoidal minima, see Fig. 7(b). The valleys, which account for the occupation of the momentum space with electrons, are oriented along the [001], [010] and [001] directions and are located at about 85% of the

way to the first Brillouin zone's boundaries. This yields a valley degeneracy of six in bulk silicon. By reducing the dimensionality of Si in the case of inversion layers, the valley degeneracy results from the relative orientation of the 2D interface with respect to the six ellipsoids. Thus, for (001)-, (110)- and (111)-oriented Si the valley degeneracies are 2, 4 and 6, respectively. In this way, each individual valley is generally characterized by a high mass anisotropy and, consequently, a low symmetry [61].

3 Experimental methods

For the observation and experimental investigation of the photocurrents described in the previous chapter, THz laser radiation of various wavelengths and polarizations is employed. Therefore, this chapter is devoted to outline the functionality of the used THz laser source and the optical components for the variation of the light's polarization state, which can be described in vivid terms of polarization ellipses and the Stokes parameters. Afterwards, the complete experimental setup including the electronic devices for signal processing and the power calibration of the system are pointed out. Furthermore, the properties, parameters, geometries and fabrication processes of the studied samples – graphene and Si-MOSFETs – are overviewed.

3.1 Optically pumped molecular THz laser

A valuable tool to effectively generate THz radiation is provided by molecular gas lasers optically pumped by CO_2 lasers. Their advantages are the high power and the fact that they are easy to build and operate [29]. This kind of lasers was discovered by Chang and Bridges in 1969 [67] for continuous wave (cw) operation and extended to the pulsed mode by de Temple in 1974 [68]. Another convenience of these lasers is that they are able to cover a wide range of frequencies with many discrete laser lines. In the following, the pulsed high power THz radiation source, pumped by a transversely excited atmospheric pressure (TEA) CO_2 laser [29, 69, 70], is described in detail. The functionality of the cw molecular gas laser can be treated quite similarly.

A molecular THz laser uses dense lying rotational states as lasing transitions. As active media acts, thereby, a symmetric top molecule, whose vibrational-rotational transitions are pumped optically by a mid-infrared laser. A lot of molecules with only one symmetry axis and a permanent electric dipole moment can be utilized as laser gas, e.g., NH_3, D_2O, CH_3F and CH_3OH [71]. The lasing operation using the example of NH_3, most important for this work, is illustrated in Fig. 8(a). The molecule is excited from the lower ($\nu_2 = 0$) to the upper ($\nu_2 = 1$) vibrational state by the CO_2 laser radiation, whose wavelength range can be tuned from 9.2 to 11.2 µm fitting to many molecular
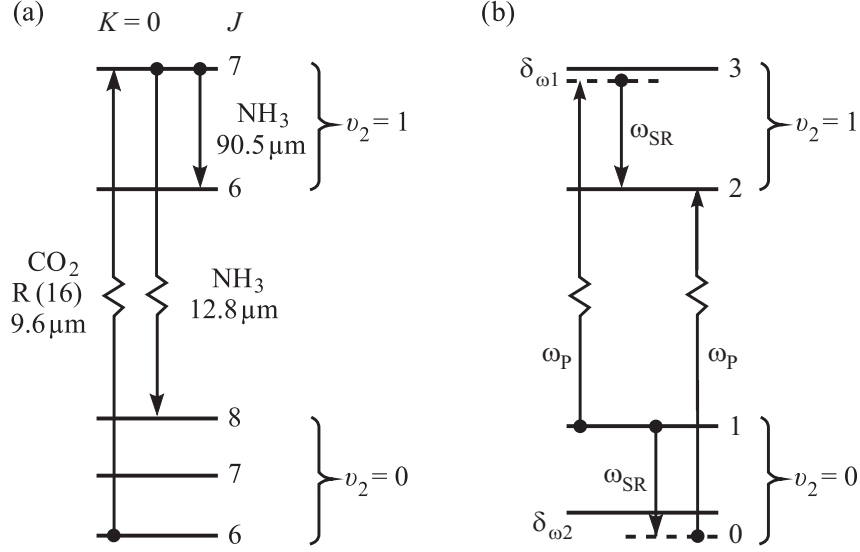
Figure 8: (a) Rotational transitions in the NH_3 molecule after pumping with a certain CO_2 laser line. (b) Principle of Raman transitions.

transitions. Therefore, in both states a population inversion between higher and lower rotational levels and, consequently, a laser action can be achieved. In the case of pumping the NH_3 molecule with the R(16) CO_2 laser line having a mid-infrared (MIR) wavelength of 9.6 µm, the laser process can be obtained within the upper vibrational state from the $J = 7$ to the $J = 6$ rotational level resulting in a THz wavelength of $\lambda = 90.5$ µm. The degree and relative orientation of the linear polarization of the produced THz radiation, which are of great importance for the photocurrent experiments, are determined by the quantum numbers K and J, where K is the projection of the angular momentum J onto the symmetry axis of the molecule. The laser radiation is highly linearly polarized in case that the pump radiation excites molecular states with angular momentum quantum numbers $K \ll J$. If $|\Delta J|$ is identical for pump and THz transitions (like in Fig. 8(a)), the two polarizations are oriented parallel, otherwise they are orthogonal. The reason for this are angular momentum selection rules for pump and lasing transitions. A great number of THz wavelengths lying between 20 and 2000 µm are obtained with this technique by simply choosing different gases as active media for the THz laser or changing the pump frequency of the CO_2 laser.

Due to a strong near resonance interaction not only a laser transition but also a stimulated Raman transition may occur in the optically pumped far-infrared (FIR) system. Moreover, by pumping the active media with high intensities this is the main principle for the generation of THz radiation. Therefore, laser emission can be obtained for a relative high frequency mismatch up to some GHz [72]. This clearly shows the advantage of using the TEA CO_2 laser as pump source, since the produced strong electric field of the light wave yields a broadening of the molecular levels (so called ac Stark shift) and opens the possibility to excite states with an energetic distance deviant from the pumping frequency [68]. In Fig. 8(b) such a Raman scattering process is illustrated for a four-level system, where the pumping frequency ω_p differs from the resonance frequency by δ_{ω_1} in the intermediate or by δ_{ω_2} in the initial state [73]. This demonstrates that Raman scattering is a two-photon process, where a photon of energy $\hbar\omega_p$ is absorbed and a photon of energy $\hbar\omega_{SR}$ is emitted in the second stage [74]. If the emitted Raman energy $\hbar\omega_{SR}$ is smaller than the difference $\hbar(\omega_3 - \omega_2)$ between the rotational levels 2 and 3, the process is called Stokes scattering where, e.g., an additional rotational transition in a molecule or a phonon in a solid is produced, otherwise for $\hbar\omega_{SR} > \hbar(\omega_1 - \omega_0)$ anti-Stokes process. By the excitation of Raman active molecules with a sufficiently high laser intensity, the process of stimulated Raman scattering (SRS) can be observed. In this case, both the pump beam ω_p and the Raman light of frequency ω_{SR} propagate trough the active media. Thus, the Raman transition leads to the absorption of the pump photons and an amplification of the Raman photons, so that the spontaneously emitted Raman line gets exponentially amplified [75]. The SRS, whose intensity is some orders of magnitude larger than in the spontaneous case, is always directed parallel or antiparallel to the pump laser propagation and results in coherent photons having the same
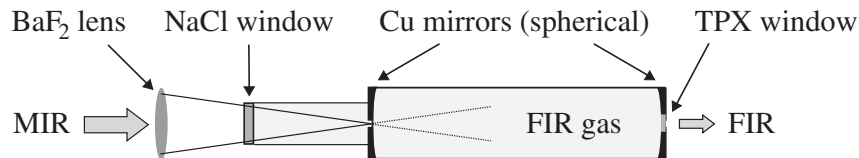

Figure 9: Resonator of the pulsed THz Raman laser with used optical components.

frequency ω_{SR}. This increases the number of possible laser lines which would not be accessible by low-power cw pumping.

The experimental realization of the far-infrared laser employed in the experiment is sketched in Fig. 9. Note that techniques typically used for the neighboring spectral ranges can not be applied to terahertz frequencies. For example, single-mode waveguides widely used in the microwave region can not be employed due to the strong damping of the radiation, whereas glass as the standard material for optical components in the visible and near infrared region is characterized by a strong absorption in the far infrared range. Hence, for a quasi-optical THz setup various crystalline and plastic materials as windows, filters, lenses etc. have to be taken [29]. Below the pulsed THz laser with the used optical components is described in detail. The pulsed high power mid-infrared radiation of a TEA CO_2 laser is focused with a BaF_2 lens through a NaCl window into a glass tube of 1.27 m length and 80 mm diameter. This cavity is filled with NH_3 (for the wavelengths 76, 90, 148 and 280 µm), D_2O (385 µm) or CH_3F (496 µm) as active gases. The gas pressure is an important parameter of the laser emission and lies typically between 1 and 20 mbar. At low pressure, less molecules within the resonator lead to a small laser gain, whereas for high pressures molecular collisions prevent a large population inversion. Thus, it exists an optimal value for each laser line. Two gold coated
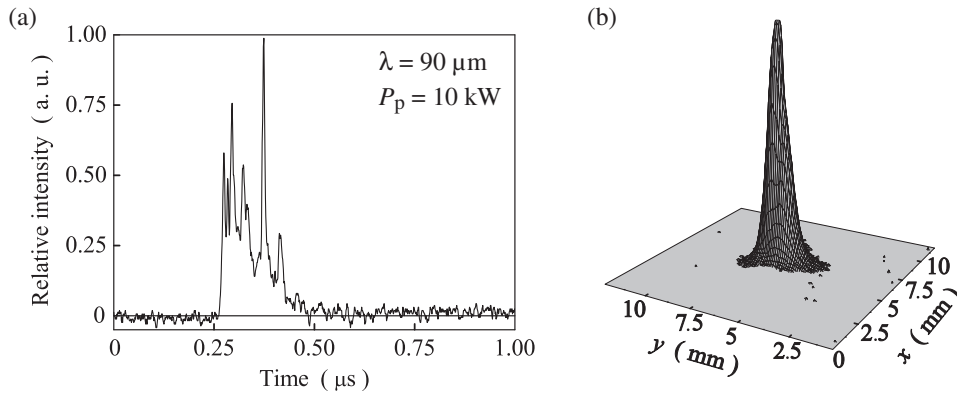

Figure 10: (a) Temporal and (b) spatial beam shape of a THz pulse at a wavelength of $\lambda = 90$ µm, measured by a photon drag detector "PD5F" and a pyroelectric camera "Spiricon", respectively.

spherical copper mirrors with a curvature radius of 1000 mm allow multiple reflections to ensure a maximal absorption of the exciting beam and, hence, to increase the light amplification. Holes in the middle of both mirrors enable to couple in the CO_2 laser beam and out the THz radiation on the other end of the resonator, which is enclosed by a TPX (4-Methylpenthen-1) window. This polymer acts here also as a filter being transparent for the THz laser but not for the MIR pump radiation. All the used optical elements are as well transparent for visible light, which enables the adjustment of the whole setup with a red HeNe laser. The emitted THz pulses have typically a duration of $t_p \approx 100$ ns repeating the pump pulse length of the CO_2 laser and a peak power P_p of several tens of kW depending on the wavelength. As an example, the temporal shape as well as the spatial Gaussian distribution of one pulse at $\lambda = 90$ µm are shown in Fig. 10.

3.2   Variation of the polarization state of light

Radiation emitted by the THz laser is linearly polarized with the $\boldsymbol{E}$-field either vertically or a horizontally oriented depending on the used laser system and wavelength. For the study of the photocurrents in this work, however, both linearly polarized light of different orientations and circularly polarized radiation are crucially needed, as the currents are strongly influenced by the polarization state. For this purpose, $\lambda/2$- and $\lambda/4$-plates were fabricated from birefringent x-cut crystalline quartz, suitable for the THz frequency range. Therefore, in the following the phenomenon of birefringence, the functionality of retardation wave plates and the Stokes parameters, which completely and effectively describe the polarization state of light, are discussed.

Birefringence can occur in optical anisotropic media, especially in uniaxial crystals like x-cut quartz, and means the splitting of one light beam into two partial beams with orthogonal polarizations. The relative intensities of these beams are given by the polarization state of the incident light [76]. Uniaxial crystals are characterized by the same dielectric constants $\varepsilon_x = \varepsilon_z = \varepsilon_\perp$ along two crystal axes x and z and another one $\varepsilon_\parallel = \varepsilon_y \neq \varepsilon_\perp$ parallel to the main symmetry axis or so called optical axis c. Note that hereby the coordinate system is changed from the previous one, which was given by the symmetry of the

birefringent crystal, in such a way that the plate's normal as well as the propagation of light are parallel to $-z$ (instead of x) and the optical axis is oriented along y (instead of z). Light incident normally on such uniaxial crystals yields two values of the refractive index, $n_{\mathrm{o}} = \sqrt{\varepsilon_\perp}$ and $n_{\mathrm{eo}} = \sqrt{\varepsilon_\parallel}$. Hence, the beam is split into an ordinary (o) and an extraordinary (eo) beam propagating with orthogonal polarizations and different velocities. The ordinary beam with the polarization perpendicular to the optical axis (electric field vector $\boldsymbol{E}_\perp$) satisfies the refraction law of Snellius, whereas the extraordinary beam is polarized parallel to the optical axis ($\boldsymbol{E}_\parallel$). In quartz, the refraction index of the extraordinary beam is higher than that of the ordinary ($\Delta n = n_{\mathrm{eo}} - n_{\mathrm{o}} > 0$), hence, the optical axis c defines also the slow axis of the anisotropic crystal. Due to the different propagation velocities in the media, a certain optical retardation Δl or, correspondingly, phase shift $\Delta\phi$ between the two partial beams arise:

$$\Delta l \;=\; d\,(n_{\mathrm{eo}} - n_{\mathrm{o}})\,, \tag{23}$$

$$\Delta\phi \;=\; \frac{2\pi d}{\lambda}\,(n_{\mathrm{eo}} - n_{\mathrm{o}})\,. \tag{24}$$

Consequently, by choosing the adequate thickness d of the plate for a certain wavelength λ, one can introduce a well-defined phase shift between ordinary and extraordinary beam and, thus, vary the polarization state of the incoming light. These retardation plates are widely used in the visible and near-infrared range, but not available for THz frequencies. Therefore, by measuring the difference Δn of the refraction indices in dependence of the wavelength with, e.g., a Fourier transform infrared spectrometer using parallel and crossed polarizers, one can estimate the required thickness of the crystal and fabricate $\lambda/2$- as well as $\lambda/4$-plates for each available wavelength of the THz laser [29, 77, 78].

A $\lambda/2$-plate can be realized by choosing the crystal's thickness d in such a way that a phase shift $\Delta\phi = (2m + 1)180°$ in the order m results for a certain wavelength λ_0. Thus, the zero order condition for the thickness of the plate is given by

$$d \;=\; \frac{\lambda_0}{2}\,\frac{1}{\Delta n}\,. \tag{25}$$

Higher orders of $\lambda/2$-plates ($m \geq 1$) can be produced as well, but result in thicker plates and, thus, stronger absorption of the transmitted radiation. Figure 11(a) illustrates the mode of operation of such a $\lambda/2$-plate. The initial
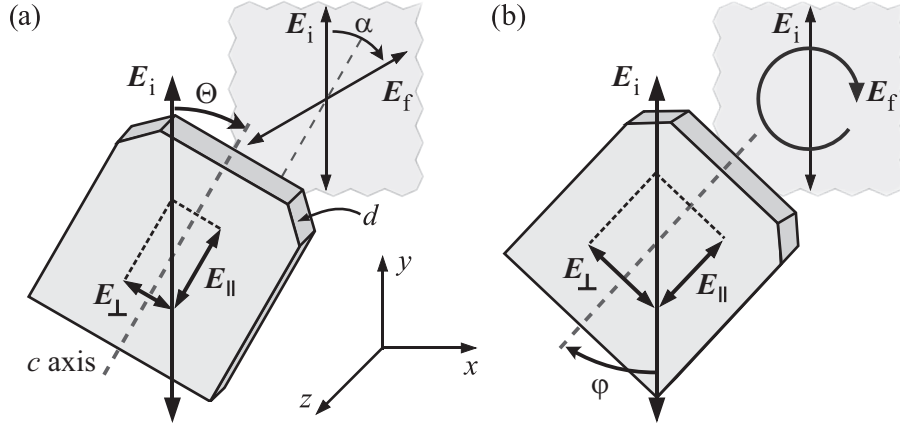
Figure 11: Sketch of (a) a $\lambda/2$-plate rotated about Θ and (b) a $\lambda/4$-plate rotated by the angel $\varphi = 45°$ with initial and final polarizations of the light. Note that the coordinate system is fixed stationary.

electric field vector $\boldsymbol{E}_\mathrm{i}$ of the normally incident beam can be decomposed into components $\boldsymbol{E}_\parallel$ and $\boldsymbol{E}_\perp$ parallel and perpendicular to the optical axis, respectively. The phase shift of 180° between the ordinary and extraordinary beam after passing the plate can be considered as a relative sign change between their polarizations resulting, e.g., in a reflection of $\boldsymbol{E}_\perp$ about the c axis. If the angle between the initial polarization $\boldsymbol{E}_\mathrm{i}$ and the optical axis was Θ, the final polarization $\boldsymbol{E}_\mathrm{f}$ of the beam is rotated by $\alpha = 2\Theta$. Therefore, by rotating the $\lambda/2$-plate about Θ one can achieve every possible azimuth angle α of linear polarization within the xy plane.

A $\lambda/4$-plate, in contrast, can produce circularly (or in general elliptically) polarized light. Here, the thickness of the plate is chosen to achieve a phase shift of $\Delta\phi = (2m + 1)90°$:

$$d = \frac{\lambda_0}{4}\frac{1}{\Delta n}. \tag{26}$$

The angle φ denotes the angle between the initial polarization of the radiation and the c axis of the plate. For a rotation of the plate about $\varphi = 45°$ (or 225°), the two projections $\boldsymbol{E}_\perp$ and $\boldsymbol{E}_\parallel$ have the same absolute value. Hence, the superposition of these two orthogonal linear polarizations, which are phase shifted by 90° against each other, yields circularly polarized radiation (see Fig. 11(b)), in the case of $\varphi = 45°$ with a right-handed sense of rotation (σ_+).

For the angle $\varphi = 135°$ (or $315°$) (in the lowest order $m = 0$), the relative sign between the components is changed resulting in left-handed circularly polarization or, correspondingly, the opposite helicity of the light (σ_-). In the case that φ is a multiple of $90°$, only one partial beam exists and the final polarization state remains unchanged, $\boldsymbol{E}_\mathrm{f} = \boldsymbol{E}_\mathrm{i}$. In general, for any other intermediate angle, the projections have different values and, thus, the light is elliptically polarized.
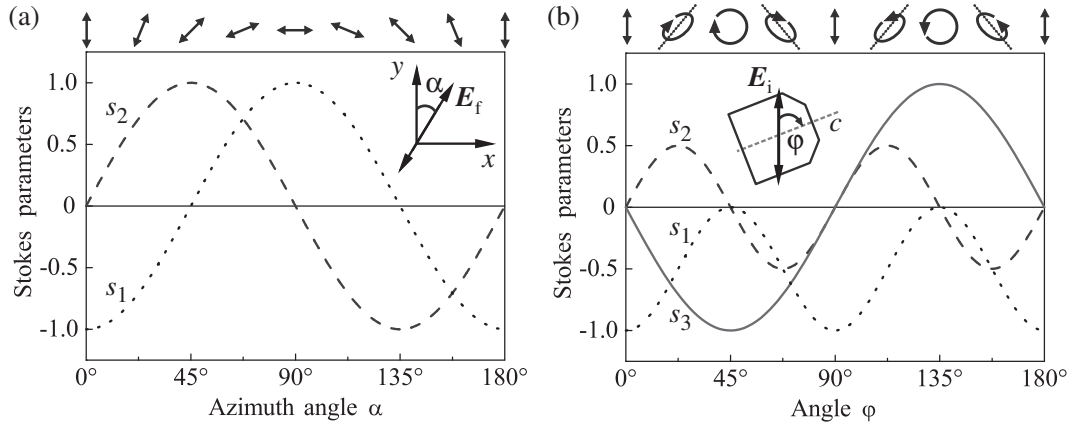
Figure 12: Stokes parameters for the rotation of (a) a $\lambda/2$- and (b) a $\lambda/4$-plate. On top, characteristic polarization states are sketched.

For a complete characterization and description of all these different polarization states, a set of four values $s_0, ... s_3$, introduced by G. G. Stokes in 1852, is commonly used [79–81]. These Stokes parameters are related with the electric field $\boldsymbol{E}$ in the xy plane for a fully polarized monochromatic wave propagating along $-z$ (coordinate system of the sample) as follows:

$$s_0 = |E_x|^2 + |E_y|^2 = |E|^2 = I \,, \tag{27}$$

$$s_1 = |E_x|^2 - |E_y|^2 \,, \tag{28}$$

$$s_2 = E_x E_y^* + E_y E_x^* \,, \tag{29}$$

$$s_3 = \mathrm{i}(E_x E_y^* - E_y E_x^*) = -P_\mathrm{circ} I \,. \tag{30}$$

Here, s_0 does not contain information about the polarization state and determines only the radiation intensity I. The parameters s_1 and s_2, in contrast, describe the linear polarization within the coordinate axes x, y and within the

system rotated about an angle of 45°, respectively. The circular polarization of light – or helicity P_{circ} – is represented by the value of s_3, $+1$ for right-handed σ_+ or -1 for left-handed σ_- circularly polarized radiation. As the retardation plates change the states of polarization, the Stokes parameters vary by rotating the plates depending on the initial laser polarization and the sense of rotation. The experimental configuration of this work is in the majority of cases chosen in such a way that the initial electric field direction is vertical ($\boldsymbol{E}_{\text{i}} \parallel y$) and the plate rotates clockwise. Thus, the Stokes parameters normalized to the intensity are given in this geometry for varying the azimuth angle α by means of the $\lambda/2$-plate as well as rotating the $\lambda/4$-plate about the angle φ by

$$\frac{s_1}{s_0} = \frac{|E_x|^2 - |E_y|^2}{|E|^2} = -\cos 2\alpha = -\frac{1 + \cos 4\varphi}{2} \, , \tag{31}$$

$$\frac{s_2}{s_0} = \frac{E_x E_y^* + E_y E_x^*}{|E|^2} = \sin 2\alpha = \frac{\sin 4\varphi}{2} \, , \tag{32}$$

$$\frac{s_3}{s_0} = \frac{\mathrm{i}(E_x E_y^* - E_y E_x^*)}{|E|^2} = -P_{\text{circ}} = -\sin 2\varphi \, . \tag{33}$$

Other geometries with different initial orientations of the electric field or rotation senses result usually in other signs of s_1, s_2 and s_3. For illustration, the variation of the Stokes parameters given by Eqs. (31)-(33) is also shown in Fig. 12. On top of this figure, characteristic polarization states depending on the angles α and φ are sketched.

The most general state of fully polarized light is represented by elliptically polarized radiation. Therefore, the polarization state can be determined by the orientation and shape of a polarization ellipse, which is traced by the tip of the periodically rotating electric field vector within the xy plane at a fixed value of z. Such an ellipse, as shown in Fig. 13(a), is characterized by the angle ψ determining the direction of the major axis a with respect to x and the angle χ defined as the ratio of the minor to the major axis b/a and, hence, determining the ellipticity. The size of the ellipse is given by the intensity of the wave $I = |E_x|^2 + |E_y|^2$. Thus, the linear and circular polarization states are degenerate cases of this ellipse. If the phase difference $\Delta\phi$ between E_x and E_y gets 0 or π, the angle χ vanishes (since $b = 0$) and the ellipse collapses to a straight line of slope $\pm E_y/E_x$. For the case $\Delta\phi = \pm\pi/2$ and $E_x = E_y$, χ
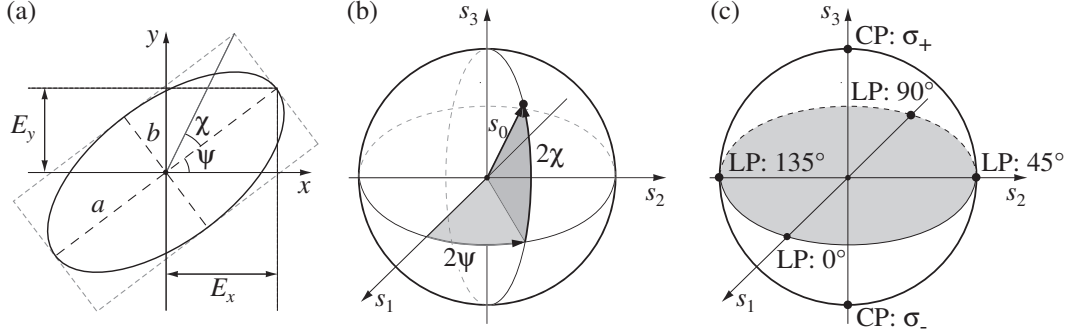
Figure 13: (a) Polarization ellipse. (b) Poincaré sphere with coordinate system. (c) Poincaré sphere showing purely linear (LP) and circular (CP) polarization states.

and ψ get $\pm 45°$ as well as the axes a and b of the ellipse get equivalent, what just describes a circle. All these polarization states can – in relation to the Stokes parameters $s_0, ...s_3$ – also be represented as points on the surface of a so called Poincaré sphere with radius s_0, see Fig. 13(b). Here, the usual spherical coordinate system is given by $r = s_0$, $\theta = 90° - 2\chi$ and $\phi = 2\psi$, and, thus, the three linear independent Stokes parameters as kind of orthogonal coordinate system as functions of the ellipse's angles χ and ψ:

$$s_1 = s_0 \cos 2\chi \cos 2\psi \,, \tag{34}$$

$$s_2 = s_0 \cos 2\chi \sin 2\psi \,, \tag{35}$$

$$s_3 = s_0 \sin 2\chi \,. \tag{36}$$

In this construct, points on the equator $(\chi = 0°)$ represent all possible states of purely linear polarization. For example, $2\psi = 0°$ and $2\psi = 180°$ stand for the polarization along the x and y axes (given by the Stokes parameter s_1), respectively. The linear polarization along the bisector xy (Stokes parameter s_2) is described by the points on the Poincaré sphere $2\psi = 90°$ and $2\psi = 270°$. The north and south pole of this sphere, in contrast, represent right- and left-handed circularly polarized light (Stokes parameter s_3), see Fig. 13(c). All other points on the surface exhibit the general case of elliptical polarization [82].

3.3 Experimental setup and calibration

After the description of the used THz source and all essential optical components for the photocurrent experiments, the complete experimental setup used in this work is discussed in this chapter. As sketched in Fig. 14, all components are linked via the General Purpose Interface Bus (GPIB) or the parallel printer port for a convenient control by a program written in the software LabView. In this manner, this program initiates the pulses of the CO_2 and thereby the FIR laser, drives a step motor, which rotates the retardation plates, and also stores the pulsed signals from the reference detector and the sample. The voltage signals induced by the THz radiation are measured via a 50 Ω load resistor and, after amplification by high frequency electronics, recorded with a 1 GHz digital storage oscilloscope. These fast electronics are needed for a good resolution of the signal shape, as the total THz pulses have a characteristic length of about 100 ns corresponding to a frequency of 10 MHz.
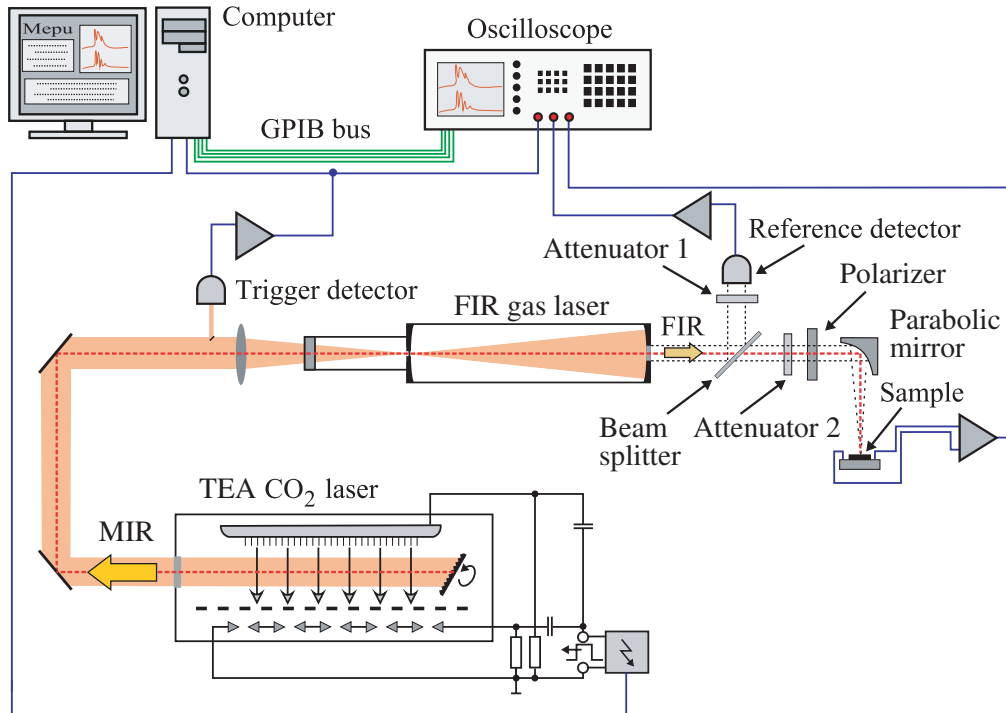

Figure 14: Experimental setup of the pulsed high power THz laser, which is optically pumped by a TEA CO_2 laser.

Since it is crucial for the analysis of the experiments to know the intensity of each pulse acting on the sample, a calibration of the laser system is done in combination with each photocurrent measurement. Therefore, the sample is replaced by a photon drag detector "PD5F" to get the power of each pulse at the position of the sample and, thus, the ratio of the transmitted and reflected parts of the beam after the beam splitter. Due to the calibration, one can measure with the help of the reference detector the intensity reaching the sample for every pulse during the measurement. This has to be repeated for every change of the setup, as, for example, the beam splitter fabricated from a mylar film shows different reflection and transmission characteristics for miscellaneous wavelengths. Furthermore, all optical components, as the used $\lambda/4$-, $\lambda/2$-plates, grids, filters or attenuators, have different absorption and reflection spectra, what is considered by the calibration procedure. In addition, also the size of the beam in the focus of the parabolic mirror can be taken into account, if the sample size is smaller than the beam diameter, which leads to absorption losses. Therefore, a pyroelectric camera with a detection area of 12.8×12.8 mm^2 and a resolution of 0.1 mm is placed at the sample position. This camera allows to image the spatial distribution of the intensity in a wide spectral range and to calculate the mean power per area. In addition, the quality and mode structure of the THz beam as well as the focus of the used parabolic mirror can be probed by this device (for an exemplary picture see Fig. 10(b)). For temperature dependent measurements, the samples can be mounted into a direct flow optical cryostat system.

3.4   Description and details of the studied samples

This section describes the studied sample structures and fabrication processes. First, the monolayer graphene samples produced by the exfoliation technique as well as epitaxially grown on SiC, afterwards both the (001)- and (111)-oriented silicon metal-oxide-semiconductor field-effect-transistors (MOSFETs) are discussed.

3.4.1 Monolayer graphene samples

Two different sets of graphene samples were investigated, small exfoliated graphene flakes produced on a SiO_2 substrate as well as large area graphene epitaxially grown on SiC.

The small graphene samples were prepared from highly oriented pyrolytic graphite (HOPG) using the mechanical exfoliation technique [4] on an oxidized silicon wafer (also called "Scotch tape technique" or "drawing method"). By means of a cohesive tape, graphite crystals were split repeatedly into increasingly thinner pieces and, afterwards, sedimented on the wafer. The oxide thickness of 300 nm allows to locate graphene flakes in an optical microscope and to assess their thickness by the contrast ratio between the flakes and the background. The SiO_2 layer of this proper thickness results in interference effects, which enables seeing and identifying the samples, as the typical violet color of the 300 nm oxide changes slightly into blue. The reliability of this method was checked using Raman spectroscopy and low-temperature quantum Hall measurements on similar samples [83]. Typically, samples were p-doped by adsorbed contaminants with carrier concentrations $N_s \leq 2 \times 10^{12}$ cm^{-2}. The Fermi energies were $\varepsilon_F \leq 165$ meV and the mobilities μ at room temperature of the order of 2.5×10^3 cm^2/Vs. The flakes investigated in this work were all single layer with a typical size of some tens of μm. After recording the position of the flakes with respect to predefined markers on the Si wafer, they were contacted by electron beam lithography and thermal evaporation of 60 nm thick Pd electrodes. The resistance of graphene measured between var-
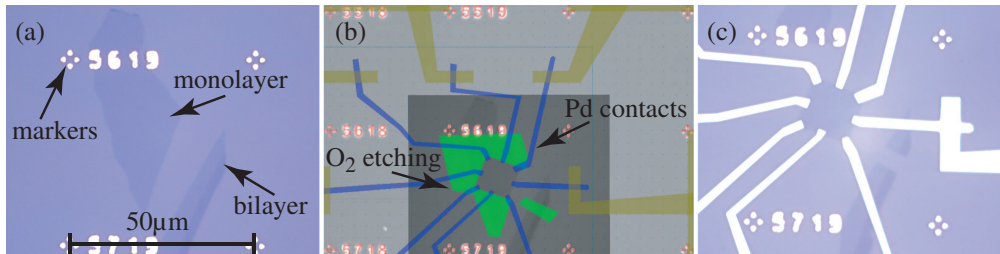

Figure 15: Preparation process of a graphene flake. (a) Sample obtained from exfoliation technique. (b) Etching and lithography steps. (c) Finished sample with contact geometry.
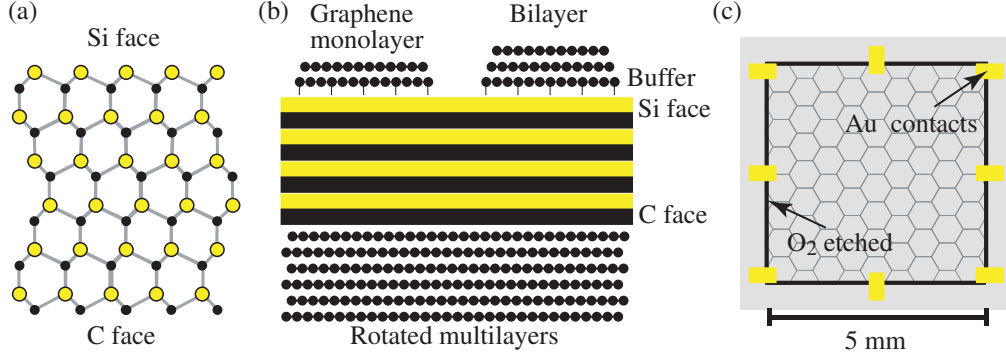
Figure 16: Preparation process of a graphene sample on a SiC substrate. (a) Hexagonal 4H-SiC with wurtzite structure in a side view. (b) Graphene mono- and bilayer formation on the Si-terminated face of the substrate, separated by a buffer layer. (c) Schematical sketch of a finished sample with contact geometry.

ious contacts was in the range of 1 kΩ. Some flakes were cut into shape using oxygen based reactive ion etching. Figure 15 shows the shapes and the contact geometry of one investigated sample. The samples were glued onto holders with conductive epoxy. Their morphology was characterized by atomic force microscopy measurements under ambient conditions with the microscope in intermittent contact mode with standard silicon tips [15, 84].

The second set consisting of large-area graphene samples has been grown on the Si-terminated face of a 4H-SiC(0001) (see Fig. 16(a)) semi-isolating substrate having a band gap of 3 eV [85, 86]. At temperatures larger than 1150 °C, the SiC crystal starts to decompose. Silicon vaporizes due to its higher vapor pressure, whereas the nascent carbon builds stable C-C bindings and stays at the surface forming graphene or graphite [87, 88]. The reaction kinetics on the Si-face is slower than on the C-face because of the higher surface energy, which supports a homogeneous and well controlled graphene formation, separated from the substrate by a buffer layer [89], see Fig. 16(b). The buffer layer occurs only on the Si face of the substrate and has a fully developed σ band building a honeycomb lattice similar to a real graphene layer. But covalent bindings to the substrate prevent the formation of a π band and, thus, the emergence of states near the Fermi energy. This buffer layer is thereby electrically isolating.

Here, graphene was grown at a temperature of 2000 °C in argon atmosphere at 1 atm gas pressure resulting in monolayers of graphene atomically uniform over more than 1000 μm^2, what was checked by low-energy electron microscopy [90]. The presence of Ar decelerates the sublimation of Si and increases the building temperature of graphene up to 1650 °C in contrast to the growth in ultra high vacuum. This enhances the mobility of the surface atoms yielding smooth and homogeneous terraces. This method allowed the growth of samples with a size of 5×5 mm^2. The boundaries of this area were etched by oxygen plasma with a width of 20 μm to obtain macroscopically well-defined graphene edges, see the black square in Fig. 16(c). Eight contact pads were produced by the deposition of 3 nm of Ti and 100 nm of Au. The measured resistance was in the range of 10 to 20 kΩ. Low-field measurements show that the manufactured material is n-doped due to the charge transfer from SiC [89,91], with a measured electron concentration N_s in the range of (3 to 7)$\times 10^{12}$ cm^{-2} and a mobility μ of about 1.0×10^3 cm^2/Vs at room temperature. One of these samples with a smaller size of 3×3 mm^2 shows p-type conductivity. It has a density and mobility similar to that of the n-type samples [14].

3.4.2 Silicon-MOSFET structures

Another kind of samples is provided by Si-MOSFETs fabricated by means of ordinary MOS technology. In this work, a number of two-dimensional Si structures are investigated differing in their crystallographic orientation. The samples are prepared on precisely (001)- and (111)-oriented as well as on miscut silicon surfaces, for an illustration of all four sets of MOSFETs see Fig. 17.

On the precisely (001)-oriented surface (set 1), a transistor along $y \parallel$ [110] with a channel length of 3 mm and a width of 2.8 mm was prepared with a 110 nm thick SiO$_2$ layer, a semitransparent polycrystalline Si gate and a doping level N_a of the depletion layer of about 3×10^{15} cm^{-3}. In this transistor, a variation of the gate voltage V_g from 1 to 20 V changes the carrier density N_s from about 1.9×10^{11} to 3.8×10^{12} cm^{-2} and the energy spacing ε_{21} between the size-quantized subbands $e1$ and $e2$ from 10 to 35 meV. The peak mobilities μ at room and helium temperature are 700 and 10^4 cm^2/Vs, respectively.
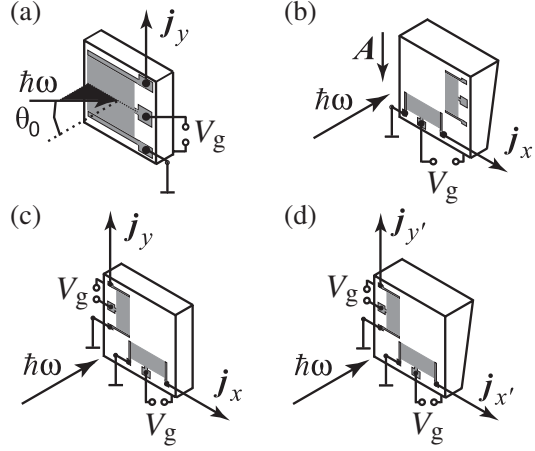
Figure 17: Sketches of the used Si-MOSFETs. (a) Set 1: (001)-oriented Si structure containing only one current direction j_y under oblique illumination $\theta_0 \neq 0°$. (b) Set 2: miscut (001)-Si-MOSFET excited by normally incident radiation with the transistor in x' direction. (c) Set 3: exactly (111)-oriented Si-MOS structure enabling the current detection in both directions x and y. (d) Set 4: (111) Si structure with the surface tilted from the (111)-plane about $\delta\Theta = 4°$.

A second set of MOSFETs was fabricated on miscut surfaces tilted by an angle of $\delta\Theta = 9.7°$ or $10.7°$ from the (001)-plane around $x' \parallel [1\bar{1}0]$. Two transistors were prepared on each miscut substrate, one oriented along x' and the other along the inclination direction $\boldsymbol{A} \parallel y'$. They have a size of 1.2×0.4 mm^2, semitransparent Ti gates of 10 nm thickness and a doping concentration N_a of about 1×10^{13} cm^{-3}. A variation in the gate voltage from 1 to 20 V changes the carrier density N_s from 1.5×10^{11} to 3.0×10^{12} cm^{-2} and the energy spacing ε_{21} from 5 to 28 meV. The peak electron mobilities μ in the channel are about 10^3 and 2×10^4 cm^2/Vs at $T = 296$ and 4.2 K, respectively. The MOSFETs produced on miscut surfaces have a 140 nm thick SiO$_2$ layer [23].

Furthermore, MOSFETs fabricated on exact and miscut (111) silicon surfaces have been studied. These samples were produced by means of standard MOS technology including high temperature oxidation of silicon to get SiO$_2$ as 100 nm thick insulator, ion-implantation to fabricate heavily doped n^{++} contact regions and the fabrication of heavily doped semitransparent poly-

crystalline gates. The Si samples with their surfaces precisely oriented along the (111) plane (set 3) contain two transistors, each prepared with a channel length of 1.5 mm, a width of 0.5 mm and the channel directions parallel either to $x \parallel [\bar{1}10]$ or $y \parallel [\bar{1}\bar{1}2]$. The variation of the gate voltage V_g from 1 to 20 V changes the carrier density N_s from 2.0×10^{11} to 4.1×10^{12} cm^{-2}. The (111)-oriented Si structure are characterized by a six-fold valley degeneracy, see Chap. 2.4, which has been previously approved in experiments on the phonon drag effect [92]. Note that the energy of valley splitting, if any, in nominally unstrained Si-MOSFETs is much smaller than the mean kinetic energy of carriers at room temperature and, therefore, is negligible [93].

The fourth set of MOSFETs is fabricated on Si surfaces with the normal $\boldsymbol{n}$ rotated from the (111) orientation around the axis $x' = x \parallel [\bar{1}10]$ by an angle of $\delta\Theta = 4°$. Two transistors with the same size are prepared on the miscut substrate with the channels oriented either along x' or along the inclination axis $y' \perp \boldsymbol{n}, x'$. They have 70 nm thick SiO$_2$ layers and semitransparent polycrystalline Si gates. Variation in V_g from 1 to 20 V changes N_s from 3.0×10^{11} to 5.7×10^{12} cm^{-2}.

All kinds of (111)-oriented MOSFETs used in the experiment exhibit room-temperature electron mobilities μ in the channel between 400 and 800 cm^2/Vs. The orientation of the Si surfaces has been proved applying an X-ray diffractometer. The accuracy of the orientation is better than 0.5° [17].

4 Photocurrents in graphene

First of all, the experimental observation of photocurrents in monolayer graphene is reported. It is demonstrated that the illumination of graphene with THz radiation in the absence of any dc field applied to the sample causes directed electric currents, including those solely driven by the radiation's helicity. The experiments evidence that the photocurrents in graphene consist of two contributions. The first one appears only at oblique incidence and is an odd function of the angle of incidence θ_0, whereas the second contribution reaches its maximum at normal incidence and is even in θ_0. The former effect discussed in the following section is caused by the circular photon drag effect [36–38,94], which stems from the simultaneous transfer of both the linear and angular momenta of photons to the carriers in the interior of the graphene sheet. After presenting the experimental results, the novel model of the circular ac Hall effect is developed. Additional experiments on small area graphene flakes reveal a remarkable contribution to the current formation induced by normally incident light, that, however, cannot be attributed to any photoelectric effect in an ideal honeycomb lattice of graphene. These currents are caused by the edges of the real finite-size samples. Subsequently, this current origin is approved by further experiments on large area graphene samples.

4.1 High frequency Hall effect in large area graphene

For more than a century, the Hall effect has enabled physicists to gain information on the electronic properties of matter. In Hall's original experiment [95], a suitable combination of static magnetic and electric fields allowed to determine the sign and density of charge carriers, opening the door to a more thorough understanding of electronic transport in metals and semiconductors. The high frequency or circular ac Hall effect (CacHE), in contrast, driven by the crossed alternating electric and magnetic fields of circularly polarized light, delivers information about the underlying electron dynamics. This effect described in the following remained so far undiscovered, as electromagnetic radiation incident upon low dimensional structures causes all sorts of photocurrents stemming from both contact and band-structure specifics. With respect to the latter,

graphene being just recently feasible by experiments [4] is an ideal model system, as symmetry prevents other helicity driven photocurrents like the circular photogalvanic [45] or spin-galvanic effect [20] to occur. These effects require the lack of spatial inversion and are, therefore, forbidden in the honeycomb crystal lattice of graphene, which belongs to the point-group D_{6h} having a relatively high symmetry. A more detailed symmetry analysis taking into account a possible symmetry breaking by the substrate of graphene samples can be found at the end of this chapter (see also Ref. [15]).

4.1.1   Experimental observation of photocurrents in graphene

First, the results obtained at large area graphene epitaxially grown on SiC substrates (see Chap. 3.4 for sample details) by illuminating the interior of the samples are discussed. The experimental geometry is sketched in Fig. 18. The graphene samples are illuminated at oblique incidence, where the incidence angle θ_0 was varied between $-40°$ and $+40°$. The resulting photocurrent is measured at room temperature for wavelengths between 90 μm and 280 μm using either the continuous-wave CH_3OH laser or the high power pulsed laser with NH_3 as active gas, see Chap. 3.1. For these wavelengths the condition $\omega\tau < 1$ holds, with ω being the angular frequency of the light and τ the momentum relaxation time of electrons (or holes) in graphene. The resulting photocurrent is measured by the voltage drop across a load resistor between pairs of contacts made at the edges of the graphene square. The degree of circular polarization, $P_{\mathrm{circ}} = \sin 2\varphi$, is adjusted by a quarter-wave plate, where
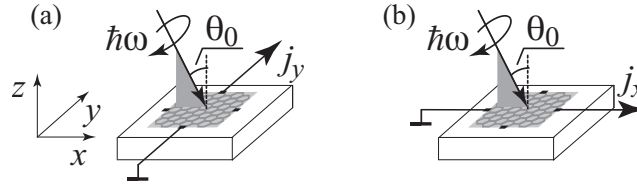
Figure 18: Experimental configurations showing the radiation's plane of incidence and the contact arrangement at the edges of graphene. Both (a) transverse and (b) longitudinal geometries are used to measure the photocurrents.
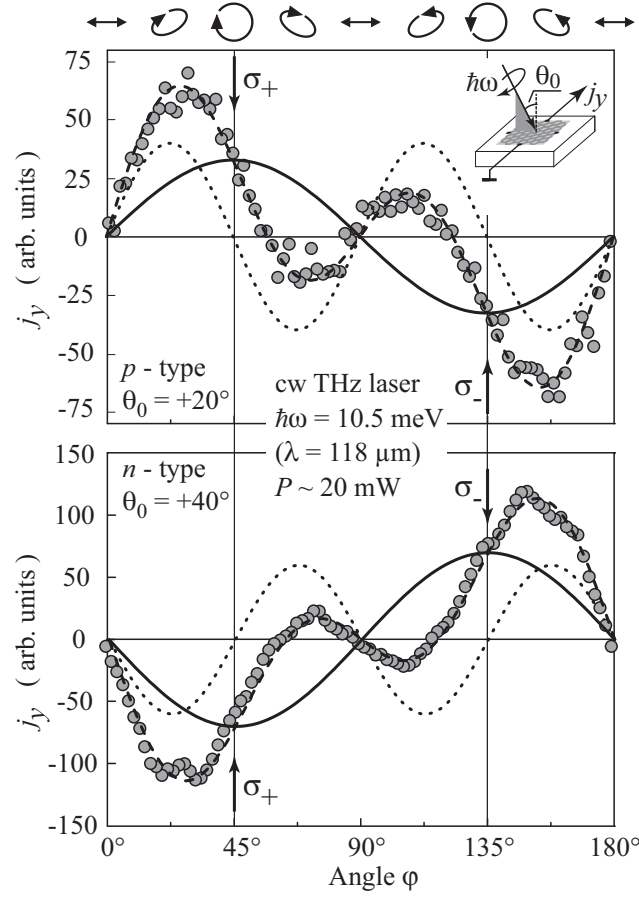
Figure 19: Transverse photocurrent j_y as function of the angle φ for p- and n-type epitaxial graphene. The ellipses on top illustrate the polarization states for various φ. Dashed lines show fits to the calculated total current $j_A + j_B$ comprising the circular contribution j_A (CacHE, full line) and the linear contribution j_B (dotted line). An offset ξ, two times smaller than j_A, is subtracted.

φ is the angle between the initial polarization vector of the laser light and the plate's c-axis, see Chap. 3.2.

The photocurrent for the transversal geometry, j_y, is shown in Fig. 19 as a function of the angle φ for p- and n-type graphene. The results of this plot are obtained by the cw THz laser with a wavelength of $\lambda = 118$ µm (or the corresponding photon energy $\hbar\omega = 10.5$ meV), a power of $P \approx 20$ mW and a diameter of the laser spot of about 1 mm. This low power radiation
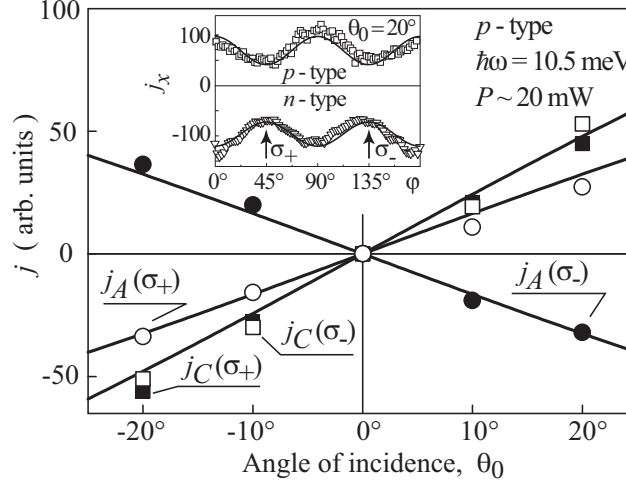
Figure 20: Photocurrents j_A (circles) and j_C (squares) induced by circularly polarized light $\sigma_\pm$ in the p-type epitaxial sample as function of the incidence angle θ_0. Open symbols correspond to σ_+, filled symbols to σ_- light. The solid lines are fits based on Eqs. (40) and (41). The inset shows the φ dependence of the longitudinal current j_x measured in p- and n-type graphene together with fits according to Eq. (38). The constant offsets ξ and ξ' are subtracted.

is modulated at chopper frequencies in the range from 120 to 600 Hz. The photoresponse ($j \propto U$) to the cw laser is measured by the voltage drop U across a 10 MΩ load resistor and recorded with lock-in technique. The sign of the signal is defined as a relative phase with respect to the lock-in reference signal frequency, which was kept the same for all measurements.

However, the principal observation made in all investigated samples for both low and high power excitation is that for purely circularly polarized light, i.e. for $\varphi = 45°$ and $135°$, the sign of j_y depends on the light's helicity and the charge carriers' polarity (positive for holes and negative for electrons). The overall dependence of the transversal photocurrent j_y on the angle φ is more complex and, at small θ_0, well described by

$$j_y \;=\; A\,\theta_0\,\sin 2\varphi \;+\; B\,\theta_0\,(1/2)\sin 4\varphi \;+\; \xi\,. \tag{37}$$

Here, ξ is a polarization independent offset, ascribed to sample or intensity inhomogeneities. It does not change with the angle of incidence θ_0 and is
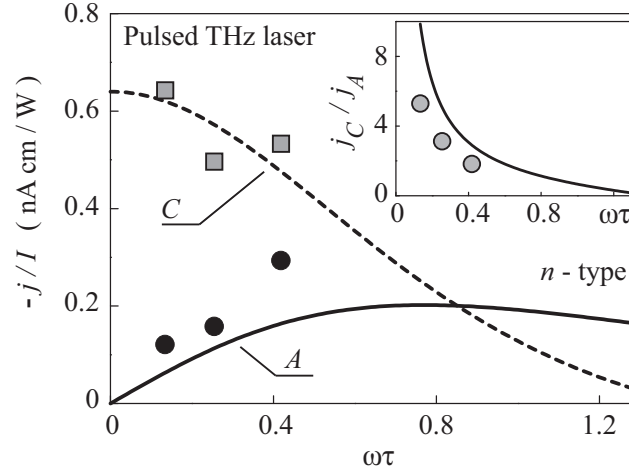
Figure 21: Frequency dependence of $A = j_A/\theta_0$ (dots) and $C = j_C/\theta_0$ (squares) as function of $\omega\tau$ for circularly polarized light. The photocurrent j_A is obtained from the current in y direction, where $j_A = A\theta_0 \sin 2\varphi$, and j_C from the current induced in x direction, which for σ_+, σ_- reads $j_x = C\theta_0$. The calculated frequency dependence of j_A (Eq. (40), solid line) and j_C (Eq. (41), dashed line) describe the experiment quantitatively well. The inset shows j_C/j_A for experiment (circles) and theory (line).

subtracted from the data of Fig. 19. The fit parameters A and B describe the strength of the circular contribution $j_A \propto \theta_0 \sin 2\varphi$ and of the contribution $j_B \propto \theta_0(1/2) \sin 4\varphi$ caused by linear polarization. Both functions being in agreement with the Stokes parameters already introduced in Chap. 3.2 are shown together with the resulting fit of the data in Fig. 19. Note that for purely circularly polarized light, the linear contribution j_B vanishes.

In the longitudinal geometry, being schematically illustrated in Fig. 18(b), only linearly polarized light gives rise to the φ-dependence of the current j_x:

$$j_x \;=\; B\,\theta_0\,(1/2)\,(1 + \cos 4\varphi) \;+\; C\,\theta_0 \;+\; \xi'. \tag{38}$$

This is shown in the inset of Fig. 20 for both n- and p-type graphene. A sizable fraction of j_x stems from the polarization independent contribution $j_C = C\theta_0$, proportional to the angle of incidence θ_0, whose sign does not reverse with the helicity. Both currents j_y and j_x, however, change their signs upon reversing

the direction of incidence; the corresponding dependence on θ_0 is presented in Fig. 20. Here, the photoresponses of the p-type graphene sample to right- (σ_+) and left-handed (σ_-) light are shown for both experimental geometries. All data of Fig. 20 are obtained by the cw THz laser with the same parameters as mentioned above [14].

In contrast, the results presented in Fig. 21 stem from the excitation of the n-type graphene sample by the high power pulsed THz laser. The experimental data are obtained for both geometries and for the wavelengths 90, 148 and 280 μm with the power ranging from 10 to 30 kW. For the pulsed laser, the current density j normalized to the laser intensity I (power per area) can be extracted from the data due to the well known power calibration (see Chap. 3.3 for more details). This delivers the frequency dependence shown in Fig. 21 for both the helicity dependent magnitude A of the photocurrent j_A in y direction and the polarization independent value C of j_C in the longitudinal geometry. The inset shows the ratio j_C/j_A, independent of the absolute values, which demonstrates that the helicity driven current j_A vanishes for $\omega\tau \ll 1$ [14].

4.1.2   Model of the circular ac Hall effect

Photon helicity driven currents are well known in low-dimensional semiconductor structures, whereby the photocurrent generation has been proven to be a very efficient method to study non-equilibrium processes in semiconductors yielding information on their symmetry, details of the band structure and processes of electron momentum, spin and energy relaxation, etc. [18, 28, 29, 45]. Microscopic mechanisms of this class of phenomena in quantum wells are usually based on the spin-orbit coupling in gyrotropic materials [18–20], see also, e.g., Chap. 2.2.3 for illustration of such an effect. However, the light carbon atoms in graphene enable only a vanishingly weak spin-orbit interaction, whereby a spin dependent origin of the photocurrent generation becomes ineffective. In graphene, in contrast, rather the orbital motion of charge carriers caused by the electromagnetic radiation leads to the observed helicity driven currents. Thereby, it is convenient to discuss these currents by means of the high frequency conductivity, see Chap. 2.1 for the basic idea, taking into account the light's magnetic field component and the peculiarities of graphene.
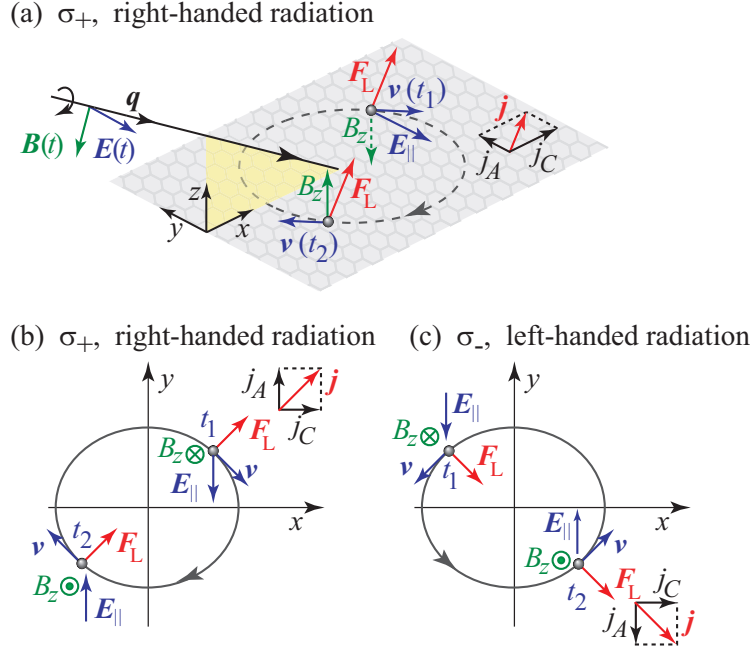
Figure 22: Schematic illustration of the circular ac Hall effect. For simplicity positive carriers, i.e. holes, are assumed. (a) Electric and magnetic field vectors of σ_+ polarized light with wavevector $\boldsymbol{q}$ under oblique incidence in the (xz) plane. The dashed orbit represents the hole's elliptical trajectory caused by the ac $\boldsymbol{E}$-field. The relevant vectors are shown for two instants in time, t_1 and t_2, shifted by half a period. The hole velocities $\boldsymbol{v}_1$ and $\boldsymbol{v}_2$ are given for the points in time t_1 and t_2, respectively, taking retardation into account. The direction of the Lorentz force $\boldsymbol{F}_\mathrm{L}$ due to the ac $\boldsymbol{B}$-field determines the direction of the Hall current $\boldsymbol{j}$. (b) Top view of (a). (c) Same as (b) but for σ_- light.

The experimental data are well described by the theoretical model, outlined in the following. While the longitudinal currents can be explained analogous, here, the transverse helicity driven current j_A is the focus of the discussion. The basic physics behind the CacHE is illustrated in Fig. 22. This model considers the classical regime, where the photon energy is much smaller than the Fermi energy, $\hbar\omega \ll |\varepsilon_\mathrm{F}|$, fulfilled in the experiment as $|\varepsilon_\mathrm{F}|$ is larger than 100 meV while the photon energy $\hbar\omega$ is typically $\sim$ 10 meV. In this range, the THz radiation causes intraband transitions only. For circularly polarized radiation, the electric field rotates around the wavevector $\boldsymbol{q}$, as sketched in

Fig. 22(a) for σ_+ circularly polarized light. This leads to an orbital motion of the holes (electrons) within the graphene layer. The CacHE comes into existence due to the combined action of the rotating electric and magnetic field vectors $\boldsymbol{E}$ and $\boldsymbol{B}$, respectively. At an instant of time, e.g., at t_1, the electron is accelerated by the in-plane component $\boldsymbol{E}_\parallel$ of the ac electric field. At the same time, the electron with velocity $\boldsymbol{v}$ is subjected to the out-of-plane magnetic field component $\boldsymbol{B}_z$ perpendicular to the graphene sheet. Note that the velocity $\boldsymbol{v}$ does not instantaneously follow the actual $\boldsymbol{E}_\parallel$-field direction due to retardation: There is a phase shift equal to $\arctan(\omega\tau)$ between the electric field and the electron velocity. Only for $\omega\tau \ll 1$ the directions of the electron velocity $\boldsymbol{v}$ and the electric field component $\boldsymbol{E}_\parallel$ coincide. The effect of retardation, well known in the Drude-Lorentz theory of high frequency conductivity [26], was already discussed in Chap. 2.1 and results in an angle between the velocity $\boldsymbol{v}$ of the carrier and the electric field direction $\boldsymbol{E}_\parallel$, which depends on the value of $\omega\tau$. The resulting Lorentz force $\boldsymbol{F}_\mathrm{L} = e(\boldsymbol{v} \times \boldsymbol{B}_z)$, where e is the positive (holes) or negative (electrons) carrier charge, generates a Hall current $\boldsymbol{j}$, also shown in Fig. 22. Half a period later at $t_2 = t_1 + T/2$, where the $\boldsymbol{E}$- and $\boldsymbol{B}$-fields of the electro-magnetic wave are rotated about 180°, both the electron velocity and the out-of-plane magnetic field component get reversed. Therefore, the direction of the Lorentz force $\boldsymbol{F}_\mathrm{L}$ and, consequently, the current $\boldsymbol{j}$ stay the same. The oscillating magnitude and direction of $\boldsymbol{B}_z$ along the closed trajectory leads to a periodical modulation of the Lorentz force with non-zero average causing a non-zero time-averaged Hall current with fixed direction.

If, as shown in Fig. 22(c), the light helicity is reversed, the electric field rotates in the opposite direction and, thus, the charge carrier reverses its direction. Hence, the retardation leads to an inversion of the y-component of the Lorentz force $\boldsymbol{F}_\mathrm{L}$ at the times t_1 and t_2. Consequently, the polarity of the transverse, time-averaged Hall current j_A changes. This is the circular ac Hall effect. On the other hand, the longitudinal current j_x does not change the direction when the helicity flips. This current is also observed in the experiment and displayed in Fig. 20. Obviously, reversing the angle of incidence, $\theta_0 \to -\theta_0$, results in a change of the relative sign of $\boldsymbol{E}_\parallel$ and $\boldsymbol{B}_z$ so that both the longitudinal and transversal currents j_x and j_y flip their directions.

While the explanation of the CacHE has been given in a pictorial way above, now a microscopic description based on the Boltzmann kinetic equation for the electron distribution function $f(\boldsymbol{p}, \boldsymbol{r}, t)$ is resorted, with the free-carrier momentum $\boldsymbol{p}$, in-plane coordinate $\boldsymbol{r}$, and time t:

$$\frac{\partial f}{\partial t} \;+\; \boldsymbol{v}\,\frac{\partial f}{\partial \boldsymbol{r}} \;+\; e\,(\boldsymbol{E} + \boldsymbol{v} \times \boldsymbol{B})\,\frac{\partial f}{\partial \boldsymbol{p}} \;=\; Q\{f\}\,. \tag{39}$$

Here, $Q\{f\}$ is the collision integral described in terms of momentum relaxation times τ_n ($n = 1, 2 \ldots$) for corresponding angular harmonics of the distribution function [15,96]. The electric current density is given by the standard equation $\boldsymbol{j} = 4e \sum_{\boldsymbol{p}} \boldsymbol{v}\, f(\boldsymbol{p})$, where a factor of 4 accounts for spin and valley degeneracies. In order to solve the kinetic equation (39), the solution is expanded in powers of electric and magnetic fields, keeping linear and quadratic terms only. This is described in more detail in Ref. [15] closely following previous work [96]. In the calculation of $f(\boldsymbol{p})$ and $\boldsymbol{j}$, the energy dispersion $\varepsilon_p = \pm vp$ of free carriers in graphene and the relation $\boldsymbol{v} \equiv \boldsymbol{v_p} = v\boldsymbol{p}/|\boldsymbol{p}|$ between the velocity and the quasi-momentum is used. Contributions to the photocurrent appear not only from a combined action of the electric and magnetic fields of the light wave (so called EB-mechanism), as illustrated in Fig. 22 by means of the CacHE model, but also due to the spatial gradient of the electric field (qE^2-mechanism) [15,96]. As final result one obtains for the helicity driven current

$$j_A \;=\; A\,\theta_0\,\sin 2\varphi \;=\; q\,\theta_0\,\chi P_{\text{circ}}\left(1 + \frac{\tau_2}{\tau_1}\right)\frac{1 - r}{1 + \omega^2\tau_2^2}\,, \tag{40}$$

flowing in y-direction, and the φ-independent current

$$j_C \;=\; C\,\theta_0 \;=\; \frac{q\theta_0\chi}{\omega\tau_1}\left[2(1 + r) + (1 - r)\frac{1 - \omega^2\tau_1\tau_2}{1 + \omega^2\tau_2^2}\right]\,, \tag{41}$$

flowing along x (for light propagating in the (xz) plane). Here $q = \omega/c$, $q\sin\theta_0 \approx q\theta_0$, $r = d\ln\tau_1/d\ln\varepsilon$ and $\chi = e^3\tau_1(v\tau_1 E)^2/[2\pi\hbar^2(1 + \omega^2\tau_1^2)]$.

The results of the calculation are shown in Figs. 20 and 21. The used fit parameters only depend on details of the underlying scattering mechanism discussed below. Equation (39) provides in addition to j_A and j_C also expressions for currents $j_{B,x} \propto q\theta_0(1/2)(1 + \cos 4\varphi)$ and $j_{B,y} \propto q\theta_0(1/2)\sin 4\varphi$, for details see [15]. The latter currents are independent of the sign of the helicity

and readily excited by linearly polarized light [15]. For elliptically polarized
radiation, this causes a more complex dependence of the photocurrent on the
angle φ (see lines in Fig. 19 and in the inset of Fig. 20). These currents with
different angular dependencies are superimposed on the circular ac Hall effect
(and also on j_C discussed above), when the angle φ is varied. However, for
circularly polarized light ($\varphi = 45°$ or $135°$), the degree of linear polarization
is zero and the corresponding currents vanish leaving the undisturbed CacHE
contribution.

As seen in experiment the polarity of the photocurrents is opposite for n- and
p-type graphene samples. This is expected from theory since (i) the ac Hall
current j_y as well as the longitudinal current j_x are proportional to e^3 and
(ii) the conduction- and valence-band, in the massless Dirac model, are sym-
metric with respect to the Dirac point. In contrast, in typical semiconductors
conduction- and valence-band states have different symmetry properties and,
thus, the relation between values and polarities of the ac Hall photocurrents is
more involved.

Equations (40) and (41) suggest a non-monotonous frequency dependence of
the photocurrents. In Fig. 21 the calculated frequency dependence of both
$A = j_A/\theta_0$ and $C = j_C/\theta_0$ are compared quantitatively to the experimen-
tal data. For the momentum scattering time, the relation $\tau_1 = 2\tau_2 \propto \varepsilon_p^{-1}$,
valid for short range scattering [3] and relevant for the low mobility samples
($\tau_1 \approx 2 \times 10^{-14}$ s), is used. Apart from the above assumption of short range
scattering, no further fit parameter is needed. Figure 21 shows that the theory
describes the frequency dependence and the absolute value of the photocur-
rent very well. Both j_A and j_C contribute to the photocurrent for circularly
polarized light. It is remarkable that the helicity driven current j_A and the
polarization independent photocurrent j_C show completely different frequency
dependencies. While j_C does not change much for $\omega\tau \ll 1$, the helicity driven
current j_A increases with growing $\omega\tau$ at low frequencies. For large $\omega\tau$ well
above unity both photocurrents decrease with increasing ω. This property
agrees with the model addressed above (see Fig. 22). The CacHE, i.e. j_A, dis-
appears for $\omega \to 0$, since no circular polarization exists for static fields and the
required retardation vanishes. With increasing ω the retardation becomes im-

portant and the current increases $\propto \omega\tau$. For $\omega\tau \simeq 1$ the current gets maximal and decreases rapidly at higher ω, $j_y \propto 1/\omega^3$. In contrast, the longitudinal current j_C does not depend on the frequency at $\omega\tau \ll 1$ and displays its maximum at $\omega \to 0$. The effect of retardation is just opposite to that on j_A: Increasing ω reduces the y-component of the velocity (Fig. 22) and hence the x-component of the Lorentz force. As a consequence, j_C drops with increasing ω, see Fig. 21. The ratio of j_C and j_A is plotted in the inset of Fig. 21 showing that the role of the circular effect substantially increases with $\omega\tau$. The excellent agreement of theory and experiment evidences that the model covers the essential physics of the circular ac Hall effect.

The photocurrents j_C and j_A are both proportional to the wavevector q and may, therefore, also be classified as photon drag effect, see Chap. 2.2.2 for a qualitative description. In fact, the polarization independent longitudinal current j_C is the well-known linear photon drag effect, which was first treated by Barlow [33] in 1954, observed in bulk cubic semiconductors [34,35] and recently discussed for graphene [15,97]. The effect, described here, can be considered as the classical limit ($\hbar\omega \ll \varepsilon_{\mathrm{F}}$ and $\omega\tau \lesssim 1$) of the circular photon drag effect. As it can be described in terms of the Lorentz force (see Eq. (39)), it is called ac Hall effect. The circular photon drag effect, which takes over at higher frequencies, i.e. for $\omega\tau \gg 1$, was discussed phenomenologically [36,37] and observed in GaAs quantum wells in the mid-infrared range [38]. In this pure quantum mechanical limit, the picture above is inapplicable and involves asymmetric optical transitions and relaxation in a spin polarized non-equilibrium electron gas. The drag effect in metallic photonic crystals, generating a transverse current due to microscopic voids, was reported recently [94].

The appearance of a helicity driven Hall current as a combined action of the light in-plane wavevector and the induced orbital momentum is a specific feature of two-dimensional, even centrosymmetric, structures like graphene. CacHE is a general phenomenon and should exist in any low-dimensional system. It is, however, more readily observable in a monoatomic layer like graphene, as in multilayered low-dimensional systems, e.g., quantum wells, the CacHE is masked by the circular photogalvanic effect [45], see Chap. 2.2.3. In isolated graphene, the spatial inversion symmetry forbids photogalvanic ef-

fects. In real samples deposited on a substrate, the equivalence of z and $-z$ directions is broken. Since the circular photogalvanic effect in the resulting point-group symmetry C_{6v} requires an electronic response to the out-of-plane component of the electric field, it is governed, in monoatomic layers, by a small factor $\hbar\omega/\Delta$, where $\Delta \sim 10$ eV [3] is the energy distance to other bands, and strongly suppressed in comparison to zinc-blende-lattice quantum wells [14,15].

4.2   Helicity driven currents in exfoliated graphene

Additionally, photocurrents are also studied in small area graphene samples prepared on SiO_2 substrates by the exfoliation technique. The main difference to the experiments carried out on epitaxial samples is the small size of only some tens of micrometers. As a result, not only the interior of graphene, but also the sample edges are illuminated by the THz laser beam having a typical diameter of some millimeters. Therefore, a novel type of photocurrents attributed to the edges of graphene is observed in the experiment.

4.2.1   Experiments on small area exfoliated graphene

Irradiating small area exfoliated graphene (see Chap. 3.4 for sample details) at normal as well as oblique incidence induces photocurrents in all investigated samples. The signal is detected at room temperature for both low and high power excitation of the cw and the pulsed laser, respectively. In the latter case the duration of the photocurrent pulses is about 100 ns, which corresponds to the THz laser pulse length. In order to prove that the signal stems from graphene and not, e.g., from the substrate, the graphene layer was removed from one of the small area samples, whereby the signal disappeared. In the following, photocurrents observed by employing the cw THz laser with a photon energy of 10.5 meV, power of about 20 mW and a diameter of the laser spot in the focus of about 1 mm are presented exemplary.

Figure 23 shows the photoresponse $U_\perp$, which is proportional to the photocurrent j, of the two samples 1 and 2 as a function of the angle φ. The signals are measured for different angles of incidence $\theta_0 = 0, \pm 25°$. While the figure shows
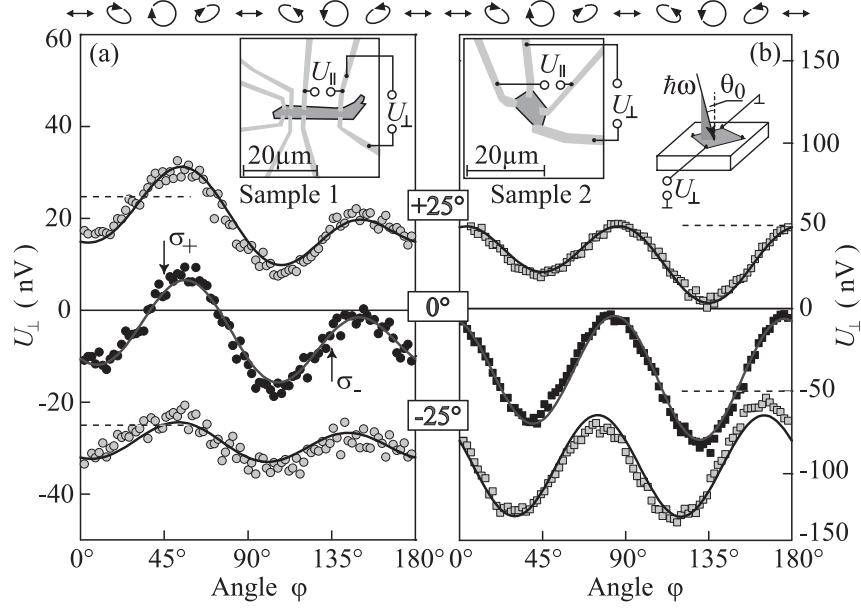
Figure 23: Photosignals, $U_\perp$, in two graphene sheets as a function of the angle φ for various angles of incidence, θ_0. The signal is measured nearly perpendicular to the light propagation direction. The data for $\theta_0 = \pm 25°$ are shifted by ± 25 nV (sample 1, panel (a)) and ± 50 nV (sample 2, panel (b)), respectively. The horizontal dashed lines show the x axes corresponding to $U_\perp = 0$ for the shifted data. Full lines are fits to Eq. (42). The insets show the sample geometry and experimental configuration. The ellipses on top illustrate the polarization states for various angles φ.

the photoresponse obtained from the pairs of contacts oriented almost perpendicularly to the light propagation direction, a photocurrent was also observed at any other pair of contacts. Generally, the dependence of the photocurrent can be well fitted by

$$J(\varphi) \;=\; A\sin 2\varphi \;+\; B(1/2)\sin 4\varphi \;+\; B'(1/2)(1+\cos 4\varphi) \;+\; C\,, \quad (42)$$

where A, B, B' and C are fitting parameters. Note that all these functions are in agreement with the Stokes parameters $s_0, ... s_3$ already introduced in Chap. 3.2. Such behavior, phenomenologically well described by symmetry arguments (see below), was found in all graphene samples. The fits to the experimental data shown by solid lines in Fig. 23 demonstrate a good agree-
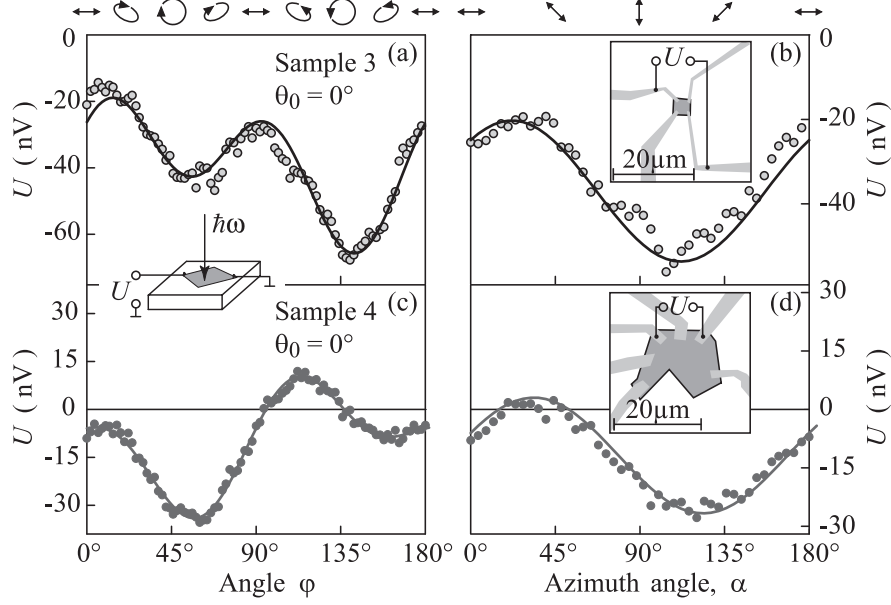
Figure 24: Polarization dependences of the photoresponse obtained at normal incidence for the samples 3 and 4. The two left panels show signals as a function of the radiation helicity, given by φ, and the two right panels as a function of the electric field orientation given by the azimuth angle α. Full lines are fits corresponding to Eq. (42) (panels (a) and (c)) and Eq. (43) (panels (b) and (d)). The insets show the experimental arrangement and the samples' geometry. The symbols on top of the left and right panels illustrate the polarization states for various angles φ and α, respectively.

ment. The first term on the right hand-side of Eq. (42), which is proportional to $\sin 2\varphi$ and described by the parameter A, changes its sign upon reversing the photon helicity (marked by arrows). The analysis of the experimental data gives a clear evidence for a substantial contribution to the total photocurrent that changes its sign upon switching the radiation's helicity from right- (σ_+) to left-handed (σ_-) circularly polarized. This is most evidently seen in the data obtained for sample 1, where the current's inversion point is directly detected at normal incidence, $\theta_0 = 0°$ (Fig. 23(a)). The helicity driven photocurrent gives also a substantial contribution to the photoresponse of two other samples as demonstrated in Figs. 24(a) and (c) for normal incidence of radiation.

A deeper insight into the photon helicity driven currents is again given by their dependences on the angle of incidence θ_0, as presented in Fig. 25 for the samples 1 and 2. The photoresponse of the helicity driven current $U_{\text{CPC}} \propto A$ is substantially different for the geometries, where the photocurrent is measured either in the direction transversal or almost longitudinal to the light propagation. In spite of taking care in aligning the radiation propagation direction closely parallel to the line connecting the contacts, slight deviations are possible since the invisible radiation and the small sample size prevent a full control of the adjustment. However, while the photocurrent measured in the longitudinal geometry is almost independent of the angle of incidence and reflects the signals obtained at normal incidence, the transverse current shows a superposition of two contributions being even and odd in θ_0. An important feature of the odd contribution is that its direction is determined by the light's propagation plane, the radiation's helicity and the sign of θ_0. Further, it is independent of the orientation of the sample edges. In contrast, the geometry
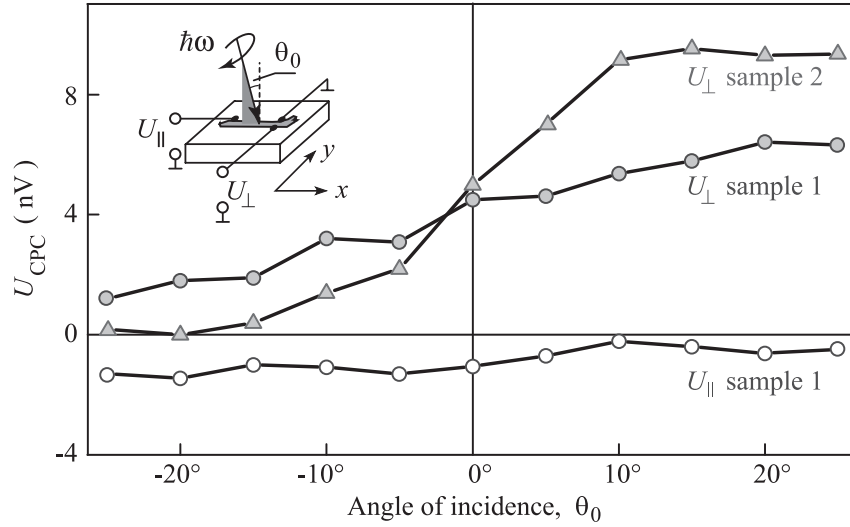
Figure 25: Signals due to circularly polarized radiation $U_{\text{CPC}} = [U(\varphi = 45°) - U(\varphi = 135°)]/2$ measured as a function of the incidence angle θ_0. Triangles and full circles show the transversal response, $U_\perp$, for samples 1 and 2, respectively. Open circles represent the signal obtained in the longitudinal geometry, $U_\parallel$, for sample 1. The inset illustrates the experimental configuration.

of the graphene flakes' edges strongly influence the photocurrents being even functions of the angle θ_0.

Now, the photocurrent contributions proportional to the coefficients B and B' in Eq. (42) are discussed. These currents, in fact, do not require the radiation's helicity and reflect the linearly polarized components of the incident radiation, described by the Stokes parameters s_1 and s_2. This has been checked in an independent experiment. By rotating a $\lambda/2$ plate the relative position between the plane of the radiation's polarization and the axes of the samples characterized by the azimuth angle α is varied. The resulting data are shown in Fig. 24(b) and (d) and are well described in agreement with Eq. (42) by

$$J(\alpha) \;=\; B\sin 2\alpha \;+\; B'\cos 2\alpha \;+\; C\,. \tag{43}$$

Corresponding fits are plotted by the solid lines in Figs. 24(b) and (d). Such a behavior of the photocurrents clearly demonstrates the sensitivity of these effects to linear polarization. Note that the offset C actually constitutes the polarization independent effect.

Studying the dependence of the photocurrents on the angle of incidence under linearly polarized excitation exhibits that, in contrast to the excitation with circularly polarized light, the currents in both longitudinal and transversal geometries always result from the superposition of two contributions. One depends only weakly on θ_0, which stems from normal incidence, and the other one is odd in the angle θ_0 (not shown). Moreover, the contributions odd in θ_0 are interconnected: While the longitudinal one behaves as $\cos 2\alpha$ (Stokes parameter s_1), the transverse component is proportional to $\sin 2\alpha$ (s_2).

4.2.2   Discussion of the results and clarifying experiments

The main result obtained with small area graphene flakes is that both the helicity dependent and helicity independent photocurrents have two contributions: (i) an even function of the incidence angle θ_0, which dominates the signal at normal incidence, and (ii) a contribution being odd in the incidence angle, which appears at oblique incidence only. The contributions to the photocurrent odd in the angle θ_0, both circular and linear, stem from the interior

of the graphene sheets and are caused by the high frequency Hall or photon drag effect, as discussed before. The photoresponse at normal incidence, by contrast, can not be related with an ideal bulk material. As this 2D structure possesses a center of space inversion, it does not allow an electric current excited by normally incident light. Thus, the appearance of photocurrents at normal incidence is a clear manifestation of the symmetry reduction of the system [15]. Since all edges of the flakes are illuminated by the relatively large laser spot, the boundaries may be responsible for the lower symmetry and the observed currents.
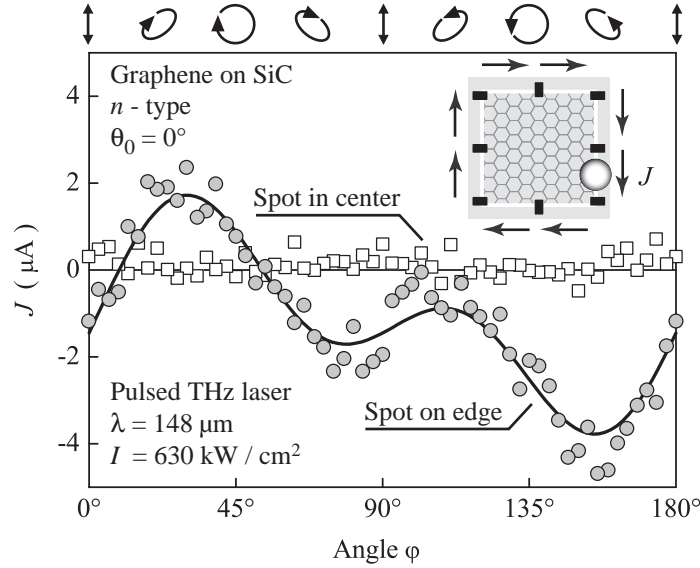
Figure 26: Photocurrent as function of the angle φ in a large area graphene sample due to illumination of boundaries. The circles correspond to the current measured for aligning the laser spot to the edge, see inset, the squares to the signals for exciting the sample's interior.

To unambiguously identify the edges of graphene as origin of the photocurrents, further experiments on large area samples on SiC substrates are carried out. Here, the laser spot is smaller than the samples. An exemplary dependence of the current on the angle φ by illuminating one single edge and picking up the resulting photocurrent over two neighboring contacts is shown in Fig. 26. For this plot, the pulsed high power THz laser with a wavelength of $\lambda = 148$ μm, an intensity of $I = 630$ kW/cm^2 and a spot diameter of $d = 1.7$ mm is

employed. If the laser spot is located in the sample's center under normal incidence, no signal is observed as expected for the ideal honeycomb lattice of graphene and previously described. By contrast, illuminating the sample edge between two contacts results in a photoresponse, which is in good agreement with the phenomenological Eq. (42) and reflects the Stokes parameters of the incident polarized light. A remarkable contribution of the signal is, thereby, caused by the radiation's helicity yielding a current inversion upon switching the circular polarization from right- to left-handed. It is also experimentally observed that for moving the laser spot along the edges around the square shaped sample, the helicity driven edge photocurrent forms a vortex (see inset of Fig. 26), which reverses its sense of rotation upon changing the circular polarization state. Thus, this net electric current stems from the sample edges, which locally reduce the symmetry and yield asymmetric scattering of charge carriers accelerated by the radiation field. The presented dependences are only preliminary results indicating the clear influence of the edges. Therefore, further experiments as well as a model and microscopic theory of the edge photocurrent similarly to the surface photogalvanic effect [98–101] are a future task.

4.3   Summary of photocurrents in graphene

To summarize, the experimental observations demonstrate that the irradiation of monolayer graphene flakes as well as large area graphene on SiC substrates results in directed electric currents of different origins. In all measurements a substantial fraction to the photocurrent is driven by the photon helicity. The current can be separated into contributions resulting from normal and from oblique incidence. The one due to oblique incidence is related to the bulk material and results from the transfer of the photon angular and linear momenta to free carriers. Here, the theory of the high frequency Hall effect describes the helicity driven currents in the classical limit, where the radiation frequency is small compared to the characteristic energy of the carriers. In contrast, the effect at normal incidence is caused by the sample edges and vanishes in the bulk material. This edge photogalvanic effect needs future treatment both experimentally and theoretically.

5 Photocurrents in 2D silicon structures

One peculiarity of graphene being the focus of some theoretical proposals is that electrons can occupy two valleys resulting from the two Dirac points K and K'. These proposals suggest to use the valley degree of freedom as an alternative carrier of information besides the electric charge [8–10]. In this manner, the concept of valleytronics could be developed being similar to spintronics, which utilizes the spin as additional feasibility for information processing. In general, such degeneracies enable one to engineer various distributions of carriers in the momentum, spin and valley spaces. Thereby, a controllable way of occupying a particular spin state or filling a particular valley is a key ingredient, respectively, for spintronics [11] or valleytronics [8,12] both aimed at the development of novel solid-state devices characterized by less dissipation. Appropriate candidates for the realization of valleytronics concepts include not only graphene but also other multi-valley semiconductors such as carbon nanotubes [12] and silicon [12, 13]. A remarkable selective population of the electron states is, thereby, achieved by optical pumping with polarized light: circularly for spin polarization [48] and linearly polarized for "valley polarization" [102]. Besides the selective valley population, the radiation can also cause a particle flux $\boldsymbol{i}_\nu$ within each valley, whose direction and magnitude depend on the valley number ν. In general, the total electric current $\boldsymbol{j} = e\sum_\nu \boldsymbol{i}_\nu$ is non-zero and, thus, measurable by conventional electric methods. However, for special geometries and light polarizations, the partial fluxes $\boldsymbol{i}_\nu$ do exist but the total electric current vanishes. This is the pure valley-orbit current proposed in Ref. [12], which implies the potential use of the valley index in a device in analogy to the pure spin currents in spintronics and topological electronics [103–108].

5.1 Valley-orbit currents driven by polarized light

In this work, a vivid evidence for the existence of pure valley-orbit currents is found. Furthermore, it is demonstrated that the electron fluxes within valleys can be individually controlled by the excitation of (111)-oriented Si-metal-oxide-semiconductor structures with polarized light. This achievement

is confirmed by experimental results obtained by studying the (111)-oriented Si structures. After presenting the experimental findings, the valley-orbit currents are examined by means of a phenomenological model and theory.

5.1.1   Experiments on (111)-oriented Si-MOSFETs

The used experimental geometries for the investigation of valley-orbit currents are illustrated in the insets of Figs. 27 and 29. All experiments are performed at normal incidence of radiation and room temperature. In this setup, the THz radiation causes indirect Drude-like optical transitions in the (111)-oriented Si-MOSFETs. For sample details and properties, see Chap. 3.4. The Stokes parameters $s_1 = |e_x|^2 - |e_y|^2$ and $s_2 = e_x e_y^* + e_y e_x^*$ as well as the degree of circular polarization P_{circ} (see Chap. 3.2) for this geometry depend on the angles α and φ by applying $\lambda/2$- and $\lambda/4$-plates, respectively, as

$$s_1(\alpha) = -\cos 2\alpha \,, \quad s_2(\alpha) = \sin 2\alpha \,,$$
$$s_1(\varphi) = -\frac{1}{2}(\cos 4\varphi + 1) \,, \quad s_2(\varphi) = \frac{1}{2}\sin 4\varphi \,, \quad s_3 = P_{\text{circ}} = \sin 2\varphi \,. \quad (44)$$

The photocurrents are measured between source and drain contacts of the unbiased transistors via the voltage drop across a 50 Ω load resistor.

Irradiating the exact (111) Si-MOSFETs (set 3) with linearly polarized THz radiation at normal incidence generates photocurrent signals with a temporal shape reproducing the laser pulse. The dependence on the azimuth angle α normalized to the laser power in the crystallographic directions x and y for a gate voltage of $V_{\text{g}} = 20$ V and the wavelength of $\lambda = 280$ μm is shown in Fig. 27. The data are well fitted by

$$J_x(\alpha) \; = \; \chi \sin 2\alpha \,, \; J_y(\alpha) \; = \; -\chi \cos 2\alpha \quad (45)$$

with the same prefactor $\chi = -24$ nA/W, in agreement with the Stokes parameters and the theoretical expectation for the point group C_{3v}. It has been checked that, in reference MOSFETs prepared on exact (001) Si surfaces, normal-incidence photocurrents are absent for any polarization of radiation [23], see also Chap. 5.2. In Fig. 28(a), the linear photocurrent contribution, obtained after $J_1 = [J_y(\alpha = 0°) - J_y(\alpha = 90°)]/2 \propto \chi$, for $V_{\text{g}} = 13$ V
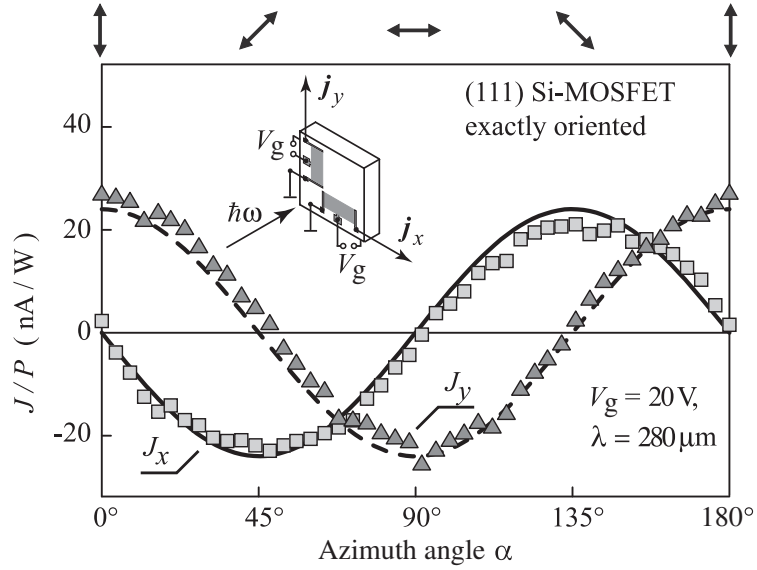
Figure 27: Photocurrent as function of the azimuth angle α measured in the precisely (111)-oriented MOSFET. Lines are fits to Eqs. (45) with one fitting parameter χ. The inset shows the experimental geometry, on top various polarization orientations with respect to the angle α are illustrated.

is presented as function of the wavelength λ. The triangles in Fig. 28 show that, as expected for free-carrier absorption, the signal rises with increasing wavelength following the Drude formula of high-frequency conductivity (full line) [39, 109], see also Chap. 2.1. The variation of the photocurrent with the angle φ presented in Fig. 28(b) clearly demonstrates that the current vanishes for circularly polarized photoexcitation, σ_+ and σ_-, realized at $\varphi = 45°$ and $135°$. The data are obtained in the x direction for a gate voltage of $V_{\mathrm{g}} = 20$ V and the wavelength $\lambda = 280$ μm. The best fit of the dependencies $J_x(\varphi)$ and $J_y(\varphi)$ (not shown) contains no contributions from P_{circ} and reduces to

$$J_x(\varphi) \;=\; \frac{\chi}{2}\sin 4\varphi\,, \quad J_y(\varphi) \;=\; -\frac{\chi}{2}\left(\cos 4\varphi + 1\right), \tag{46}$$

with the same coefficient χ as in Eq. (45).

In the miscut samples (set 4), in contrast, a substantial signal is observed even for circularly polarized light. Figure 29, which is obtained for $V_{\mathrm{g}} = 5$ V and
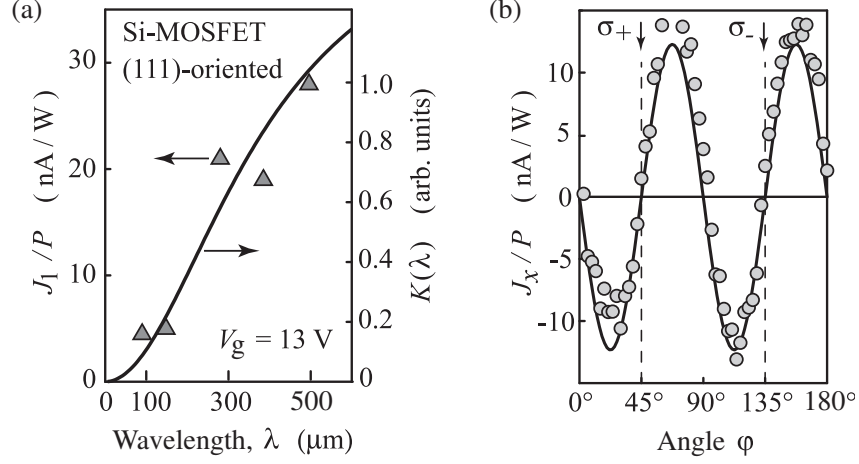
Figure 28: Photocurrent measured in the precisely (111)-oriented MOSFET. (a) Comparison of the wavelength dependencies of the linear photocurrent $J_1 = [J_y(\alpha = 0°) - J_y(\alpha = 90°)]/2 \propto \chi$ (triangles) and the calculated coefficient of free carrier absorption (solid curve). (b) Photocurrent in the x direction as function of the angle φ. The full line is a fit to Eq. (46).

radiation with the wavelength $\lambda = 90$ µm, shows that now the current can be well fitted as a function of the angle φ in the x' and y' directions by

$$J_{x'} = \gamma P_{\text{circ}} + \frac{\chi_1}{2} \sin 4\varphi \,, \quad J_{y'} = \chi_2 - \frac{\chi_3}{2} \left(\cos 4\varphi + 1\right) , \tag{47}$$

what follows from symmetry considerations for the miscut (111) Si transistors of the C_s point group. The best fit is obtained with the coefficients (in nA/W): $\gamma = -1.8$, $\chi_1 = -5.5$, $\chi_2 = -0.8$, and $\chi_3 = -4.0$. As compared with the exact (111) Si sample, the inclination leads to three distinctive features: (i) a current along the x' axis proportional to the radiation helicity P_{circ} is generated under normal incidence, (ii) the current component $J_{y'}$ acquires a polarization-independent contribution, and (iii) the absolute values of the coefficients χ_1 and χ_3 describing the currents induced in x' and y' direction by linearly polarized light become different [17].
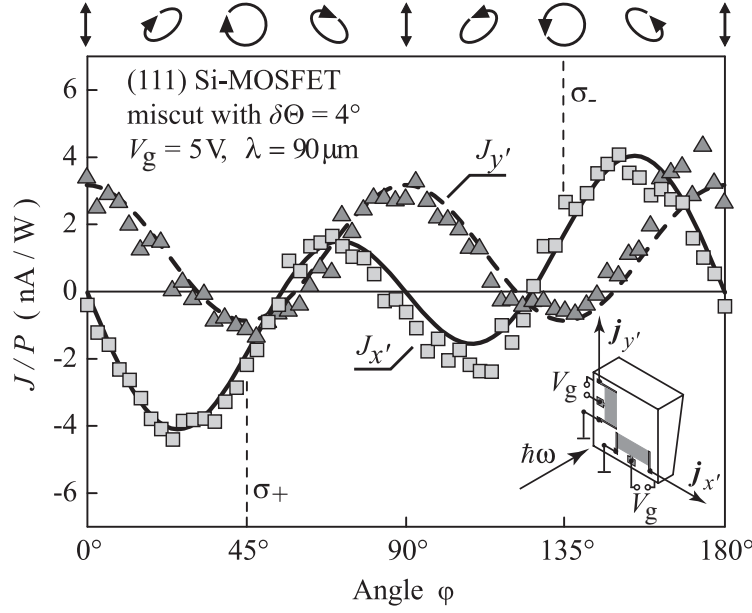
Figure 29: Photocurrent as a function of the angle φ measured in the transistors prepared on the miscut surface. Lines are fits to the phenomenological Eqs. (47). The inset shows the experimental geometry. On top, characteristic polarization ellipses corresponding to various angles φ are illustrated.

5.1.2 Theory and model of valley currents

Below it is demonstrated that the experimental results are a vivid evidence of the existence of pure valley-orbit currents and that the individual control of electron fluxes in valleys is achieved by the excitation of (111)-oriented Si-MOSFETs with polarized light. Such two-dimensional systems contain six equivalent electron valleys [13, 17], see Fig. 30, and possess the overall point-group symmetry C_{3v}, i.e. they are invariant with respect to the rotation by an angle of 120°. The irradiation of (111)-oriented Si-MOS structures leads to an emergence of the fluxes $\boldsymbol{i}_\nu$ in all six valleys, see Fig. 30(a). The generation of the fluxes $\boldsymbol{i}_\nu$ is microscopically caused by the low symmetry of individual valleys, see Fig. 30(b), and stems from asymmetric electron photoexcitation. It is mostly of orbital origin while spin-related mechanisms are negligible due to the vanishingly small spin-orbit coupling in silicon, as already mentioned in Chap. 5.2. Owing to the mass anisotropy in valleys of bulk silicon and

to the valley tilting with respect to the channel normal in (111) structures, the in-plane and out-of-plane motions of carriers are coupled. Therefore, the rates of optical transitions induced by radiation polarized in the channel plane depend on the electron wavevectors. Such an asymmetry of photoexcitation in $\boldsymbol{k}$ space results in a polarization dependent electron flux $\boldsymbol{i}_\nu$. The mechanism of current generation in (111)-oriented Si structures is similar to those considered in Chap. 5.2.4 and Refs. [22, 23, 109, 110], but out of scope of this work.
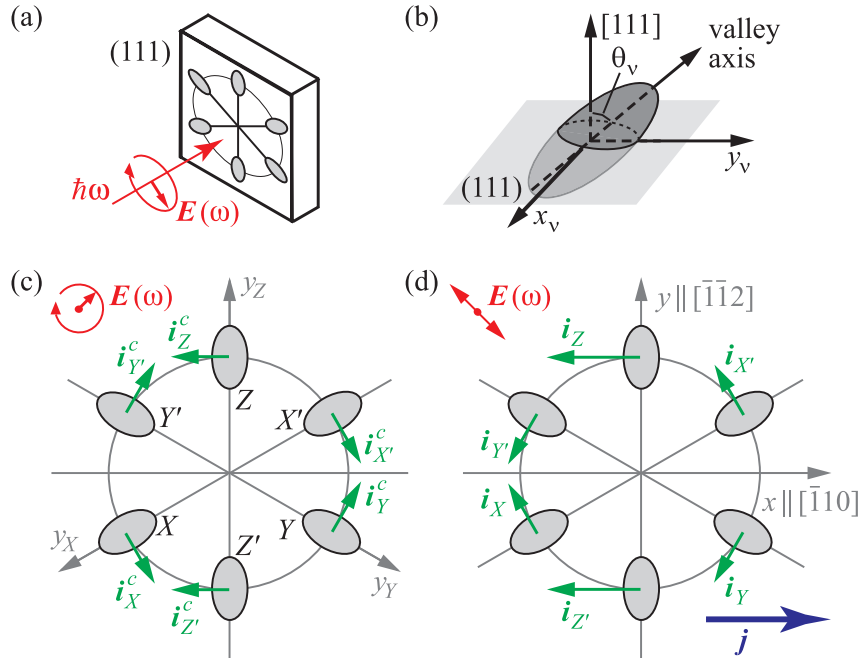
Figure 30: (a) Excitation of (111)-oriented Si-MOS structures with, e.g., circularly polarized light. (b) Orientation of an individual valley. (c) Angular distribution of helicity-dependent fluxes over valleys, $\boldsymbol{i}_\nu^c$, induced in the exact (111) Si-MOSFET under normal incidence of circularly polarized light. The in-plane coordinates y_ν attached to the valleys X, Y and Z are shown. (d) Intravalley fluxes under excitation with linearly polarized light, the total current $\boldsymbol{j} = e \sum_\nu \boldsymbol{i}_\nu \neq 0$.

Instead, the distribution of the fluxes $\boldsymbol{i}_\nu$ over the valleys forming the pure valley-orbit currents or, under certain conditions, an electric current are in the focus below. A symmetry analysis shows that circularly polarized light normally incident upon the sample induces helicity-sensitive intravalley fluxes $\boldsymbol{i}_\nu^c$

in the directions perpendicular to the principal valley axes resulting in a zero net photocurrent, see Fig. 30(c). The fluxes $\boldsymbol{i}_\nu^c$ in this panel are calculated after Eq. (48) based on symmetry arguments and determined by the coefficient A. They are directed perpendicularly to the valley principal axes and compensate each other to nullify the net electric current. On the other hand, the theory allows the generation of a total electric current by normally incident and linearly polarized radiation, see Fig. 30(d). The directions and magnitudes of fluxes in valleys are calculated after Eq. (48) in a particular case of $C = D = 0$. However, the choice of the parameters does not affect the polarization dependence of the total current $\boldsymbol{j}$, see Eq. (51). Thus, the first experimental evidence of valley currents in (111) Si-MOS structures is the lack of a net photocurrent for circularly polarized light and its observation for linear polarization. This is indeed obtained in experiments, see Figs. 27 and 28, where a clear dependence on linearly but no response to circularly polarized light is observed. Note that the exemplary situation of an angle of $\alpha = 135°$ shown in Fig. 30(d) exactly reflects the experimental finding of Figs. 27 and 28, where, for the same azimuth angle α, no current J_y, but the maximum positive signal in x direction is observed. A further confirmation is the appearance of a photocurrent in samples with broken equivalence of valleys, e.g., in structures with the surface normal $\boldsymbol{n}$ slightly tilted from the [111] axis, as demonstrated by the dependence on the angle φ in Fig. 29.

The experimentally observed dependencies (45)-(47) are readily obtained by summing up the photocurrents $\boldsymbol{j}_\nu = e\boldsymbol{i}_\nu$ induced in individual valleys. Each valley ν ($\nu = X, Y, Z, X', Y'$ and Z', see Fig. 30) has only one non-trivial symmetry element, the reflection $x_\nu \to -x_\nu$, described by the point group C_s. Here, the following in-plane coordinate frame is used: The axis x_ν is perpendicular to the plane containing the principal valley axis and the channel normal $\boldsymbol{n}$, and the axis y_ν lies in this plane. Particularly, for $\boldsymbol{n} \parallel$ [111], the axes x_Z and y_Z coincide with $[\bar{1}10]$ and $[\bar{1}\bar{1}2]$, respectively. The current density emerging in the valley ν is phenomenologically given by [23]

$$
\begin{aligned}
j_{x_\nu}^{(\nu)}/I &= A(\theta_\nu)\, P_{\text{circ}} + B(\theta_\nu)\, (e_{x_\nu} e_{y_\nu}^* + e_{y_\nu} e_{x_\nu}^*)\,, \\
j_{y_\nu}^{(\nu)}/I &= C(\theta_\nu) + D(\theta_\nu)\, (|e_{x_\nu}|^2 - |e_{y_\nu}|^2)\,,
\end{aligned}
\tag{48}
$$

where I is the light intensity, $A(\theta_\nu)$, $B(\theta_\nu)$, $C(\theta_\nu)$, and $D(\theta_\nu)$ are polarization-independent coefficients, θ_ν is the angle between the normal $\boldsymbol{n}$ and the principal axis of the valley ν, e_{x_ν} and e_{y_ν} are the projections of the polarization vector $\boldsymbol{e}$ on the x_ν and y_ν axes, respectively.

The total electric current is a sum of the single-valley contributions $\boldsymbol{j}^{(\nu)}$. In fact, the contributions due to the valleys X, X' (or Y, Y' and Z, Z') coincide so that the total photocurrent simplifies to

$$\boldsymbol{j} \;=\; 2 \sum_{\nu=X,Y,Z} \boldsymbol{j}^{(\nu)} \,. \tag{49}$$

By projecting all the partial vectors $\boldsymbol{j}^{(\nu)}$ on the transistor axes x and y (or x' and y') one obtains

$$
\begin{aligned}
j_x &= 2 \sum_{\nu=X,Y,Z} \left[j_{x_\nu}^{(\nu)} \cos\phi_\nu - j_{y_\nu}^{(\nu)} \sin\phi_\nu \right] \,, \\
j_y &= 2 \sum_{\nu=X,Y,Z} \left[j_{x_\nu}^{(\nu)} \sin\phi_\nu + j_{y_\nu}^{(\nu)} \cos\phi_\nu \right] \,,
\end{aligned}
\tag{50}
$$

where ϕ_ν is the angle between the axes x_ν and x.

In the exact (111) Si-MOS structure, all valleys are equivalent, $\theta_\nu = \Theta_0$ with $\cos\Theta_0 = 1/\sqrt{3}$, and the in-plane angles ϕ_ν are given by $\phi_X = -\phi_Y = 120°$, $\phi_Z = 0$. Therefore, one can derive the current density per light intensity

$$
\begin{aligned}
j_x/I &= 3\,(B_0 + D_0)\,(e_x e_y^* + e_y e_x^*) \,, \\
j_y/I &= 3\,(B_0 + D_0)\,(|e_x|^2 - |e_y|^2) \,,
\end{aligned}
\tag{51}
$$

where $B_0 = B(\Theta_0)$ and $D_0 = D(\Theta_0)$. Equation (51) exactly reproduces the experimentally observed polarization dependencies (45)-(46) with the fitting parameter χ given by $3(B_0 + D_0)$. Thus, in conclusion, while both circularly polarized and unpolarized radiation give rise to electric currents $\boldsymbol{j}_\nu$ in all valleys, the total photocurrent can only be excited by linearly polarized light.

To describe the photocurrent in miscut structures, the polar angles Θ and Φ of the normal $\boldsymbol{n}$ in the Cartesian system [100], [010], [001] are introduced. If the channel normal $\boldsymbol{n}$ is close to [111], then the angles Θ and Φ are close to

Θ_0 and $\Phi_0 = 45°$, respectively. By expanding ϕ_ν and θ_ν in powers of $\delta\Theta = \Theta - \Theta_0$ and $\delta\Phi = \Phi - \Phi_0$ one can derive the expression for the photocurrent in miscut structures. In the approximation linear in $\delta\Theta$ and $\delta\Phi$, the total helicity-dependent current reduces to

$$\boldsymbol{j}^c/I \;=\; Q\,P_{\text{circ}}\left(\boldsymbol{l}\times\boldsymbol{n}\right), \tag{52}$$

where $Q = 3\left(A_0/\sqrt{2} + A_0'\right)$, $A_0' = dA/d\theta|_{\theta=\Theta_0}$, and $\boldsymbol{l}$ is the unit vector along the crystallographic axis [111]. While deriving Eq. (52) it was taken into account that (i) for a fixed value of the total electron density, the electron chemical potential is independent of $\delta\Theta$ and $\delta\Phi$, (ii) the angles θ_ν are expressed in terms of $\delta\Theta$, $\delta\Phi$ by $\theta_Z = \Theta_0 + \delta\Theta$ and $\theta_{X,Y} = \Theta_0 - \delta\Theta/2 \pm \delta\Phi/\sqrt{2}$, and (iii) the components $(\boldsymbol{l}\times\boldsymbol{n})_{x'}$ and $(\boldsymbol{l}\times\boldsymbol{n})_{y'}$ are given by $\delta\Theta$ and $\sqrt{2/3}\,\delta\Phi$, respectively. Equation (52) shows that the helicity-dependent photocurrent excited by normally incident radiation appears only in miscut structures and in the direction perpendicular to the inclination axis. Indeed, this behavior is observed in all Si-MOSFETs studied in experiment, see Figs. 28(b) and 29. In fact, the observation of the circular photogalvanic effect in miscut samples, where the equivalence of valleys is disturbed, demonstrates that photocurrents in individual valleys are efficiently generated. It follows from the experimentally measured value of the ratio γ/χ_3 and from Eq. (52) that the ratio between $A_0/\sqrt{2} + A_0'$ and $B_0 + D_0$ amounts 5. An estimation based on the microscopic theory [22,109] of orbital mechanisms of dc currents driven by ac electric fields gives for the latter ratio a value of unity. This mismatch needs a further analysis.

Furthermore, the valley currents with zero net charge transfer can be classified according to their behavior under symmetry operations. In (111)-oriented Si-MOS structures of the C_{3v} point group, the pure valley currents can belong to the irreducible representations A_1, A_2 and E [28]. The scalar representation A_1 describes the pure valley current $j_{\text{valley}}^{(A_1)} = \sum_\nu j_{y_\nu}^{(\nu)}$; this current is excited by normally incident unpolarized radiation. The pseudo scalar representation A_2 describes the valley current $j_{\text{valley}}^{(A_2)} = \sum_\nu j_{x_\nu}^{(\nu)}$, which changes its sign upon reflection in any of the three mirror planes of the point group C_{3v}. The contribution $j_{\text{valley}}^{(A_2)}$ is induced by circularly polarized radiation, see Fig. 30(c), and reverses

its sign upon inversion of the photon helicity. Finally, the two-dimensional vector representation E describes the valley current with the components

$$
\begin{aligned}
j_{\text{valley},x}^{(E)} &= \left(2j_{xZ}^{(Z)} - j_{xX}^{(X)} - j_{xY}^{(Y)}\right) + \sqrt{3}\left(j_{yX}^{(X)} - j_{yY}^{(Y)}\right), \\
j_{\text{valley},y}^{(E)} &= \left(-2j_{yZ}^{(Z)} + j_{yX}^{(X)} + j_{yY}^{(Y)}\right) + \sqrt{3}\left(j_{xX}^{(X)} - j_{xY}^{(Y)}\right).
\end{aligned} \tag{53}
$$

The polarization dependence of the pure valley current $\boldsymbol{j}_{\text{valley}}^{(E)}$ excited by normally incident and linearly polarized radiation is given by Eq. (51), where D_0 is replaced by $-D_0$ [17].

5.1.3   Summary and outlook of valley currents

In conventional electric measurements, the pure valley currents are hidden and special methods are needed to reveal them. A possible experiment to observe $j_{\text{valley}}^{(A_2)}$ is the generation of the second harmonic. Indeed, under normal incidence of the probe light, the dielectric polarization at the second harmonic frequency is given by

$$
\begin{aligned}
P_x^{(2)} &= \chi_{xxy}^{(2)}\, 2\,\mathcal{E}_x \mathcal{E}_y + \chi_{xxx}^{(3)}\, j_{\text{valley}}^{(A_2)}\left(\mathcal{E}_x^2 - \mathcal{E}_y^2\right), \\
P_y^{(2)} &= \chi_{xxy}^{(2)}\left(\mathcal{E}_x^2 - \mathcal{E}_y^2\right) - \chi_{xxx}^{(3)}\, j_{\text{valley}}^{(A_2)}\, 2\,\mathcal{E}_x \mathcal{E}_y,
\end{aligned} \tag{54}
$$

where $\mathcal{E}$ is the probe electric-field amplitude, $\chi_{xxy}^{(2)} = \chi_{yxx}^{(2)} = -\chi_{yyy}^{(2)}$ the second-order susceptibility of the equilibrium system and $\chi_{xxx}^{(3)} = -\chi_{xyy}^{(3)} = -\chi_{yxy}^{(3)}$ the third-order susceptibility (the second order in $\mathcal{E}$ and the first in $j_{\text{valley}}^{(A_2)}$). Note that the effect of the gate voltage on the generation of the second harmonic has been previously observed in (001) Si-MOSFETs [111]. Another possibility to reveal the pure valley currents is the *orbital* Kerr or Faraday rotation. In this case, the polarization of the probe beam is rotated by the angle $\Phi \propto j_{\text{valley}}^{(A_2)}$ caused by the pure valley-orbit current, similar to spin Kerr or Faraday effect.

To summarize, it is demonstrated that pure valley-orbit currents can be generated by optical excitation of multi-valley semiconductors. The appearance of a pure valley current is a specific feature of semiconductors with several equivalent valleys such as graphene, carbon nanotubes and silicon, the latter being in focus of this work. The electron fluxes in valleys can be individually

controlled by simple means, namely, by variation of the light's polarization or by the disturbance of the valleys' equivalence. The latter can be achieved, e.g., by the application of strain. A controllable way of a selective occupation of valleys and the generation of pure orbit-valley currents are key ingredients for valleytronics aimed at the development of novel solid-state devices with less power dissipation [17].

5.2   Orbital photogalvanic effects

So far, only the phenomenological current distribution but not the microscopic mechanisms underlying the generation of photocurrents in silicon are addressed. Therefore, the concept of orbital roots resulting in photogalvanic effects is discussed in the following. The linear and circular photogalvanic effect, representing the generation of a directed current due to the asymmetry of photoexcitation or relaxation processes, are, thereby, only allowed in media of sufficiently low spatial symmetry. This low symmetry required for the photogalvanic effects is naturally realized in non-centrosymmetric semiconductors and low-dimensional structures based on them. However, it has been shown that both the LPGE and the CPGE can occur even in two-dimensional structures made of centrosymmetric crystals, e.g., silicon, due to the structure inversion asymmetry [30, 110, 112]. The LPGE in Si-MOSFETs was observed almost twenty years ago [113], but the first experiments on the CPGE, which reverses the current direction upon switching the sign of circular polarization, have been reported just recently by our group [22]. These experiments were carried out on MOSFETs fabricated on miscut silicon surfaces and provided the first prove that the photon-helicity sensitive photocurrent can be not only of spin-dependent origin, as commonly considered [18, 19, 114] (see also Chap. 2.2.3) but also be caused by pure orbital effects.

Therefore, this chapter presents a comprehensive experimental and theoretical study of THz radiation induced photogalvanic effects in Si-MOSFETs fabricated on exactly (001)-oriented as well as on miscut surfaces. The fact that a circular (photon helicity sensitive) photocurrent exists in Si-based structures is of particular interest. It demonstrates that the CPGE current caused by the transfer of photon angular momenta to free carriers can be generated not

only in structures with a strong spin-orbit interaction due to spin-dependent optical excitation [18, 19, 114], but even in systems with a vanishingly small constant of spin-orbit coupling. In this chapter, it is demonstrated that the circular photocurrent in silicon-based structures is of pure orbital nature originating from the quantum interference of different pathways contributing to the Drude absorption of monochromatic radiation [22, 112]. Besides this quantum mechanical approach, also a classical model based on the high frequency conductivity under asymmetric photoexcitation is introduced.

5.2.1 Experiments on (001)-oriented Si-MOSFETs

Irradiating the Si-MOSFET structures with high power pulsed THz radiation induces photocurrent signals with a temporal shape reproducing that of the laser pulse, which has a duration of about 100 ns. Figure 31 shows polarization dependences of the measured currents in both the y direction on the precisely (001)-oriented surface (panels (a) and (b)) and in the transistor along x' on the miscut surface (panels (c) and (d)). The insets illustrate the experimental setups for the Si-MOSFET, which are already described in Chap. 3.4. The data are obtained at room temperature, for an applied gate voltage of $V_{\mathrm{g}} = 15$ V, and at oblique and normal incidence of radiation for the former and latter structures, respectively. The photon energy in this plot is $\hbar\omega = 4.4$ meV, corresponding to the wavelength $\lambda = 280$ μm. This yields a peak power ≈ 6.5 kW and a diameter of the laser spot of about 2.5 mm.

First, the polarization dependences of the photocurrents in (001)-oriented Si structures (set 1) are specified. Figure 31(a) shows the photoresponse $J_y(\varphi)$ measured perpendicular to the light propagation at oblique incidence of radiation in the plane (xz) for an angle $\theta_0 = 30°$. The light polarization states for several angles φ for this particular experimental geometry are sketched on the top of Fig. 31(a). Obviously, the signal reverses its sign upon switching the radiation helicity from right- to left-handed circular polarization, i.e. from $\varphi = 45°$ to $135°$ in this geometry, respectively. This is the characteristic fingerprint of the circular photogalvanic effect [28, 29, 31, 45], already pointed out in Chap. 2.2.3. In addition, the photocurrent has a contribution independent
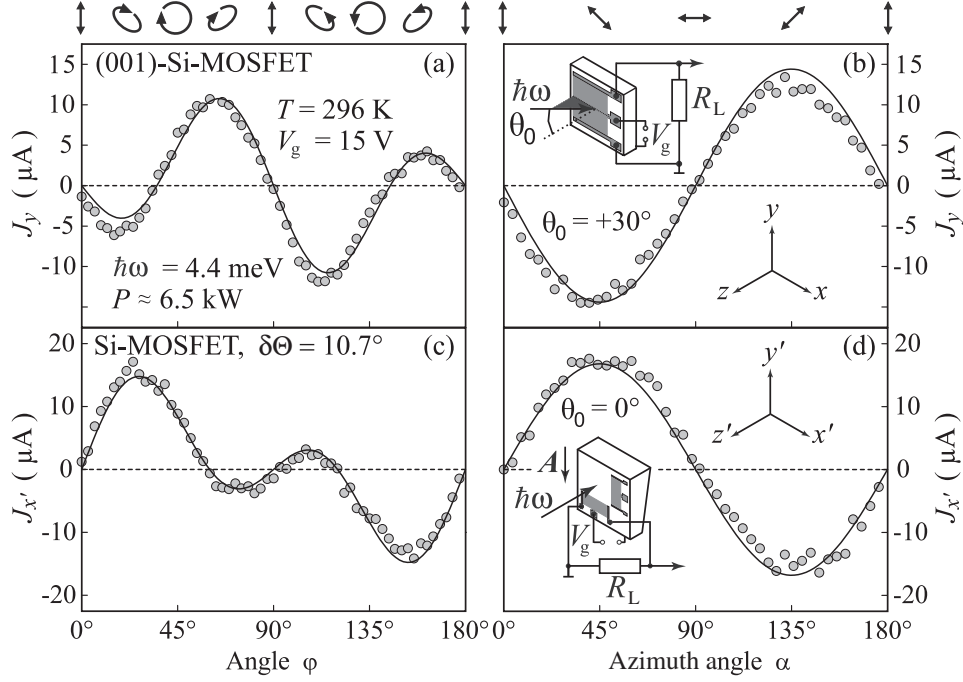
Figure 31: Polarization dependences of the photocurrents measured in transistors on the (001)-oriented surface ((a) and (b)) and on the miscut surface ((c) and (d)). Panels (a) and (c) show the photocurrent as a function of the angle φ, which determines the radiation helicity, panels (b) and (d) the photocurrent in dependence on the azimuth angle α. The insets sketch the experimental setups for the different structures. On top, characteristic polarization states of various angles φ and α are illustrated.

of the photon helicity, but sensitive to the linear polarization of the radiation. The whole dependence $J_y(\varphi)$ can be well fitted by

$$J(\varphi) \;=\; J^{\mathrm{LPGE}}\,(1/2)\sin 4\varphi \;+\; J^{\mathrm{CPGE}}\,\sin 2\varphi\,, \tag{55}$$

with comparable parameters J^{LPGE} and J^{CPGE}. The first and second terms on the right-hand side of Eq. (55) correspond to the linear and circular photogalvanic effects, respectively, see below. By varying the angle of incidence θ_0 from $-30°$ to $+30°$ both contributions to the photocurrent reverse their signs. Moreover, by changing the plane of incidence from (xz) to (yz), the

photon helicity driven current in the y direction vanishes and only the LPGE contribution remains.

The dependence on the angle φ demonstrates that the photocurrent can also be induced by linearly polarized radiation. In the case of purely linearly polarized light, the signal should solely be caused by the LPGE. Therefore, the dependence of J_y on the azimuth angle α is presented in Fig. 31(b). The current behavior on rotating the orientation of linearly polarized light in respect to the y axis can be well fitted by

$$J(\alpha) \;=\; J^{\mathrm{LPGE}} \sin 2\alpha \,, \tag{56}$$

with the same parameter J^{LPGE} used in Eq. (55).

Subsequently, the results obtained from the transistors made on miscut surfaces (set 2) are discussed. In contrast to exactly (001)-oriented structures, here a photocurrent can be observed even at normal incidence of radiation (Figs. 31(c) and (d)). This difference follows from symmetry arguments discussed below. The photon helicity dependent current is thereby detected only in the transistor along $x' \parallel [1\bar{1}0]$. Thus, this particular geometry is in the focus of discussion in the following. The polarization dependences $J_{x'}(\varphi)$ and $J_{x'}(\alpha)$ can also be described by Eqs. (55) and (56), respectively, with another set of fitting parameters. Note that, in contrast to (001)-oriented structures, the photocurrent in miscut samples is determined by the crystallographic axes rather than by the light propagation direction.

The contributions of the circular and linear photogalvanic effects J^{CPGE} and J^{LPGE} persist for all applied gate voltages from 1 to 20 V, photon energies and temperatures used in the experiments on both types of MOSFETs. Hereby, these contributions can be obtained by $J^{\mathrm{CPGE}} = [J(\varphi = 45°) - J(\varphi = 135°)]/2$ and $J^{\mathrm{LPGE}} = [J(\alpha = 45°) - J(\alpha = 135°)]/2$, respectively. First, the gate voltage dependences of the CPGE (Fig. 32(a)) and LPGE (Fig. 32(b)) contributions measured at room temperature are described. The data are obtained for the photon energy 8.4 meV (or $\lambda = 148$ µm), the power ≈ 30 kW, and the diameter of the laser spot of about 2 mm. For this wavelength, as well as the most other studied photon energies, an increase in the gate voltage V_{g} results in a rise of the photocurrent magnitude. Such a behavior can be attributed to

Figure 32: Gate voltage dependences of (a) the circular and (b) the linear photogalvanic currents measured in the transistors on the (001)-oriented transistor for $\theta_0 = 30°$ and the miscut surface with $\delta\Theta = 10.7°$ for normal incidence. The inset shows the behavior of the circular photocurrent for the photon energy 16.3 meV in the miscut MOSFET with the inclination angle 9.7°.

the increasing electron density N_s in the inversion channel and, therefore, the enhancement of Drude absorption. For a detailed explanation of this absorption process, see Chap. 2.1. However, while the LPGE contribution always increases with V_g, the CPGE exhibits a sign inversion at some photon energies with raising V_g, as demonstrated for the photon energy $\hbar\omega = 16.3$ meV ($\lambda = 76$ μm) in the inset in Fig. 32(a). Note that this gate voltage can not be

attributed to any characteristic energy in the band structure of silicon-based quantum-confined channels.
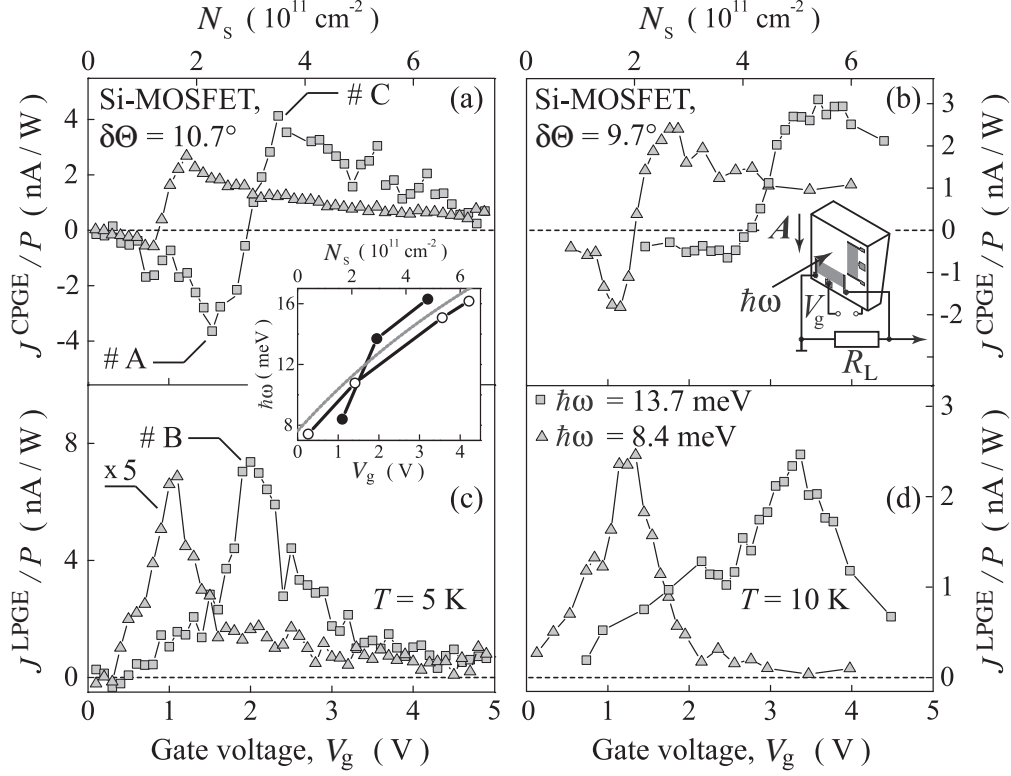
Figure 33: Dependences of the circular (panels (a) and (b)) and linear (panels (c) and (d)) photogalvanic current on the gate voltage V_g and, thus, the carrier density N_s. The data are obtained at transistors on miscut surfaces with different inclination angles. The letters #A, #B and #C denote the characteristic gate voltages, at which the temperature dependences of Fig. 34 are measured. Full circles in the inset show the relation between the photon energy and gate voltage of the inversion point of the CPGE. The open circles and solid curve demonstrate the relation between the photon energy and gate voltage corresponding to the intersubband resonance in (001)-oriented MOSFETs obtained by absorption measurements [115] and calculated numerically [116], respectively.

The most spectacular discrepancy in the CPGE and LPGE behavior emerges at helium temperature. While the polarization dependences remain the same,
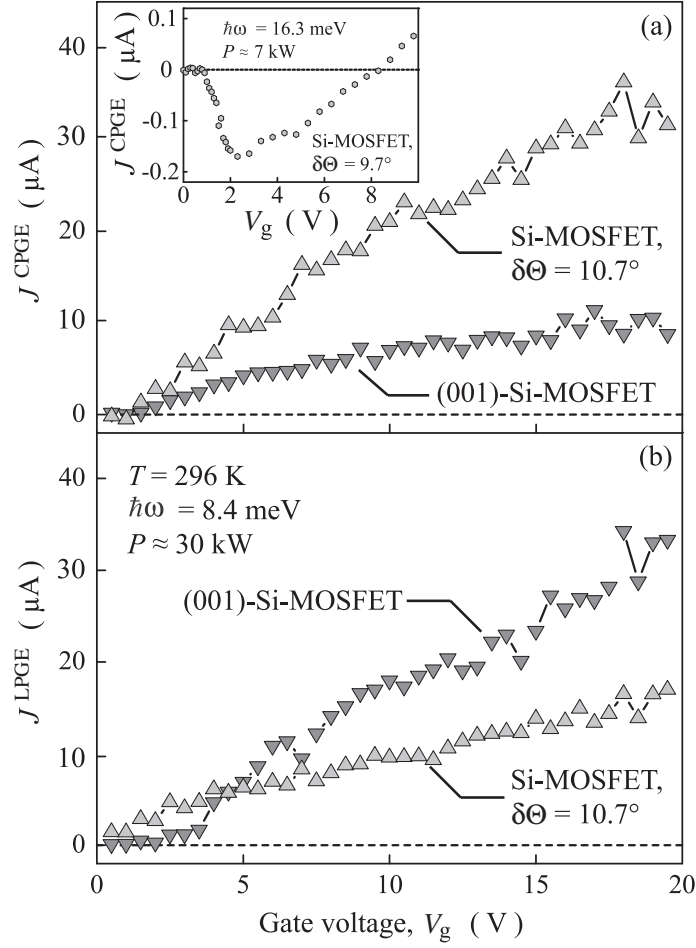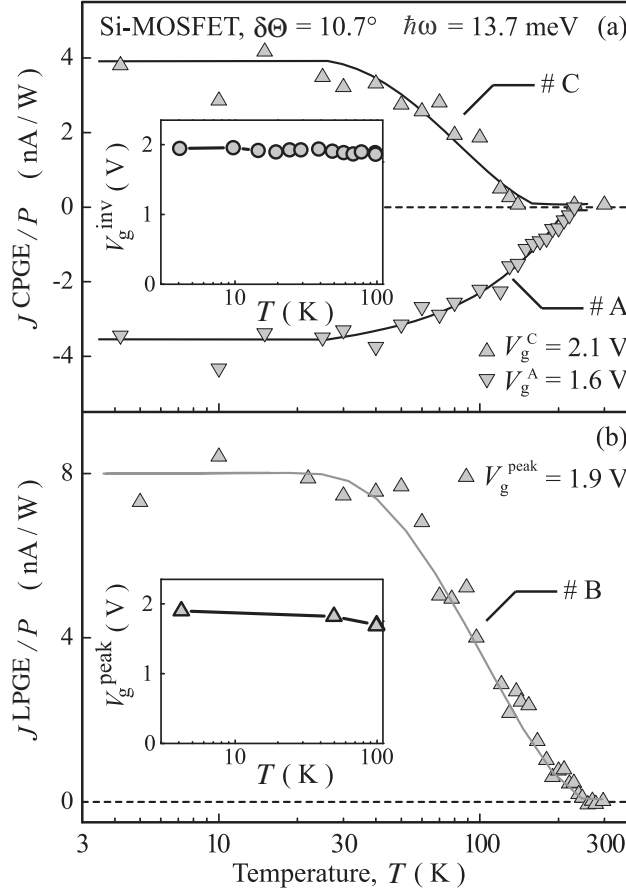
Figure 34: Temperature dependences of (a) the circular and (b) the linear photogalvanic current measured in the transistor on the miscut surface with $\delta\Theta = 10.7°$ at characteristic gate voltages indicated by the letters #A, #B and #C in Fig. 33. The insets show the gate voltage corresponding to the CPGE sign inversion, V_g^{inv}, as well as the gate voltage corresponding to the LPGE peak, V_g^{peak}, as function of the temperature.

the gate voltage dependences get consistently different. In contrast to the smooth behavior observed at room temperature, at helium temperature the LPGE current exhibits a resonance-like response and the CPGE photocurrent shows always a sign inversion. This is shown in Fig. 33 for two miscut Si-MOSFETs with different angles of inclination $\delta\Theta = 10.7°$ and 9.7°. The data of the two photon energies 8.4 meV and 13.7 meV ($\lambda = 148$ and 90 μm),

normalized to the laser power, are presented in this figure. The peak position of the LPGE current, which coincides with the inversion point of the CPGE, depends on the photon energy $\hbar\omega$ and corresponds to $\hbar\omega \approx \varepsilon_{21}$, where ε_{21} is the energy separation of the first two electron subbands. The latter is in accordance with band structure calculations [116] and experiments on far infrared absorption [115] (see inset to Fig. 33) as well as with photoconductivity measurements (not shown). The resonance condition is obtained by tuning the energy separation between the first two electron subbands ε_{21} to the photon energy $\hbar\omega$ by changing the gate voltage: Increasing the photon energy shifts the intersubband resonance to larger gate voltages [61]. The discrepancy in the resonance positions for a fixed photon energy observed in the two miscut samples is attributed to the difference of their inclination angles.

By increasing the temperature from liquid helium to room temperature, the resonant peak of the LPGE and as well as the sign inversion of the CPGE at $\hbar\omega \approx \varepsilon_{21}$ vanish. This is shown in Fig. 34, where the normalized temperature dependences of J^{CPGE} and J^{LPGE} are plotted for $\hbar\omega = 13.7$ meV, for three characteristic gate voltages: All three signals remain almost constant below about 35 K and decrease for higher temperatures. The insets in Fig. 34(a) and (b) demonstrate that the inversion point of the CPGE, $V_{\mathrm{g}}^{\mathrm{inv}}$, and the peak position of the LPGE, $V_{\mathrm{g}}^{\mathrm{peak}}$, do not shift with temperature as far as they are detectable. This is in agreement with the behavior of $\varepsilon_{21}(T)$ well known for MOSFETs [61]. At $T > 120$ K, the gate voltage dependences of the current contributions become smooth, similar to those observed at room temperature.

5.2.2   Orbital mechanisms of the photogalvanic effects

5.2.2.1   Phenomenological theory: To understand the behavior of the observed photocurrents, first the phenomenological equations for the linear and circular photogalvanic effect, which were introduced in Chap. 2.2, are applied to the two point-group symmetries $C_{\infty v}$ and C_s, relevant to electron channels on precisely (001)-oriented and miscut silicon surfaces, respectively. Two-dimensional channels on a (001) surface can be effectively described by the axial point-group $C_{\infty v}$, which takes into account the structure inversion asymmetry of the channel. In such structures, the photocurrent can be excited only

at oblique incidence of radiation ($\theta_0 \neq 0°$, $E_z \neq 0$), and its components are given by the phenomenological equations

$$
\begin{aligned}
j_x &= L\,(E_x E_z^* + E_z E_x^*)\ +\ C\,\mathrm{i}\,(\boldsymbol{E} \times \boldsymbol{E}^*)_y\,, \\
j_y &= L\,(E_y E_z^* + E_z E_y^*)\ -\ C\,\mathrm{i}\,(\boldsymbol{E} \times \boldsymbol{E}^*)_x\,,
\end{aligned}
\tag{57}
$$

where the first and second terms on the right-hand side of Eqs. (57) stand for the LPGE and CPGE, respectively, x and y are the in-plane axes, and $z \parallel [001]$ is the channel normal. Thus, the experimental results in dependence on the angel φ presented in Fig. 31(a) and fitted by Eq. (55) are in full agreement with the phenomenological Eq. (57), since the polarization dependent terms are reduced to $(E_y E_z^* + E_z E_y^*) = -(1/2)(E_0^2\, t_p t_s) \sin\theta \sin 4\varphi$ and $\mathrm{i}(\boldsymbol{E} \times \boldsymbol{E}^*)_x = E_0^2\, t_p t_s \sin\theta \sin 2\varphi$ in this experimental geometry. Here, E_0 is the electric field amplitude of the incident light, t_p and t_s are the amplitude transmission coefficients for s- and p-polarized radiation, θ is the angle of refraction related to the incidence angle by $\sin\theta = \sin\theta_0/n_\omega$ with the refraction index of the medium n_ω. For rotating purely linearly polarized light about the angle α, Eq. (57) reduces to $(E_y E_z^* + E_z E_y^*) = -E_0^2\, t_p t_s \sin\theta \sin 2\alpha$, in agreement with Fig. 31(b) and Eq. (56).

The channels fabricated on miscut surfaces exhibit the lower point-group symmetry C_s due to the deviation of the channel plane from (001) together with the asymmetry of the confinement potential [30, 110]. In structures of the C_s point group, both linear and circular photogalvanic effects are allowed even at normal incidence of radiation ($\theta_0 = 0°$, $E_z = 0$) [18]. In this particular geometry, the photocurrent components are phenomenologically described by

$$
\begin{aligned}
j_{x'} &= L_1'\,(E_{x'} E_{y'}^* + E_{y'} E_{x'}^*)\ +\ C'\,\mathrm{i}\,(\boldsymbol{E} \times \boldsymbol{E}^*)_{z'}\,, \\
j_{y'} &= L_2'\ +\ L_3'\,(|E_{x'}|^2 - |E_{y'}|^2)\,.
\end{aligned}
\tag{58}
$$

Here, the channel plane $(x'y')$ is assumed to be tilted from the plane (001) around the axis $x' \parallel [1\bar{1}0]$, and z' is the channel normal. In contrast to (001)-oriented MOSFETs, the photocurrent in structures on miscut surfaces can be induced even by unpolarized radiation. The results from the miscut Si-MOSFETs (see Figs. 31(c) and (d)) are in full accordance with the

phenomenological Eq. (58), since at normal incidence $(E_{x'} E_{y'}^* + E_{y'} E_{x'}^*) = -(1/2)(E_0 \, t_s)^2 \sin 4\varphi$, $\mathrm{i}(\boldsymbol{E} \times \boldsymbol{E}^*)_{z'} = -(E_0 \, t_s)^2 \sin 2\varphi$, and $(E_{x'} E_{y'}^* + E_{y'} E_{x'}^*) = -(E_0 \, t_s)^2 \sin 2\alpha$.

The microscopic theory of the photogalvanic effects caused by intersubband optical transitions in silicon-based low-dimensional structures was developed in Ref. [110]. This theory describes well the resonance behavior of the linear photogalvanic effect measured at low temperatures. The observation of the photogalvanic effects apart the intersubband resonance demonstrates that the free carrier Drude absorption also gives rise to a polarization dependent photocurrent. Below the microscopic theory of the CPGE in both (001)-oriented and miscut Si-MOSFETs is presented. As addressed above, the generation of helicity dependent photocurrents in silicon-based structures is of particular interest, because spin-related mechanisms of the CPGE are ineffective due to the vanishingly small constant of spin-orbit coupling in silicon. Therefore, less studied pure orbital mechanisms determine the current formation. Below, this process is considered theoretically following Ref. [112] and the photocurrent is calculated taking into account the peculiarity of the silicon band structure.

As already mentioned in Chap. 2.4, the electron subbands in Si structures are formed by six valleys X, X', Y, Y', Z and Z' located at the Δ points of the Brillouin zone of the bulk crystal. The electron dispersion in each valley is strongly anisotropic and described by two different effective masses: longitudinal $m_\parallel$ and transverse $m_\perp$ with respect to the principle axis of the valley. Due to quantum confinement, only two valleys, Z and Z', are occupied at low temperatures and low electron densities in structures grown along $z \parallel$ [001], while the other four valleys are considerably higher in energy. The low-energy valleys are almost equivalent and can be treated independently, because the valley splitting caused by the asymmetry of the confining potential is negligible in comparison to the kinetic energy of electrons and because inter-valley scattering is much weaker than intra-valley processes [23, 61].

5.2.2.2   The CPGE in (001)-oriented structures: The model illustrating the generation of a photocurrent due to free-carrier Drude absorption of circularly polarized radiation is sketched in Fig. 35. Panel (a) shows indirect optical tran-
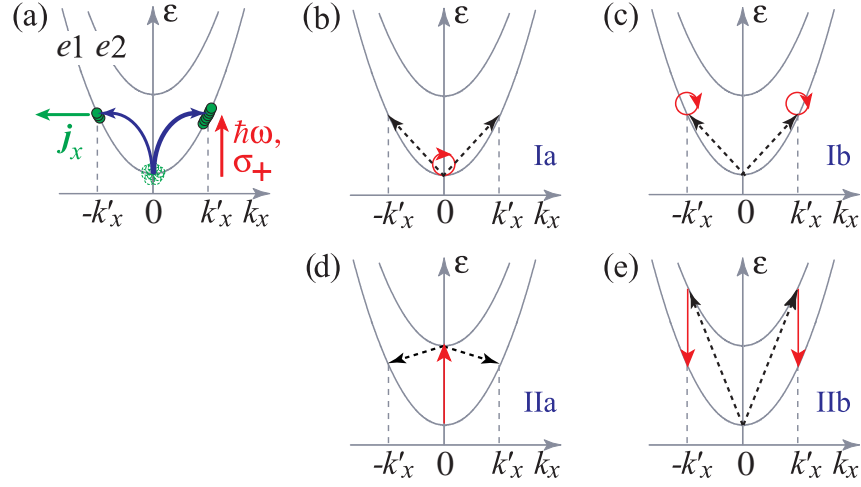
Figure 35: Microscopic model of the CPGE. (a) Indirect optical transitions due to free-carrier absorption of circularly polarized radiation are shown by bent arrows of various thickness indicating the difference in transition rates, which is caused by the quantum interference of various absorption pathways. Full circles sketch the resulting imbalance of the carrier distribution in the momentum space yielding an electric current j_x. (b) - (e) Various pathways of radiation absorption involving intermediate states in the subbands $e1$ and $e2$. Red solid arrows indicate electron-photon interaction and black dashed arrows describe scattering events.

sitions within the subband $e1$. Here, only the ground subband is assumed to be populated in equilibrium. For fulfilling the conditions of energy and momentum conservation in this case, the transitions can only occur if the electron-photon interaction is accompanied by simultaneous electron scattering by phonons or static defects, as already discussed in Chap. 2.1. Such indirect transitions are theoretically treated as second-order virtual processes via intermediate states. They can be located within the same quantum subband $e1$ as well as in other conduction or valence subbands. Figures 35(b) and (d) illustrate possible absorption pathways with intermediate states in the electronic ground subband $e1$ and the first excited subband $e2$.

The pathway, which is usually considered and determines the structure absorbance at normal incidence, involves intermediate states within the subband

$e1$. Such transitions (path I) are shown in Fig. 35(b) and (c) for the process, where the electron-photon interaction is followed by electron scattering (panel (b)) and the inverted sequence process (panel (c)). The matrix element of such kind of transition processes has the form

$$M^{(1)}_{\boldsymbol{k'k}} \;=\; \frac{eA}{c\omega m_\perp}\, \boldsymbol{e}\cdot(\boldsymbol{k'}-\boldsymbol{k})\, V_{11}\,, \tag{59}$$

where $\boldsymbol{k}$ and $\boldsymbol{k'}$ are the initial and final electron wavevectors, respectively, e is the electron charge, c the speed of light, A the amplitude of the vector potential of the electromagnetic wave, which is related to the radiation intensity by $I = A^2\omega^2 n_\omega/(2\pi c)$, and V_{11} is the matrix element of electron scattering within the subband $e1$. Note that, while the matrix element in Eq. (59) is odd in the wavevector, the absorption probability given by the squared matrix element is even in $(\boldsymbol{k'}-\boldsymbol{k})$. Thus, this type of processes alone does not introduce an asymmetry in the carrier distribution in $\boldsymbol{k}$-space and, consequently, does not yield an electric current.

In the geometry of oblique incidence, which is required for the CPGE in (001)-oriented structures, additional pathways with intermediate states in the excited subbands $e2$, $e3$ etc. also contribute to the radiation absorption. Such virtual transitions (path II) via states in the $e2$ subband are sketched in Fig. 35(d) and (e). The matrix elements of the transitions with intermediate states in the subband n ($n \neq 1$) have the form [112]

$$M^{(n)}_{\boldsymbol{k'k}} \;=\; \mathrm{i}\,\frac{eA}{c\hbar}\left(\frac{\varepsilon_{n1}}{\varepsilon_{n1}-\hbar\omega} - \frac{\varepsilon_{n1}}{\varepsilon_{n1}+\hbar\omega}\right) e_z\, z_{n1}\, V_{1n}\,, \tag{60}$$

where ε_{n1} is the energy separation between the subbands at $\boldsymbol{k}=0$, $z_{n1} = \int \phi_n(z)z\,\phi_1(z)\,dz$ the coordinate matrix element, $\phi_n(z)$ the function of size quantization, and V_{1n} is the matrix element of intersubband scattering. Equation (60) exhibits that this type of indirect transitions is independent of $\boldsymbol{k}$ and, consequently, also does not result in an electric current.

The photocurrent emerges due to quantum interference of the virtual transitions considered above. Indeed, the total probability for the real optical

transition from $\boldsymbol{k}$ to $\boldsymbol{k}'$ is given by the squared modulus of the sum of matrix elements describing individual pathways,

$$
\begin{aligned}
W_{\boldsymbol{k}'\boldsymbol{k}} &\propto |M^{(1)}_{\boldsymbol{k}'\boldsymbol{k}} + \sum_{n\neq 1} M^{(n)}_{\boldsymbol{k}'\boldsymbol{k}}|^2 \\
&= |M^{(1)}_{\boldsymbol{k}'\boldsymbol{k}}|^2 + |\sum_{n\neq 1} M^{(n)}_{\boldsymbol{k}'\boldsymbol{k}}|^2 + 2\sum_{n\neq 1}\mathrm{Re}\left[M^{(1)}_{\boldsymbol{k}'\boldsymbol{k}} M^{(n)*}_{\boldsymbol{k}'\boldsymbol{k}}\right].
\end{aligned}
\tag{61}
$$

Beside the probabilities of individual processes, it contains interference terms. By using Eqs. (59) and (60) one can derive for the last terms on the right-hand side of Eq. (61)

$$
\begin{aligned}
\mathrm{Re}\left[M^{(1)}_{\boldsymbol{k}'\boldsymbol{k}} M^{(n)*}_{\boldsymbol{k}'\boldsymbol{k}}\right] &= \mathrm{i}\,\frac{e^2 A^2}{c^2 m_\perp}\frac{\varepsilon_{n1} z_{n1}}{\varepsilon_{n1}^2 - (\hbar\omega)^2}\,V_{11}\,V_{1n} \\
&\times\; [(k'_x - k_x)(e_z e_x^* - e_x e_z^*) + (k'_y - k_y)(e_z e_y^* - e_y e_z^*)].
\end{aligned}
\tag{62}
$$

These terms are odd in the wavevector and, therefore, result in different rates for the transitions to $\boldsymbol{k}'$ and $-\boldsymbol{k}'$. This leads to an imbalance in the carrier distribution between $\boldsymbol{k}'$ and $-\boldsymbol{k}'$, i.e. to an electric current $\boldsymbol{j}$. Such a difference in real optical transition rates caused by constructive or destructive interference of various pathways is illustrated in Fig. 35(a). Moreover, it follows from Eq. (62) that the sign of the interference terms is determined by components of the vector product $\mathrm{i}(\boldsymbol{e}\times\boldsymbol{e})$ and, thus, by the radiation helicity since $\mathrm{i}(\boldsymbol{e}\times\boldsymbol{e}) = \hat{\boldsymbol{e}}P_{\mathrm{circ}}$. Therefore, the imbalance of the carrier distribution in $\boldsymbol{k}$-space and, consequently, the photocurrent reverse upon switching the light helicity.

For the calculation of the photocurrent it is assumed that (i) electrons populate only the ground subband, (ii) they are elastically scattered by short-range defects, and (iii) $\hbar\omega < \varepsilon_{21}$. Then, making an allowance for transitions via all electron subbands, one can write for the photocurrent [30, 112]

$$
\begin{aligned}
\boldsymbol{j} &= e\,\frac{8\pi}{\hbar}\sum_{\boldsymbol{k},\boldsymbol{k}'}[\tau_p(\varepsilon_{\boldsymbol{k}'})\boldsymbol{v}_{\boldsymbol{k}'} - \tau_p(\varepsilon_{\boldsymbol{k}})\boldsymbol{v}_{\boldsymbol{k}}]\,[f(\varepsilon_{\boldsymbol{k}}) - f(\varepsilon_{\boldsymbol{k}'})] \\
&\times\;\sum_{n\neq 1}2\,\mathrm{Re}\left[M^{(1)}_{\boldsymbol{k}'\boldsymbol{k}} M^{(n)*}_{\boldsymbol{k}'\boldsymbol{k}}\right]\delta(\varepsilon_{\boldsymbol{k}'} - \varepsilon_{\boldsymbol{k}} - \hbar\omega),
\end{aligned}
\tag{63}
$$

where τ_p is the momentum relaxation time, $\boldsymbol{v}_{\boldsymbol{k}} = \hbar\boldsymbol{k}/m_\perp$ the electron velocity in the channel plane, $\varepsilon_{\boldsymbol{k}} = \hbar^2\boldsymbol{k}^2/(2m_\perp)$ the electron kinetic energy measured

from the subband bottom, $f(\varepsilon_{\boldsymbol{k}})$ the function of equilibrium carrier distribution in the subband $e1$, and the factor 8 in Eq. (63) accounts for the spin and valley degeneracy. For the electron scattering by short-range defects within the subband $e1$, the momentum relaxation time is given by $1/\tau_p = m_\perp \langle V_{11}^2 \rangle / \hbar^3$, where the angular brackets denote averaging over the impurity distribution.

Finally, by summing up Eq. (63) over the wavevectors $\boldsymbol{k}$ and $\boldsymbol{k}'$ the following expressions for the components of the helicity dependent photocurrent density result:

$$j_x/I \;=\; e\,\frac{4\pi\alpha}{\omega n_\omega}\,\frac{\kappa\hbar}{m_\perp}\sum_{n\neq 1}\frac{\langle V_{11}V_{1n}\rangle}{\langle V_{11}^2\rangle}\,\frac{\varepsilon_{n1}z_{n1}}{\varepsilon_{n1}^2 - (\hbar\omega)^2}\,N_{\mathrm{s}}\,\hat{e}_y\,P_{\mathrm{circ}} \tag{64}$$

and $j_y = -(\hat{e}_x/\hat{e}_y)j_x$, where $\alpha = e^2/(\hbar c)$ is the fine-structure constant and κ is a dimensional parameter, which is given by

$$\kappa = \int\limits_0^\infty (1 + 2\varepsilon/\hbar\omega)[f(\varepsilon) - f(\varepsilon + \hbar\omega)]\,d\varepsilon \;\bigg/\; \int\limits_0^\infty f(\varepsilon)d\varepsilon$$

and equals 1 and 2 in the cases of $\hbar\omega \gg \bar{\varepsilon}$ and $\hbar\omega \ll \bar{\varepsilon}$, respectively, with the mean kinetic energy of carriers in the equilibrium $\bar{\varepsilon}$ [23].

5.2.2.3   The CPGE in MOSFETs on miscut surfaces: In Si-MOSFETs fabricated on a miscut surface, the CPGE becomes possible even at normal incidence of radiation. This stems from the anisotropy of the electron dispersion in a valley together with the asymmetry of the confinement potential [22,110]. The Hamiltonian describing electron states in the channel on a miscut surface in each of the low-energy valleys has the form (see, e.g., Ref. [30])

$$H \;=\; \frac{p_{x'}^2}{2m_{x'x'}} + \frac{p_{y'}^2}{2m_{y'y'}} + \frac{p_{z'}^2}{2m_{z'z'}} + \frac{p_{y'}p_{z'}}{m_{y'z'}} + V(z')\,, \tag{65}$$

where $\boldsymbol{p}$ is the momentum operator, $V(z')$ the confining potential, and $1/m_{\alpha\beta}$ the tensor of the reciprocal effective masses with non-zero components $m_{x'x'} = m_\perp$, $1/m_{y'y'} = \cos^2\vartheta/m_\perp + \sin^2\vartheta/m_\parallel$, $1/m_{y'z'} = (1/m_\perp - 1/m_\parallel)\cos\vartheta\sin\vartheta$, $1/m_{z'z'} = \cos^2\vartheta/m_\parallel + \sin^2\vartheta/m_\perp$. The only nontrivial symmetry element, which does not change the Hamiltonian in Eq. (65) provided that $V(-z') \neq V(z')$, is the mirror reflection $x' \to -x'$. Thus, the Hamiltonian corresponds

to the C_s point-group symmetry that allows the photocurrent even in the geometry of normally incident radiation.

Similarly to (001)-oriented structures, the microscopic origin of the CPGE is the quantum interference of virtual optical transitions with intermediate states in the ground and excited subbands. The latter processes are possible in structures on miscut surfaces even at normal incidence of radiation due to the presence of the off-diagonal component $p_{y'}p_{z'}/m_{y'z'}$ in the Hamiltonian, which couples the motion of carriers along the y' and z' axes. The matrix elements of virtual transitions via states in the ground and excited electron subbands have the form [22]

$$
M_{\mathbf{k}'\mathbf{k}}^{(1)} = \frac{eA}{c\omega} \left[\frac{(k'_{x'} - k_{x'})\, e_{x'}}{m_{x'x'}} + \frac{(k'_{y'} - k_{y'})\, e_{y'}}{\tilde{m}_{y'y'}} \right] V_{11} \, , \tag{66}
$$

$$
M_{\mathbf{k}'\mathbf{k}}^{(n)} = 2\mathrm{i}\, \frac{eA}{c\hbar}\, \frac{m_{z'z'}}{m_{y'z'}}\, \frac{\hbar\omega\, \varepsilon_{n1} z'_{n1}}{(\hbar\omega)^2 - \varepsilon_{n1}^2}\, e_{y'}\, V_{1n} \, . \tag{67}
$$

Finally, calculating Eq. (63) with the matrix elements of Eqs. (66) and (67) and taking into account that $1/\tau_p = \sqrt{m_{x'x'}\tilde{m}_{y'y'}}\langle V_{11}^2\rangle/\hbar^3$ in the case of short-range scattering, one can derive

$$
\begin{aligned}
j_{x'}/I =\ & e\, \frac{4\pi\alpha}{\omega n_\omega}\, \frac{\kappa\hbar}{m_{y'z'}}\, \frac{m_{z'z'}}{m_{x'x'}}\, \sqrt{\frac{\tilde{m}_{y'y'}}{m_{x'x'}}} \\
& \times \sum_{n\neq 1} \frac{\langle V_{11}V_{1n}\rangle}{\langle V_{11}^2\rangle}\, \frac{\varepsilon_{n1} z'_{n1}}{\varepsilon_{n1}^2 - (\hbar\omega)^2}\, N_s\, \hat{e}_{z'}\, P_{\mathrm{circ}} \, .
\end{aligned} \tag{68}
$$

According to the symmetry analysis, the helicity-dependent photocurrent induced by normally incident radiation arises to the extent of the channel plane deviation from the plane (001) together with the channel asymmetry. This follows also from Eq. (68), which demonstrates that the current $j_{y'}$ vanishes if the channel plane is parallel to (001), where $1/m_{y'z'} = 0$, or for the symmetrical structure, where $z'_{n1}\langle V_{11}V_{1n}\rangle = 0$ for any n [23].

5.2.3 Discussion of the experimental results

Equations (64) and (68) describe the main features of the circular photocurrent observed in electron channels on (001)-oriented and miscut silicon surfaces. In

fact, it follows from Eq. (64) that the CPGE in the (001)-oriented structure can only occur at oblique incidence and in the direction normal to the incidence plane. By contrast, in miscut structures, the circular photocurrent along x' can be excited even at normal incidence (see Eq. (68)). Such a behavior of the CPGE with respect to the light propagation direction and crystallographic orientation has indeed been observed in all samples under study.

The microscopic origin of the circular photocurrent reversal upon variation of the energy separation between the subbands from $\varepsilon_{21} < \hbar\omega$ to $\varepsilon_{21} > \hbar\omega$ can be also clarified from Eqs. (64) and (68). In the vicinity of the intersubband resonance, the spectral dependence of the photocurrent is given by $1/[\varepsilon_{n1}^2 - (\hbar\omega)^2]$, which stems from the matrix elements describing virtual transitions via the excited subbands, see Eqs. (60) and (67). Thus, the photocurrent should increase drastically and undergo spectral inversion at $\hbar\omega \approx \varepsilon_{n1}$. In experiment, the resonant condition is obtained by tuning the intersubband separation with the gate voltage while the photon energy $\hbar\omega$ is fixed. Since at low temperatures only the ground subband is populated, the photocurrent inversion upon variation of V_{g} is observed for $\hbar\omega \approx \varepsilon_{21}$, see Fig. 33. While Eqs. (64) and (68) yield sharp spectral resonances, in real structures the dependence smooths because of broadening, but the inversion remains.

The magnitude of the CPGE detected in the transistor on the miscut surface with $\delta\Theta = 9.7°$ for $\hbar\omega = 8.4$ meV and $V_{\mathrm{g}} = 3$ V is $J_x/P \sim 1$ nA/W, yielding the current density $j_x/I \sim 0.1$ nA cm/W. The same order of magnitude is obtained from Eq. (68) for the structure with the miscut angle $\delta\Theta = 9.7°$, the carrier density $N_{\mathrm{s}} = 5 \times 10^{11}$ cm^{-2} ($V_{\mathrm{g}} = 3$ V), the channel width $a = 8$ nm and the structure asymmetry degree $\langle V_{11} V_{12}\rangle / \langle V_{11}^2\rangle = 10^{-2}$.

In Eqs. (64) and (68) the intrasubband optical transitions within the ground subband were derived assuming that the momentum relaxation time τ_p is independent of the electron energy. Such an approximation is reasonable, if the kinetic energy of photoexcited carriers is smaller than ε_{21}. For electrons generated with the energy $\varepsilon_{\boldsymbol{k}} > \varepsilon_{21}$, the momentum relaxation time gets shorter due to the additional relaxation channel caused by intersubband scattering. Consequently, one can expect that the magnitude of the CPGE current is smaller at $\hbar\omega > \varepsilon_{21}$ (low V_{g}) than that at $\hbar\omega < \varepsilon_{21}$ (high V_{g}). This can be responsible for

the observed asymmetry in the gate voltage dependence of the photocurrent in the vicinity of the intersubband resonance, see Fig. 33. The gate voltage changes also the channel profile, which can be taken into account assuming that the ratio $\langle V_{11}V_{1n}\rangle/\langle V_{11}^2\rangle$ and the coordinate matrix elements z_{n1} depend on V_{g}. At $\hbar\omega \geq \varepsilon_{21}$, possible contributions to the CPGE due to intersubband optical transitions as well as scattering-induced broadening of the absorption peak should also be considered [110].

With increasing temperature the intersubband resonances are broadened and the excited subbands $e2$, $e3$ etc. become also occupied in the equilibrium. It leads to additional channels of the current formation including those with initial states in the excited subbands. As a result, both the resonant LPGE and CPGE at $\hbar\omega \approx \varepsilon_{21}$ drastically decrease with temperature (see Fig. 34), and the spectral behavior of the photocurrent becomes more complicated. The experiments exhibit that at room temperature the CPGE current inversion with the gate voltage is detected only for the photon energy $\hbar\omega = 16.3$ meV. Moreover, even in this case, the point of inversion does not correspond to $\hbar\omega = \varepsilon_{21}$ [23].

5.2.4   Classical high frequency model of the current generation

While in the previous paragraphs the orbital mechanism of the photocurrent generation in silicon was referred to a quantum mechanical interference model, in this section it is explained in terms of the classical high frequency conductivity after Ref. [109], see also Chap. 2.1. This model is in an analogous manner valid for the experiments discussed above, as the photon energy is much smaller than the mean kinetic energy of the charge carriers, $\hbar\omega \ll \bar{\varepsilon}$, and can be applied to the CPGE in very good agreement with the quantum mechanical mechanism. However, in addition, it delivers some basic principles to understand qualitatively the linear photogalvanic effect, whose quantum mechanical model is not developed yet. Note that a similar mechanism explaining the photogalvanic effect in the presence of a static magnetic field (magneto-gyrotropic photogalvanic effect, MPGE) was already presented in Refs. [109, 117, 118].

Figure 36 illustrates the generation of a directed current in an asymmetric heterostructure like, e.g., a Si-MOSFET, under illumination with an alternat-
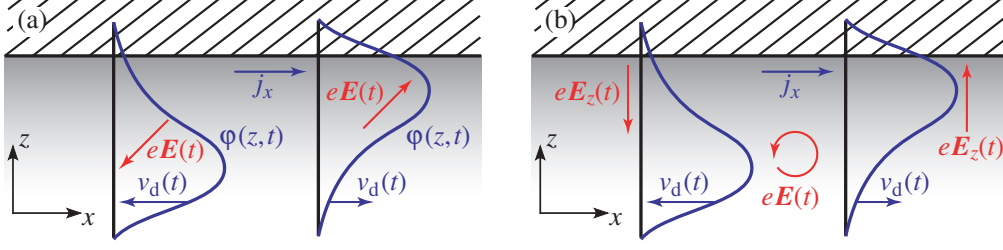
Figure 36: Microscopic model of the directed current generation j_x by (a) linearly and (b) circularly polarized light in a heterostructure.

ing electric field $\boldsymbol{E}(t)$. The shown structure possesses the $C_{\infty v}$ point-group symmetry being relevant for (001)-oriented Si-MOSFETs. Here, a nonequivalence of the z and $-z$ direction is introduced by an asymmetric confinement potential resulting in different scattering times τ and mobilities μ next to the oxide layer on top (shaded) in comparison to the interior of the p-type Si substrate (gray color gradient). Due to symmetry considerations mentioned above, the system must be illuminated under oblique incidence of light for observing photogalvanic effects, which yields in-plane E_x, E_y as well as out-of-plane E_z components of the electric field. Like in Fig. 36(a), the in-plane $E_x(t)$ and out-of-plane $E_z(t)$ components of linearly polarized radiation are in phase. Considering solely the E_x component does not lead to a directed current in x direction, as the oscillating field component results only in an alternating current within the 2DES plane without a time-averaged net direction. However, taking into account also the out-of-plane electric field E_z oscillating at the same frequency ω, yields a force acting on the carriers in z direction and changes thereby their wavefunction along the growth direction $\varphi(z, t)$. Charge carriers pushed to the upper interface are in this figure exposed to a stronger scattering than those pushed into negative z direction. Therefore, the time dependence of $\varphi(z, t)$ results in a modulated mobility $\mu(t)$ of the carriers due to the different scattering rates and, consequently, in a time dependent drift velocity $v_{\mathrm{d}}(t)$. Finally, carriers driven into one direction of the 2DES plane have a higher in-plane velocity v_{d} than those half a period of the field $\boldsymbol{E}(t)$ later, where the carrier flow is directed oppositely. Such an asymmetric carrier drift distribution between x and $-x$ (corresponding to an imbalance in $\boldsymbol{k}$-space) results in a direct electric current j_x.

For circularly polarized radiation (see Fig. 36(b)), in contrast, the phases of the in-plane and out-of-plane components of the ac electric field $\boldsymbol{E}(t)$ are phase shifted by $\pm 90°$, i.e. the component $E_z(t)$ is maximal when $E_x(t)$ vanishes and vice versa. In the case of a static electric field ($\omega \to 0$), the time averaged product $E_x(t)E_z(t)$ is zero and no electric current emerges. However, for higher frequencies the retardation of the drift velocity $\boldsymbol{v}_\mathrm{d}$ with respect to the in-plane field $E_x(t)$ enables a net particle flow averaged in time. This phase shift with the value $\arctan \omega\tau$ resulting from the Drude approach of high frequency conductivity was already discussed in the Chaps. 2.1 and 4.1.2. Here, the retardation lets the carriers still move within the 2DES plane when $E_x(t) = 0$ so that the component $E_z(t)$ can efficiently affect the scattering. This again results in a modulated drift velocity and, thus, in an electric current in x direction. Note that changing the helicity of the light from left- to right-handed circularly polarization reverses the current direction, as the phase shift between $E_x(t)$ and $E_z(t)$ gets a different sign [109].

5.2.5   Summary of the orbital mechanisms

In conclusion, the circular and linear photogalvanic effects are studied in Si-MOSFETs under excitation with linearly and elliptically polarized radiation in the THz frequency range. The behavior of the photogalvanic effects upon variation of the radiation's polarization state, wavelength, temperature and bias voltage are investigated in transistors prepared on precisely (001)-oriented as well as on miscut surfaces. The observed polarization dependences of the photocurrent are well described by the phenomenological theory of the photogalvanic effects based on a symmetry analysis of the studied structures. The experiments on Si-based structures reveal that photon-helicity sensitive photocurrents of pure orbital origin can even be generated in low-dimensional semiconductors with a simple band structure and with negligible spin-orbit interaction. Thereby, the mechanism of the photocurrent formation is based on the quantum interference of different pathways, which contribute to the absorption of radiation. A microscopic theory of the circular photogalvanic effect under intrasubband (Drude-like) absorption within the lowest electron subband is developed that shows good agreement with the experimental find-

ings. Finally, a qualitative model has been presented, which describes classically both the circular and linear photogalvanic effect in terms of the high frequency conductivity.

6 Conclusions

To summarize this work, photocurrents induced by terahertz laser radiation are employed to study optoelectronic transport phenomena in multi-valley semiconductors. It is demonstrated that the individual control of electron fluxes in valleys can be achieved by the excitation of valley degenerate structures by polarized light. The experiments in graphene as well as silicon together with theoretical considerations show that the microscopic origins of these currents are mainly orbital mechanisms, what is expected taking into account the small spin-orbit interaction of these materials. Considering spin-unrelated roots of photocurrents, the charge carriers' orbital motion is caused by the alternating electric and magnetic field components of the incident radiation. Under asymmetric electron photoexcitation or relaxation, this may result in a directed and measurable electric current. It is shown that, in the THz frequency range, models based on the high frequency conductivity and the high frequency Hall effect are very effective to describe the experimental observations.

One essential aim of this work is the investigation of valley currents in multi-valley semiconductors. The appearance of a pure valley current is a specific feature of semiconductors with several equivalent valleys such as graphene, carbon nanotubes or silicon. It is experimentally demonstrated for the first time that the utilization of the valley degree of freedom yields pure valley-orbit currents, where carriers in different valleys flow in different directions so that the total charge current vanishes. Here, it is shown that these valley-orbit currents can effectively be generated at room-temperature by optical excitation of (111)-oriented silicon possessing six individual valleys. The electron fluxes in individual valleys can be controlled by simple means, namely, by the variation of the light's polarization in exactly oriented Si or by the disturbance of the valleys' equivalence in miscut structures. A controllable way of a selective occupation of individual valleys and the generation of pure orbit-valley currents are key ingredients for valleytronics aimed at the development of novel solid-state devices, which are characterized by less dissipation in comparison to conventional bipolar electronics.

Another goal is to explore orbital mechanisms underlying the generation of photocurrents. Thereby, ideal candidates to study these spin-unrelated phenomena are graphene as well as silicon, which are both characterized by a vanishingly small spin-orbit coupling, so that spin mechanisms as microscopic origin of photocurrents become ineffective. In this manner, it is experimentally demonstrated that the optical excitation of graphene by THz radiation causes directed electric currents, including those solely driven by the circular polarization of light. The presented experiments evidence that these helicity driven photocurrents are due to purely orbital mechanisms. Thus, the current generation is caused by the circular photon drag (or high frequency Hall) effect, which stems from the simultaneous transfer of the linear and angular momenta of photons to the free carriers of graphene. Within this work, the model of the circular ac Hall effect well describing the experimental finding is developed. While in the conventional dc Hall effect a perpendicularly applied magnetic field deflects charge carriers transverse to the current direction, it is the electric and magnetic fields of a circularly polarized light wave, rotating at terahertz frequencies, that generates a current perpendicular to the wavevector of the incident light and thus constitutes the circular ac Hall effect. Switching the light's helicity – and thus the direction of the carrier velocity – inverts also the polarity of the current. The specific crystallographic symmetry of graphene makes it possible to unveil this novel effect, which provides a new access to the understanding and application of carbon based nanostructures.

Other examples for purely orbital photocurrents are both the circular and linear photogalvanic effects in Si-MOSFET structures. Therefore, the current generation in exactly (001)-oriented as well as miscut Si-MOSFETs is investigated experimentally and theoretically. It is shown that the origin of these currents can be described by orbital models, either by the interference of different pathways contributing to the light absorption within a quantum mechanical approach, or classically by the high frequency conductivity based on the Drude model. The orbital roots of photocurrents are very general and should take part in the current formation upon incident radiation in a great variety of materials, where only spin-related origin have been addressed so far.

References

[1] A. H. Castro Neto, F. Guinea, N. M. R. Peres, K. S. Novoselov, and A. K. Geim, *The electronic properties of graphene*, Rev. Mod. Phys. **81**, 109 (2009).

[2] N. M. R. Peres, *Colloquium: The transport properties of graphene: An introduction*, Rev. Mod. Phys. **82**, 2673 (2010).

[3] S. Das Sarma, Shaffique Adam, E. H. Hwang, and Enrico Rossi, *Electronic transport in two-dimensional graphene*, Rev. Mod. Phys. **83**, 407 (2011).

[4] K. S. Novoselov, A. K. Geim, S. V. Morozov, D. Jiang, Y. Zhang, S. V. Dubonos, I. V. Grigorieva, and A. A. Firsov, *Electric Field Effect in Atomically Thin Carbon Films*, Science **306**, 666 (2004).

[5] S. V. Morozov, K. S. Novoselov, M. I. Katsnelson, F. Schedin, D. C. Elias, J. A. Jaszczak, and A. K. Geim, *Giant Intrinsic Carrier Mobilities in Graphene and Its Bilayer*, Phys. Rev. Lett. **100**, 016602 (2008).

[6] F. Schwierz, *Graphene Transistors*, Nature Nanotechnol. **5**, 487 (2010).

[7] Yanqing Wu, Yu ming Lin, Ageeth A. Bol, Keith A. Jenkins, Fengnian Xia, Damon B. Farmer, Yu Zhu, and Phaedon Avouris, *High-frequency, scaled graphene transistors on diamond-like carbon*, Nature **472**, 74 (2011).

[8] A. Rycerz, J. Tworzydlo, and C. W. J. Beenakker, *Valley filter and valley valve in graphene*, Nature Phys. **3**, 172 (2007).

[9] J. L. Garcia-Pomar, A. Cortijo, and M. Nieto-Vesperinas, *Fully Valley-Polarized Electron Beams in Graphene*, Phys. Rev. Lett. **100**, 236801 (2008).

[10] A. S. Moskalenko and J. Berakdar, *Light-induced valley currents and magnetization in graphene rings*, Phys. Rev. B **80**, 193407 (2009).

[11] I. Žutić, J. Fabian, and S. Das Sarma, *Spintronics: Fundamentals and applications*, Rev. Mod. Phys. **76**, 323 (2004).

[12] S. A. Tarasenko and E. L. Ivchenko, *Pure spin photocurrents in low-dimensional structures*, Pis'ma Zh. Eksp. Teor. Fiz. **81**, 292 (2005). [JETP Lett. **81**, 231 (2005)].

[13] R. N. McFarland, T. M. Kott, L. Sun, K. Eng, and B. E. Kane, *Temperature-dependent transport in a sixfold degenerate two-dimensional electron system on a H-Si(111) surface*, Phys. Rev. B **80**, 161310(R) (2009).

[14] J. Karch, P. Olbrich, M. Schmalzbauer, C. Zoth, C. Brinsteiner, M. Fehrenbacher, U. Wurstbauer, M. M. Glazov, S. A. Tarasenko, E. L. Ivchenko, D. Weiss, J. Eroms, R. Yakimova, S. Lara-Avila, S. Kubatkin, and S. D. Ganichev, *Dynamic Hall Effect Driven by Circularly Polarized Light in a Graphene Layer*, Phys. Rev. Lett. **105**, 227402 (2010).

[15] J. Karch, P. Olbrich, M. Schmalzbauer, C. Brinsteiner, U. Wurstbauer, M. M. Glazov, S. A. Tarasenko, E. L. Ivchenko, D. Weiss, J. Eroms, and S. D. Ganichev, *Photon helicity driven electric currents in graphene*, arXiv: 1002.1047v1 (2010).

[16] D. Gunlycke and C. T. White, *Graphene Valley Filter Using a Line Defect*, Phys. Rev. Lett. **106**, 136806 (2011).

[17] J. Karch, S. A. Tarasenko, E. L. Ivchenko, J. Kamann, P. Olbrich, M. Utz, Z. D. Kvon, and S. D. Ganichev, *Photoexcitation of valley-orbit currents in (111)-oriented silicon metal-oxide-semiconductor field-effect transistors*, Phys. Rev. B **83**, 121312(R) (2011).

[18] S. D. Ganichev and W. Prettl, *Spin photocurrents in quantum wells*, J. Phys.: Condens. Matter **15**, R935 (2003).

[19] S. D. Ganichev, E. L. Ivchenko, S. N. Danilov, J. Eroms, W. Wegscheider, D. Weiss, and W. Prettl, *Conversion of Spin into*

Directed Electric Current in Quantum Wells, Phys. Rev. Lett. **86**, 4358 (2001).

[20] S. D. Ganichev, E. L. Ivchenko, V. V. Bel'kov, S. A. Tarasenko, M. Sollinger, D. Weiss, W. Wegscheider, and W. Prettl, *Spin-galvanic effect*, Nature (London) **417**, 153 (2002).

[21] R. Winkler, *Spin-Orbit Coupling Effects in Two-Dimensional Electron and Hole Systems.* Springer, Berlin, 2003.

[22] P. Olbrich, S. A. Tarasenko, C. Reitmaier, J. Karch, D. Plohmann, Z. D. Kvon, and S. D. Ganichev, *Observation of the orbital circular photogalvanic effect*, Phys. Rev. B **79**, 121302 (2009).

[23] J. Karch, S. A. Tarasenko, P. Olbrich, T. Schönberger, C. Reitmaier, D. Plohmann, Z. D. Kvon, and S. D. Ganichev, *Orbital photogalvanic effects in quantum-confined structures*, J. Phys.: Condens. Matter **22**, 355307 (2010).

[24] A. M. Fox, *Optical Properties of Solids.* Oxford Univ. Press, Oxford, 2007.

[25] P. Drude, *Zur Elektronentheorie der Metalle*, Annalen der Physik **306**, 566 (1900).

[26] N. W. Ashcroft and N. D. Mermin, *Solid State Physics.* Brooks/Cole Thomson Learning, Singapore, 2009.

[27] K. Seeger, *Semiconductor Physics.* Springer-Verlag, Wien, 1973.

[28] E. L. Ivchenko, *Optical Spectroscopy of Semiconductor Nanostructures.* Alpha Science Int., Harrow, 2005.

[29] S. D. Ganichev and W. Prettl, *Intense Terahertz Excitation of Semiconductors.* Oxford Univ. Press, Oxford, 2006.

[30] E. L. Ivchenko and G. E. Pikus, *Superlattices and Other Heterostructures. Symmetry and Optical Phenomena.* Springer, Berlin, 1997.

[31] B. I. Sturman and V. M. Fridkin, *The Photovoltaic and Photorefractive Effects in Non-Centrosymmetric Materials*. Gordon and Breach Science Publishers, New York, 1992.

[32] A. V. Ioffe and A. F. Ioffe, *Photoelectromotive forces in cubrite crystals*, Zh. Èksp. Teor. Fiz. **5**, 112 (1935). (in Russian).

[33] H. M. Barlow, *Application of the Hall effect in a semiconductor to the measurement of power in an electromagnetic field*, Nature (London) **173**, 41 (1954).

[34] A. M. Danishevskii, A. A. Kastal'skii, S. M. Ryvkin, and I. D. Yaroshetskii, *Dragging of free carriers by photons in direct interband transitions in semiconductors*, Zh. Èksp. Teor. Fiz. **58**, 544 (1970). [Sov. Phys. JETP **31**, 292 (1970)].

[35] A. F. Gibson, M. F. Kimmit, and A. C. Walker, *Photon drag in germanium*, Appl. Phys. Lett. **17**, 75 (1970).

[36] E. L. Ivchenko and G. E. Pikus, *Semiconductor Physics*. in *Problems of Modern Physics*, p. 427, eds. V. M. Tuchkevich and V. Ya. Frenkel (Cons. Bureau, 1986).

[37] V. I. Belinicher, *On the mechanisms underlying the circular drag effect*, Fiz. Tverd. Tela **23**, 3461 (1981). [Sov. Phys. Solid State **23**, 2012 (1981)].

[38] V. A. Shalygin, H. Diehl, Ch. Hoffmann, S. N. Danilov, T. Herrle, S. A. Tarasenko, D. Schuh, Ch. Gerl, W. Wegscheider, W. Prettl, and S. D. Ganichev, *Spin photocurrents and circular photon drag effect in (110)-grown structures*, JETP Lett. **84**, 570 (2006).

[39] W. Weber, L. E. Golub, S. N. Danilov, J. Karch, C. Reitmaier, B. Wittmann, V. V. Bel'kov, E. L. Ivchenko, Z. D. Kvon, N. Q. Vinh, A. F. G. van der Meer, B. Murdin, and S. D. Ganichev, *Quantum ratchet effects induced by terahertz radiation in GaN-based two-dimensional structures*, Phys. Rev. B **77**, 245304 (2008).

[40] P. Olbrich, E. L. Ivchenko, R. Ravash, T. Feil, S. D. Danilov, J. Allerdings, D. Weiss, D. Schuh, W. Wegscheider, and S. D. Ganichev, *Ratchet Effects Induced by Terahertz Radiation in Heterostructures with a Lateral Periodic Potential*, Phys. Rev. Lett. **103**, 090603 (2009).

[41] P. Reimann, *Brownian motors: Noisy transport far from equilibrium*, Phys. Rep. **361**, 57 (2002).

[42] P. Olbrich, J. Karch, E. L. Ivchenko, J. Kamann, B. März, M. Fehrenbacher, D. Weiss, and S. D. Ganichev, *Classical ratchet effects in heterostructures with a lateral periodic potential*, Phys. Rev. B **83**, 165320 (2011).

[43] N. A. Sinitsyn, *Semiclassical theories of the anomalous Hall effect*, J. Phys.: Condens. Matter **20**, 023201 (2008).

[44] J. F. Nye, *Physical Properties of Crystals: Their Representation by Tensors and Matrices.* Oxford Univ. Press, Oxford, 1985.

[45] E. L. Ivchenko and S. D. Ganichev, *Spin-Photogalvanics.* in *Spin Physics in Semiconductors*, p. 245, ed. M. I. Dyakonov (Springer, Berlin, 2008).

[46] L. D. Landau, E. M. Lifshits, and L. P. Pitaevskii, *Electrodynamics of Continues Media.* Elsevier, Amsterdam, 1984.

[47] S. D. Ganichev, *Spin-Galvanic Effect and Spin Orientation Induced Circular Photogalvanic Effect in Quantum Well Structures.* in series Advances in Solid State Physics, vol. 43, ed. B. Kramer (Springer, Berlin-Heidelberg, 2003), p. 427.

[48] M. I. Dyakonov, *Basics of Semiconductor and Spin Physics.* in *Spin Physics in Semiconductors*, p. 1, ed. M. I. Dyakonov (Springer, Berlin, 2008).

[49] S. D. Ganichev, V. V. Bel'kov, Petra Schneider, E. L. Ivchenko, S. A. Tarasenko, W. Wegscheider, D. Weiss, D. Schuh, E. V. Beregulin, and W. Prettl, *Resonant inversion of the circular photogalvanic effect in n-doped quantum wells*, Phys. Rev. B **68**, 035319 (2003).

[50] B. Wittmann, L. E. Golub, S. N. Danilov, J. Karch, C. Reitmaier, Z. D. Kvon, N. Q. Vinh, A. F. G. van der Meer, B. Murdin, and S. D. Ganichev, *Resonant circular photogalvanic effect in GaN/AlGaN heterojunctions*, Phys. Rev. B **78**, 205435 (2008).

[51] A. K. Geim and A. H. MacDonald, *Graphene: Exploring carbon flatland*, Phys. Today **60**, 35 (2007).

[52] A. K. Geim and K. S. Novoselov, *The rise of graphene*, Nature Mat. **6**, 183 (2007).

[53] P. R. Wallace, *The Band Theory of Graphite*, Phys. Rev. **71**, 622 (1947).

[54] B. Trauzettel, *Von Graphit zu Graphen*, Phys. Journal **6**, 39 (2007).

[55] A. K. Geim, *Graphene: Status and Prospects*, Science **324**, 1530 (2009).

[56] O. Klein, *Die Reflexion von Elektronen an einem Potentialsprung nach der relativistischen Dynamik von Dirac*, Z. Phys. **53**, 157 (1929).

[57] A. F. Young and P. Kim, *Quantum interference and carrier collimation in graphene heterojunctions*, Nature Phys. **5**, 222 (2009).

[58] N. Stander, B. Huard, and D. Goldhaber-Gordon, *Evidence for Klein Tunneling in Graphene p-n Junctions*, Phys. Rev. Lett. **102**, 026807 (2009).

[59] K. S. Novoselov, A. K. Geim, S. V. Morozov, D. Jiang, M. I. Katsnelson, I. V. Grigorieva, S. V. Dubonos, and A. A. Firsov, *Two-dimensional gas of massless Dirac fermions in graphene*, Nature (London) **438**, 197 (2005).

[60] Y. Zhang, Y.-W. Tan, H. L. Stormer, and P. Kim, *Experimental observation of the quantum Hall effect and Berry's phase in graphene*, Nature (London) **438**, 201 (2005).

[61] T. Ando, A. B. Fowler, and F. Stern, *Electronic properties of two-dimensional systems*, Rev. Mod. Phys. **54**, 437 (1982).

[62] F. Thuselt, *Physik der Halbleiterbauelemente.* Springer, Berlin, 2005.

[63] R. F. Pierret, *Semiconductor device fundamentals.* Addison-Wesley, Pearson International Edition, 2003.

[64] S. M. Sze and K. K. Ng, *Physics of semiconductor devices.* Wiley-Interscience, Hoboken, 2007.

[65] C. Kittel, *Introduction to solid state physics.* Wiley, Hoboken, 2005.

[66] H. Ibach and H. Lüth, *Festkörperphysik.* Springer, Berlin, 2002.

[67] T. Y. Chang and T. J. Bridges, *Laser action at 452, 496, and 541 μm in optically pumped CH_3F*, Optics Commun. **1**, 423 (1970).

[68] K. J. Button, *Pulsed Optically Pumped Far Infrared Lasers.* in *Infrared and Millimeter Waves Vol. 1: Sources of Radiation*, p. 129, ed. K. J. Button, (Academic Press Inc., London, 1979).

[69] F. K. Kneubühl and M. W. Sigrist, *Laser.* Teubner, Wiesbaden, 2005.

[70] O. Svelto, *Principles of lasers.* Plenum Press, New York, 1998.

[71] G. W. Chantry, *Long-wave optics Vol. 2: Applications.* Academic Press, London, 1984.

[72] D. G. Biron, R. J. Temkin, B. Lax, and B. G. Danly, *High-intensity CO_2 laser pumping of a CH_3F Raman FIR laser*, Opt. Lett. **4**, 381 (1979).

[73] D. G. Biron, B. G. Danly, R. J. Temkin, and B. Lax, *Far-Infrared Raman Laser with High Intensity Laser Pumping*, IEEE J. Quantum Electron. **17**, 2146 (1981).

[74] J. D. Wiggins, Z. Drozdowicz, and R. J. Temkin, *Two-Photon Transitions in Optically Pumped Submillimeter Lasers*, IEEE J. Quantum Electron. **14**, 23 (1978).

[75] Y. R. Shen, *The Principles of Nonlinear Optics.* Wiley Classics Library, Hoboken, 2003.

[76] W. Zinth and H. J. Körner, *Physik III.* Oldenbourg, München, 1998.

[77] E. V. Loewenstein, R. R. Smith, and R. L. Morgan, *Optical Constants of Far Infrared Materials. 2: Crystalline Solids*, Appl. Opt. **12**, 398 (1973).

[78] F. Brehat and B. Wyncke, *Measurement of the optical constants of crystal quartz at 10 K and 300 K in the far infrared spectral range*, Int. J. Infrared Milli. **18**, 1663 (1997).

[79] M. Born and E. Wolf, *Principles of optics.* Pergamon Press, Oxford, 1964.

[80] S. D. Ganichev, W. Weber, J. Kiermaier, S. N. Danilov, P. Olbrich, D. Schuh, W. Wegscheider, D. Bougeard, G. Abstreiter, and W. Prettl, *All-electric detection of the polarization state of terahertz laser radiation*, J. Appl. Phys. **103**, 114504 (2008).

[81] S. N. Danilov, B. Wittmann, P. Olbrich, W. Eder, W. Prettl, L. E. Golub, E. V. Beregulin, Z. D. Kvon, N. N. Mikhailov, S. A. Dvoretsky, V. A. Shalygin, N. Q. Vinh, A. F. G. van der Meer, B. Murdin, and S. D. Ganichev, *Fast detector of the ellipticity of infrared and terahertz radiation based on HgTe quantum well structures*, J. Appl. Phys. **105**, 013106 (2009).

[82] B. E. A. Saleh and M. C. Teich, *Fundamentals of photonics.* John Wiley and Sons, New Jersey, 2007.

[83] J. Eroms and D. Weiss, *Weak localization and transport gap in graphene antidot lattices*, New J. Phys. **11**, 095021 (2009).

[84] U. Stöberl, U. Wurstbauer, W. Wegscheider, D. Weiss, and J. Eroms, *Weak localization and transport gap in graphene antidot lattices*, Appl. Phys. Lett. **93**, 051906 (2008).

[85] C. Berger, Z. Song, X. Li, X. Wu, N. Brown, C. Naud, D. Mayou, T. Li, J. Hass, A. N. Marchenkov, E. H. Conrad, P. N. First, and W. A. de Heer, *Electronic Confinement and Coherence in Patterned Epitaxial Graphene*, Science **312**, 1191 (2006).

[86] A. Tzalenchuk, S. Lara-Avila, A. Kalaboukhov, S. Paolillo, M. Syväjärvi, R. Yakimova, O. Kazakova, T. J. B. M. Janssen, V. Fal'ko, and S. Kubatkin, *Towards a quantum resistance standard based on epitaxial graphene*, Nature Nanotech. **5**, 186 (2010).

[87] A. J. van Bommel, J. E. Crombeen, and A. van Tooren, *LEED and Auger electron observations of the SiC(0001) surface*, Surf. Sci. **48**, 463 (1975).

[88] T. Seyller, *Epitaktisches Graphen*, Phys. Journal **9**, 53 (2010).

[89] K. V. Emtsev, A. Bostwick, K. Horn, J. Jobst, G. L. Kellogg, L. Ley, J. L. McChesney, T. Ohta, S. A. Reshanov, J. Röhrl, E. Rotenberg, A. K. Schmid, D. Waldmann, H. B. Weber, and T. Seyller, *Towards wafer-size graphene layers by atmospheric pressure graphitization of silicon carbide*, Nature Mat. **8**, 203 (2009).

[90] C. Virojanadara, M. Syväjarvi, R. Yakimova, L. I. Johansson, A. A. Zakharov, and T. Balasubramanian, *Homogeneous large-area graphene layer growth on 6H-SiC(0001)*, Phys. Rev. B **78**, 245403 (2008).

[91] A. Bostwick, T. Ohta, T. Seyller, K. Horn, and E. Rotenberg, *Quasiparticle dynamics in graphene*, Nature Phys. **3**, 36 (2007).

[92] G. M. Gusev, N. V. Zavaritskii, Z. D. Kvon, and A. A. Yurgens, *Valley degeneracy of two-dimensional electrons on the (111) surface of silicon*, Pis'ma Zh. Eksp. Teor. Fiz. **40**, 275 (1984). [JETP Lett. **40**, 1056 (1984)].

[93] A. A. Kapustin, A. A. Shashkin, V. T. Dolgopolov, M. Goiran, H. Rakoto, and Z. D. Kvon, *Spin susceptibility and polarization field in a dilute two-dimensional electron system in (111) silicon*, Phys. Rev. B **79**, 205314 (2009).

[94] T. Hatano, T. Ishihara, S. G. Tikhodeev, and N. A. Gippius, *Transverse Photovoltage Induced by Circularly Polarized Light*, Phys. Rev. Lett. **103**, 103906 (2009).

[95] E. H. Hall, *On a New Action of the Magnet on Electric Currents*, Amer. J. Math. **2**, 287 (1879).

[96] V. I. Perel' and Ya. M. Pinskii, *Constant current in conducting media due to a high-frequency electron electromagnetic field*, Fiz. Tverd. Tela **15**, 996 (1973). [Sov. Phys. Solid State **15**, 688 (1973)].

[97] M. V. Entin, L. I. Magarill, and D. L. Shepelyansky, *Theory of resonant photon drag in monolayer graphene*, Phys. Rev. B **81**, 165441 (2010).

[98] V. L. Gurevich and R. Laiho, *Photomagnetism of metals: Microscopic theory of the photoinduced surface current*, Phys. Rev. B **48**, 8307 (1993).

[99] V. L. Gurevich and R. Laiho, *Photomagnetism of metals. first observation of dependence on polarization of light*, Phys. Solid State **42**, 1807 (2000).

[100] L. I. Magarill and M. V. Entin, *Photogalvanic effect in films*, Fiz. Tverd. Tela **21**, 1280 (1979). [Sov. Phys. Solid State **21**, 743 (1980)].

[101] V. L. Al'perovich, V. I. Belinicher, V. N. Novikov, and A. S. Terekhov, *Surface photovoltaic effect in gallium arsenide*, Pis'ma Zh. Eksp. Teor. Fiz. **31**, 581 (1980). [JETP Lett. **31**, 546 (1980)].

[102] A. A. Kaplyanskii, N. S. Sokolov, B. V. Novikov, and S. V. Gastev, *Selective Optical Valley Pumping in Silicon and Germanium*, Solid State Commun. **20**, 27 (1976).

[103] R. D. R Bhat, F. Nastos, Ali Najmaie, and J. E. Sipe, *Pure Spin Current from One-Photon Absorption of Linearly Polarized Light in Noncentrosymmetric Semiconductors*, Phys. Rev. Lett. **94**, 096603 (2005).

[104] S. D. Ganichev, V. V. Bel'kov, S. A. Tarasenko, S. N. Danilov, S. Giglberger, Ch. Hoffmann, E. L. Ivchenko, D. Weiss, W. Wegscheider, Ch. Gerl, D. Schuh, J. Stahl, J. De Boeck, G. Borghs, and W. Prettl, *Zero-bias spin separation*, Nature Phys. **2**, 609 (2006).

[105] Hui Zhao, Xinyu Pan, Arthur L. Smirl, R. D. R. Bhat, Ali Najmaie, J. E. Sipe, and H. M. van Driel, *Injection of ballistic pure spin currents in semiconductors by a single-color linearly polarized beam*, Phys. Rev. B **72**, 201302 (2005).

[106] E. L. Ivchenko and S. A. Tarasenko, *Pure spin photocurrents*, Semicond. Sci. Technol. **23**, 114007 (2008).

[107] C. L. Kane and E. J. Mele, Z_2 *Topological Order and the Quantum Spin Hall Effect*, Phys. Rev. Lett. **95**, 146802 (2005).

[108] M. König, S. Wiedmann, C. Brüne, A. Roth, H. Buhmann, L. W. Molenkamp, X.-L. Qi, and S.-C. Zhang, *Quantum Spin Hall Insulator State in HgTe Quantum Wells*, Science **318**, 766 (2007).

[109] S. A. Tarasenko, *Direct current driven by ac electric field in quantum wells*, Phys. Rev. B **83**, 035313 (2011).

[110] L. I. Magarill and M. V. Entin, *Photogalvanic effect in an inversion channel on a vicinal face*, Fiz. Tverd. Tela **31**, 37 (1989). [Sov. Phys. Solid State **31**, 1299 (1989)].

[111] J. Fang and G. P. Li, *Detection of gate oxide charge trapping by second-harmonic generation*, Appl. Phys. Lett. **75**, 3506 (1999).

[112] S. A. Tarasenko, *Orbital mechanism of the circular photogalvanic effect in quantum wells*, JETP Lett. **85**, 182 (2007).

[113] G. M. Gusev, Z. D. Kvon, L. I. Magarill, A. M. Palkin, V. I. Sozinov, O. A. Shegai, and M. V. Entin, *Resonant photovoltaic effect in an inversion layer at the surface of a semiconductor*, JETP Lett. **46**, 33 (1987).

[114] M. Bieler, N. Laman, H. M. van Driel, and Arthur L. Smirl, *Ultrafast spin-polarized electrical currents injected in a strained zinc blende semiconductor by single color pulses*, Appl. Phys. Lett. **86**, 061102 (2005).

[115] P. Kneschaurek, Avid Kamgar, and J. F. Koch, *Electronic levels in surface space charge layers on Si(100)*, Phys. Rev. B **14**, 1610 (1976).

[116] T. Ando, *Inter-subband optical absorption in space-charge layers on semiconductor surfaces*, Z. Phys. B **26**, 263 (1977).

[117] S. A. Tarasenko, *Electron scattering in quantum wells subjected to an in-plane magnetic field*, Phys. Rev. B **77**, 085328 (2008).

[118] V. Lechner, L. E. Golub, F. Lomakina, V. V. Bel'kov, P. Olbrich, S. Stachel, I. Caspers, M. Griesbeck, M. Kugler, M. J. Hirmer, T. Korn, C. Schüller, D. Schuh, W. Wegscheider, and S. D. Ganichev, *Spin and orbital mechanisms of the magneto-gyrotropic photogalvanic effects in GaAs/AlGaAs quantum well structures*, Phys. Rev. B **83**, 155313 (2011).

Danksagung

Ich möchte mich an dieser Stelle ganz herzlich bei allen bedanken, die mich während der Promotion begleitet und zum Gelingen dieser Dissertation maßgeblich beigetragen haben.

An erster Stelle gilt mein Dank meinen Eltern und meiner Großmutter, die mir mein Physikstudium überhaupt erst ermöglicht und mich auch noch während der Promotion unterstützt haben.

Besonders bedanken möchte ich mich zudem selbstverständlich bei Sergey Ganichev, in dessen Arbeitsgruppe ich diese Doktorarbeit anfertigen durfte und der dieses interessante Thema an mich vergeben hat. Stets opferte er seine wertvolle Zeit, um meine Fragen zur Theorie und zum Experiment zu beantworten.

Weiterhin geht mein Dank auch an alle meine Kollegen und die Ehemaligen der Arbeitsgruppe, sie waren immer für anregende Diskussionen bereit und sorgten für das hervorragende Arbeitsklima der AG Ganichev. Zu allererst danke ich hierbei Christoph Drexler, Vera Lechner und Sebastian Stachel für das Korrekturlesen meiner Arbeit, weiterhin natürlich Peter Olbrich, Markus Fehrenbacher, Josef Kamann, Thomas Schönberger, Tina Zoth, Sergey Danilov, Wilhelm Prettl, Thomas Stangl, Bernhard Wittmann, Christina Reitmaier, Michael Schmalzbauer, Chonyung Jiang, Ines Caspers, Marion Hirmer, Peter Lutz, Christoph Schönhuber, Wolfgang Weber, Juri Allerdings, Wolfgang Eder, Christoph Brinsteiner, Faina Lomakina, Cynthia Karl, Helgi Diehl, Daniel Plohmann und Stephan Giglberger. Unseren russischen Gästen Sergey Tarasenko, Mikhail Glazov, Eougenious Ivchenko, Leonid Golub, Dima Kvon, Vasily Bel'kov und Vadim Shalygin gilt mein Dank für ihren Beitrag zu Theorie und Experiment. Für die technische und formale Unterstützung bedanke ich mich bei Anton Humbs, Ulla Turba, Claudia Rahm und Hannelore Lanz.

Und natürlich darf ich an dieser Stelle nicht vergessen, ein großes Dankeschön an meine Freundin Steffi Pentz auszusprechen. Sie war in den letzten Jahren immer für mich da und musste sich alles anhören, was mich während meiner Doktorarbeit beschäftigte.